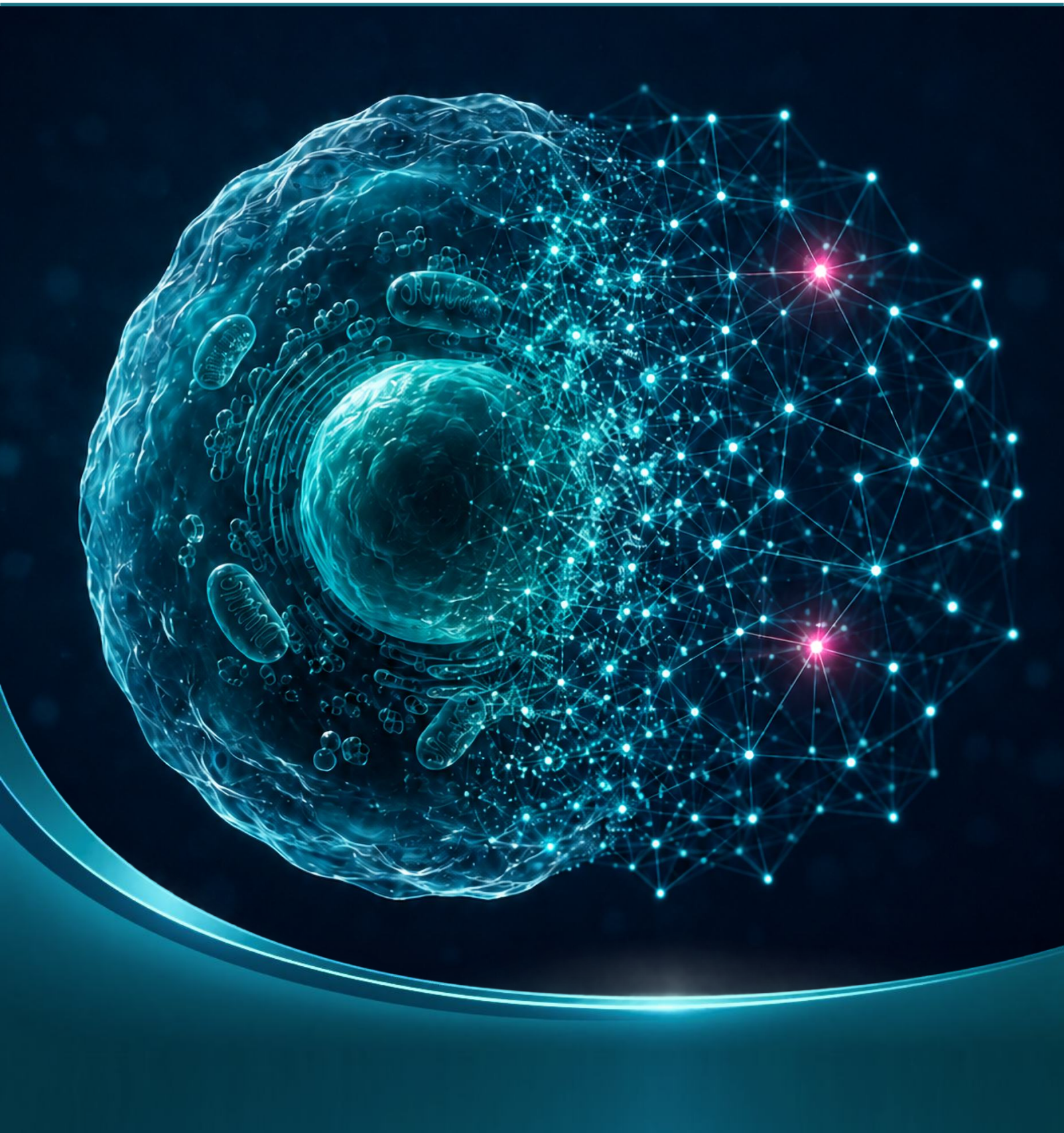
YASJ Young Australians Science Journal

Volume 1, Issue 1 | 27 November 2026 | Open Access | yasj.org.au



CALL FOR REVIEWERS

Help young scientists publish high quality articles

YASJ

The Young Australians Science Journal is looking for researchers and HDR students across all areas of science to review original research led by Australian high school students. Reviewers are provided with a template and guidance on reviewing student papers, and all feedback is filtered via the editorial panel prior to being shared with students.

SHARE YOUR EXPERTISE

Bring your discipline knowledge to support student-led research.

GIVE CONSTRUCTIVE FEEDBACK

Help young researchers strengthen their article structure, scientific reasoning, and written communication.

SUPPORT AUTHENTIC PEER REVIEW

Give students first-hand experience of science as an evolving dialogue between experts.

JOIN THE REVIEWER COMMUNITY

Register as a YASJ reviewer

https://yasj.org.au/

PUBLICATION INFORMATION

Journal	Young Australians Science Journal
Volume and issue	Volume 1, Issue 1
Publication date	27 November 2026
ISSN (print)	3083-0427
ISSN (online)	3083-0419
Publisher	Science Teachers Association of NSW Inc
Publisher address	77–79 Parramatta Road, Silverwater, NSW 2128
ABN	44 677 048 086
Website	https://yasj.org.au
Contact	editor@yasj.org.au

The Young Australians Science Journal (YASJ) is a peer-reviewed, open-access journal created to showcase the originality and talent of young Australian scientists. We enable high school students to share their research with the wider scientific community and experience authentic academic publishing.

YASJ is an initiative of its founding editorial team, published under the auspices of the Science Teachers Association of NSW (STANSW).

Potential advertisers or sponsors are invited to contact editor@yasj.org.au

Editorial independence

Editorial decisions are made independently of sponsors, partners, and advertisers. Publication of an advertisement does not constitute endorsement by the journal.

Copyright and licensing

Copyright in each article remains with its author or authors. Unless otherwise stated, articles in this issue are licensed under the Creative Commons Attribution-NonCommercial 4.0 International Licence (CC BY-NC 4.0). This licence permits sharing and adaptation for non-commercial purposes, provided appropriate credit is given to the author or authors and the source, a link to the licence is provided, and any changes are indicated. Third-party material is excluded from this licence unless otherwise stated.

Disclaimer

The views and conclusions expressed in signed articles are those of the authors and do not necessarily reflect those of the Young Australians Science Journal, its editors, reviewers, partners, sponsors or affiliated institutions. While reasonable care is taken through editorial and peer-review processes, responsibility for the accuracy and interpretation of the published work remains with the authors.

Cover image

The cover image represents how genetic information stored inside a breast cell is extracted and translated into data that a recurrent neural network can analyse. The network on the right represents patterns mapped between these data points, while the two bright pink nodes highlight influential genes used by the model in making its predictions.

Image created by Michaela Loukas using OpenAI ChatGPT image generation, based on concepts from *Assessing recurrent neural network accuracy and interpretability in breast cancer classification* (M. Loukas, 2026). The prompt was developed and refined by the author.

Printed by

UTS Print Services

The editors thank the UTS Faculty of Science for sponsoring the printing of this inaugural issue.

CONTENTS

Foreword **iii**
Professor James Wallman

Editor's note **iv**
YASJ editorial team

Variations of milling parameters and their effect on the volumetric sputtering yield of silicon with the use of a plasma focused ion beam **1**
Willow Bean Otaibi · Research article

Assessing recurrent neural network accuracy and interpretability in breast cancer classification **9**
Michaela Loukas · Research article

Investigation of kinetic energy of .308 projectiles of different masses **19**
Isaac Phillips · Research article

Box modelling the transfer of sulfur on Mars using Earth as a geochemical analogue **26**
Cathy Zhang, Penelope King · Research article

Invention of a new device to optimise air quality for vehicle occupants in Sydney's tunnels: the car canary **38**
Ellie Cole · Research article

How concentration, temperature, and pH affect soapberry's cleaning power compared to commercially available detergents **49**
Alexandra Prokhorov · Research article

Issue acknowledgements **56**

Editorial board **57**

FOREWORD

It is a pleasure to welcome readers to the first issue of the *Young Australians Science Journal*.

Across Australia, students are already asking worthwhile scientific questions, designing investigations and producing work that deserves an audience beyond the classroom. YASJ provides a place for that work to be shared, discussed and built upon.

This first issue reflects the breadth of that research, from materials science and artificial intelligence to planetary science, physics, environmental monitoring and chemistry. I congratulate the student authors, and the teachers, mentors, reviewers and editors who have supported them.

UTS Science is proud to support YASJ, and I hope this inaugural issue is the beginning of a strong national platform for young Australian scientists.



Professor James Wallman
Dean, Faculty of Science
University of Technology Sydney

EDITOR'S NOTE

While one of our editors, James, was sitting down to write this editorial, one of his chickens wandered into the living room. Fortunately, the dog ignored her. The chicken, meanwhile, had found a couple of Bogong moths and was trying to eat them. This distracted James from the editorial.

Bogong moths (*Agrotis infusa*) migrate annually towards the Australian Alps, navigating using the Earth's magnetic field and the night sky (Dreyer et al., 2025). Their alpine aggregations are also an important food source for the endangered mountain pygmy-possum (*Burramys parvus*) (Lownds et al., 2026). This season in 2026 has seen an abundance of Bogong moths, sufficient even to show as rain on the Bureau of Meteorology's radar.

Within a few minutes, one chicken had connected a dog, a moth, astronomical navigation, radar, and one of Australia's smallest possums. It is one of the things we love about science: you notice something, ask a question, and quickly find yourself somewhere you did not expect.

Across the editorial team, we have spent years reading and working with student research. We have watched young people develop questions, learn from others' research, design investigations, wrestle with experiments, and decipher what their evidence means. Their questions regularly take us somewhere we would never have thought to explore.

We have wanted something like the *Young Australians Science Journal* to exist for years because, too often, students do all that work, write it up, hand it in, and that is where it stops. But science is cumulative: one finding should become the starting point for another, with each researcher building on and acknowledging those before them.

Over the years we have seen examples where student research inspired the next cohort. A project using eggshells *[citation not found]* was later extended by another student. The same happened with a project using plant foliage for chelation *[citation not found]*. It was remembered, passed on by a teacher, improved by another student, and tested with different plants. The cycle existed, but it depended on individual teachers and students remembering and passing the work along.

Publication changes that. It gives young researchers a genuine place in the scientific conversation. As authors, their research becomes part of a wider exchange of ideas, open to scrutiny and further investigation. They are not simply practising for some future point when they become scientists. They are taking part in the practices of science now.

Science is a team sport. A project might depend on another student's skills, a teacher who recognises that an idea is worth taking further, or a mentor with the right expertise, equipment or question. It also depends on work done by people the author may never meet. Publication makes those connections visible.

Peer review is part of that conversation too. "Why did you do it that way?" can be annoying after months of doing it that way. But answering might uncover an assumption, strengthen an explanation or make a limitation clearer. Taking young people's research seriously also means taking it seriously enough to question it.

The six papers in this first issue range from ion beams (Otaibi, 2026) and artificial intelligence (Loukas, 2026) to projectile physics (Phillips, 2026), sulfur on Mars (Zhang & King, 2026), tunnel air quality (Cole, 2026) and soapberries (Prokhorov, 2026). It is a wonderfully odd collection, which we quite like.

And perhaps that brings us back to James' chicken. One observation becomes a question, the question connects to something else, and somebody takes it somewhere unexpected.

It brings us true joy to be able to cite these accomplished young scientists here. We hope this journal gives many young scientists somewhere to leave their work, and gives many researchers a starting place for wonderful new ideas.

The YASJ Editorial Team
Dr Lisa Cabral, James Cleaver, Dr Ann Göth, Dr Maria Luisa Gutierrez, Dr Matt Johansen and Dr Lauren McKnight

EDITORIAL REFERENCES

Cole, E. (2026). Invention of a new device to optimise air quality for vehicle occupants in Sydney's tunnels: the car canary. *Young Australians Science Journal*, *1*(1), 38–48. https://doi.org/10.67642/0n025v96

Dreyer, D., Gagnon, Y., Zeil, J., Warrant, E., & el Jundi, B. (2025). Bogong moths use a stellar compass for long-distance navigation at night. *Nature*, *643*, 994–1000. https://doi.org/10.1038/s41586-025-09135-3

Lownds, R. M., Waters, J., Marsland, C., Drinkwater, E., & Umbers, K. D. L. (2026). The Bogong Moth: *Agrotis infusa*. In CABI Books (pp. 526–536). https://doi.org/10.1079/9781800627680.0037

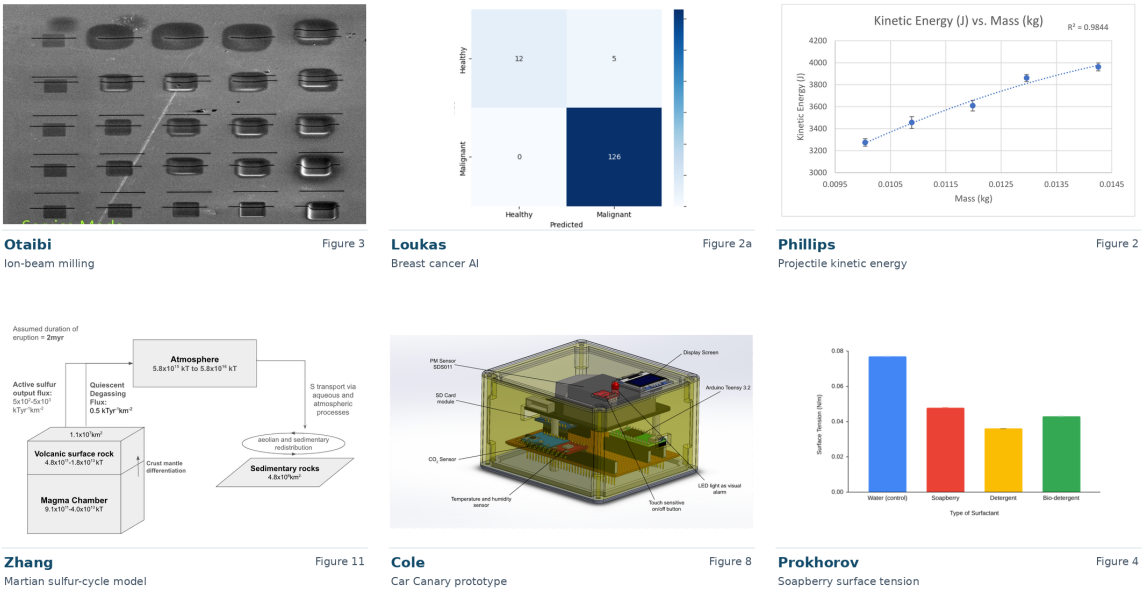
Loukas, M. (2026). Assessing recurrent neural network accuracy and interpretability in breast cancer classification. *Young Australians Science Journal*, *1*(1), 9–18. https://doi.org/10.67642/ye0rwq74

Otaibi, W. B. (2026). Variations of milling parameters and its effect on the volumetric sputtering yield of silicon with the use of a plasma focused ion beam. *Young Australians Science Journal*, *1*(1), 1–7. https://doi.org/10.67642/g1fw2r66

Phillips, I. (2026). Investigation of kinetic energy of .308 projectiles of different masses. *Young Australians Science Journal*, *1*(1), 19–25. https://doi.org/10.67642/ar34df81

Prokhorov, A. (2026). How concentration, temperature, and pH affect soapberry's cleaning power compared to commercially available detergents. *Young Australians Science Journal*, *1*(1), 49–55. https://doi.org/10.67642/psaek593

Zhang, C., & King, P. (2026). Box modelling the transfer of sulfur on Mars using Earth as a geochemical analogue. *Young Australians Science Journal*, *1*(1), 26–36. https://doi.org/10.67642/97wtbw66



Otaibi Figure 3
Ion-beam milling

Loukas Figure 2a
Breast cancer AI

Phillips Figure 2
Projectile kinetic energy

Zhang Figure 11
Martian sulfur-cycle model

Cole Figure 8
Car Canary prototype

Prokhorov Figure 4
Soapberry surface tension

Editorial Figure 1. Research featured in the inaugural issue of the *Young Australians Science Journal* (2026). Figures reproduced from the six research articles cited above.

YASJ Young Australians Science Journal

Variations of milling parameters and their effect on the volumetric sputtering yield of Silicon with the use of a plasma focused ion beam

Willow Bean Otaibi[1]

[1]Bankstown Girls High School, NSW, Australia

ABSTRACT

Volumetric sputtering is a technique used to polish the surface of materials at the atomic level used in the production of semi-conductors and nanotechnology. This study examined the effects of varying milling parameters, specifically voltage and current, on the volumetric sputtering yield of silicon using a plasma focused ion beam with argon gas. The experimental process used a Helios 5 Hydra DualBeam Scanning Electron Microscope Plasma Focused Ion Beam (SEM PFIB) to mill silicon surfaces with various voltage-current combinations. Milled depths were analysed in ImageJ, and volumetric sputtering yields were further calculated. The results demonstrate a statistically significant difference between the effects of voltage and current on the volumetric sputtering yield (ANOVA $p = 0.02$). Current was identified as a significant factor ($p = 0.008$), while voltage alone did not show statistical significance ($p = 0.395$). Accelerating voltages of 12 kV and 30 kV demonstrated the most stable and efficient sputtering processes. The results concluded that the inverse proportionality, $Y_s = \frac{V_{\text{removed}}}{q}$, was present between volumetric sputtering yield and charge, through volume removed, with a significant correlation between their natural logarithms ($p = 0.003$).

Young Australians Science Journal
Volume 1, Issue 1, 2026, pp. 1–7
https://doi.org/10.67642/g1fw2r66

Keywords: plasma focused ion beam; sputtering yield; silicon; milling parameters; voltage; current

Student authors: Willow Bean Otaibi, Year 12

Address correspondence to authors@yasj.org.au

Type: Research Article
Open access: Yes
Licence: This work is licensed under a Creative Commons Attribution-NonCommercial 4.0 International License (CC BY-NC 4.0).
DOI: 10.67642/g1fw2r66

YASJ Editors' Note: Reviewers commended the author's creative approach to measurement and communication. They asked to highlight that in longer term studies it would be traditional to include sequential measurement and the determination of uncertainty. However, this novel approach represents a thorough starting point for further studies.

INTRODUCTION

Plasma Focused Ion Beam (PFIB) milling is used in a range of industries that require high precision levels such as semiconductor production and nanofabrication (Höflich et al., 2023) (Bassim et al., 2014). PFIB milling is used to produce nanometer thin sections of biological specimens for in depth structural and compositional analysis in dental research (House et al., 2022). The rise of advanced technologies, such as artificial intelligence and quantum computing, has further expanded the applications of PFIB milling. The development of next generation silicon-based microchips and nanodevices is reliant on PFIB milling for the precise etching and patterning of optoelectronic nanoscale structures. Furthermore, recent advancements in gas source ion beams (GSIBs), such as He+ PFIBs, offer the potential to replace Ga+ PFIBs due to their ability to achieve nano-resolution imaging with lower implantation damage and pollution (Li et al., 2021).

Volumetric sputtering refers to the amount of surface material removed per unit of electric charge. It involves the ejection of atoms or ions from a

material's surface, typically a metal, caused by the bombardment of energetic ions. Sputtering occurs when these incoming ions transfer energy to the atoms in the solid, leading to the ejection of atoms from the surface. The volumetric sputtering yield can be mathematically expressed as the following :

$$Y_s = \frac{V_{\text{removed}}}{q} \tag{1}$$

Where Y_s is the volumetric sputtering yield, V_{removed} is the volume of the material removed, and q is the charge delivered, expressed in units of $\mu\text{m}^3/\text{nC}$ (Kim et al., 2012).

Milling is a technique defined as the process of removal of material from the surface of a substrate, in this case, with the use of a focused ion beam. *Milling parameters* refers to the variables that govern and affect the outcome of how much material is removed from the substrate. Voltage and current are the two parameters investigated in this study.

The effect of high voltage on the volumetric sputtering yield

High voltages increase the energy of the bombarding ion and are responsible for strong electric fields, consequently increasing the ion acceleration; leading to efficient sputtering and a high sputter rate.

The ion has sufficient momentum to cause a continuous cascade of momentum transfer in the target material (Hashmi, 2016). Therefore, a number of surface atoms within the target will be disturbed and accelerated out of the material. These ejected atoms will travel in a straight line until they deposit on a nearby surface in an inelastic collision. As high voltages increase the ion energy, the collision rate increases, increasing the sputter rate as a result. Refer to Figure 1.

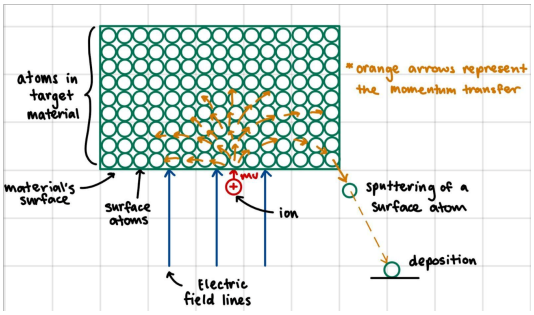


Figure 1. Ion bombardment of a target material, showing sputtering and deposition. The diagram is not to scale.

The effect of beam current on the volumetric sputtering yield

High currents result in a greater flow of charged ions impacting the target material within a given time period. As the current increases, the number of ions striking the target material per second also increases, leading to a high collision rate that results in the ejection of surface atoms from the target material. Consequently, the volumetric sputtering yield increases with beam current, which can be mathematically described as:

$$I = \frac{q}{t} \tag{2}$$

where I is current, q is charge, and t is time.

Despite the extensive interest in gallium ion milling in literature (Kim et al., 2012) (Pastewka et al., 2009), other ion species, such as argon, appear to have been comparatively understudied. While singly-charged gallium ions (Ga+) ions have been the focus of numerous investigations due to their effectiveness in various milling applications, the exploration of alternative ions remains limited.

Silicon was chosen as the material of study due to its importance in semiconductor technology and its extensively reported response to ion beam processing, making it an ideal material for evaluating the effectiveness of different ion species and milling parameters, further providing methods to optimise PFIB processes to establish the scope of upcoming microelectronics (Siew et al., 2021).

This study addresses the understudied areas within the field by using argon as the ion species in a plasma focused ion beam system to examine how varying milling parameters, specifically voltage and current, affect the volumetric sputtering yield of silicon. Understanding the effects of these parameters will contribute to the development of more effective and versatile ion beam tools, leading to advancements in semiconductor manufacturing and other high precision applications.

It is hypothesised that the volumetric sputtering yield of silicon in argon PFIB milling is more strongly influenced by beam current than the accelerating voltage, given the direct dependence of material removal on ion flux and accumulated charge. To examine this relationship, the effects of systematically varying beam current and accelerating voltage on volumetric sputtering yield are investigated under controlled milling conditions.

METHODOLOGY

Preparation of the silicon sample

The silicon sample was prepared through a cleaning process, beginning with 2 minute sonication in acetone to remove contaminants. This was followed by a second sonication in isopropyl alcohol (IPA) to ensure thorough cleansing. Finally, the sample was dried using pressurised nitrogen gas, leaving it free of any remaining residues. This process was completed to reduce the likelihood of any unwanted particles, such as dust or oils, on the silicon surface, which may interfere with the experimental procedure and affect the accuracy of the results.

Preparation of the scanning electron microscope plasma focused ion beam

Calibration of the SEM PFIB (Helios 5 Hydra DualBeam) takes place overnight at the end of each week. This is completed so angle measurements are accurate and to reduce magnification errors (Ghosh, 1975).

Process of imaging with the scanning electron microscope

The Helios SEM was operated through the use of an algorithm, written in Python and automated to mill each area of the silicon sample with specific voltage - current conditions (Table 1). The full code is provided in Supplementary Code S1. The collection of one set of sputtering yield data took place overnight (4 - 8 hour period).

Process of analysis using ImageJ

Each image was uploaded into the free image-analysis software ImageJ. The software was calibrated and used to find the depth of the image by counting each selected pixel. After the depth was found, mathematical calculations were carried out to determine the correct milled depth. The full ImageJ analysis procedure and an example calculation of the corrected milled depth are provided in the supplementary material.

Table 1. Milling depths for silicon using argon ions (n=1). An en dash indicates that a value was unavailable.

Voltage (kV)	Current (nA)	Milled depth (µm)	Volumetric sputter yield (µm^3 nC^{-1})
5	0.2	–	–
5	3.1	0.4962	0.5335
5	4.8	0.7348	0.5103
5	9.3	0.7868	0.2820
5	20.0	0.7690	0.1282
8	0.2	–	–
8	3.9	0.4442	0.3796
8	6.1	0.5812	0.3176
8	9.5	0.4784	0.1679
8	20.0	0.8211	0.1368
10	0.21	–	–
10	1.4	0.0850	0.2024
10	5.9	0.4442	0.2509
10	12.0	0.8211	0.2281
10	35.0	1.1459	0.1091
12	0.21	–	0.0000
12	1.2	0.1371	0.3807
12	4.8	0.5304	0.3684
12	14.0	1.1193	0.2665
12	50.0	2.2576	0.1505
30	0.2	–	–
30	0.7	–	–
30	2.0	0.1536	0.2559
30	7.6	0.4619	0.2026
30	28.0	2.0012	0.2382

RESULTS

Figure 2(a) shows that as charge increases, volumetric sputtering yield decreases for each voltage. This is consistent with the inverse relationship suggested by Equation (1), where $Y_s \propto \frac{1}{q}$. Although the volume removed is not constant, the overall hyperbolic trend remains evident. Localised deviations from this trend are observed at specific data points, including (840, 0.2382) at 30 kV and (177, 0.2509) and (360, 0.2281) at 10 kV, where the volumetric sputtering yield increases rather than decreases.

Figure 2(b) shows that milled depth increased with charge for all voltages. Higher voltages resulted in greater milled depth for equivalent charge, as indicated by the sharp increase in milled depth at 12 kV and 30 kV.

Figure 3 shows the silicon sample after milling under the five accelerating voltages and associated beam-current conditions listed in Table 1.

Statistical analysis

The hypothesis can be restated as null and alternative hypotheses:

H_0: There is no significant difference between the

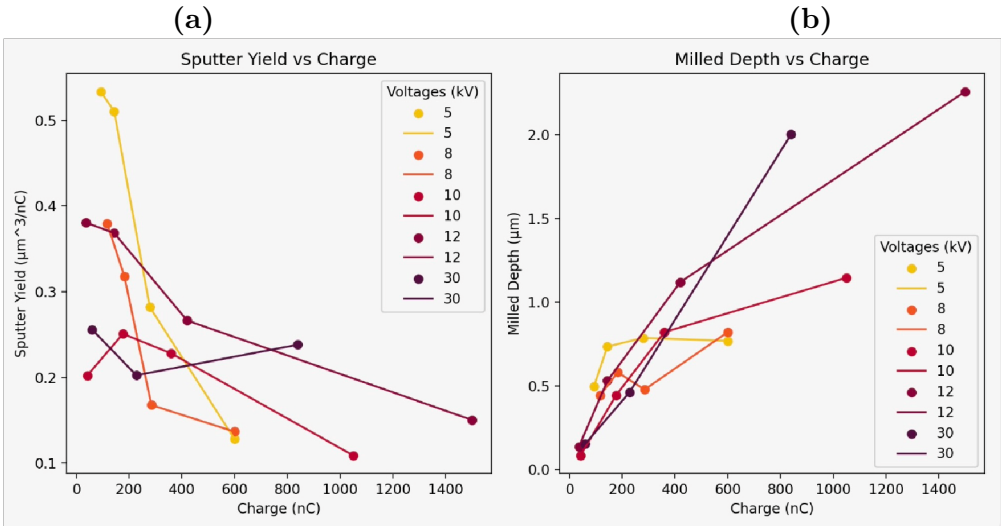


Figure 2. (a) Volumetric sputtering yield of silicon as a function of delivered charge. (b) Milled depth of silicon as a function of delivered charge.

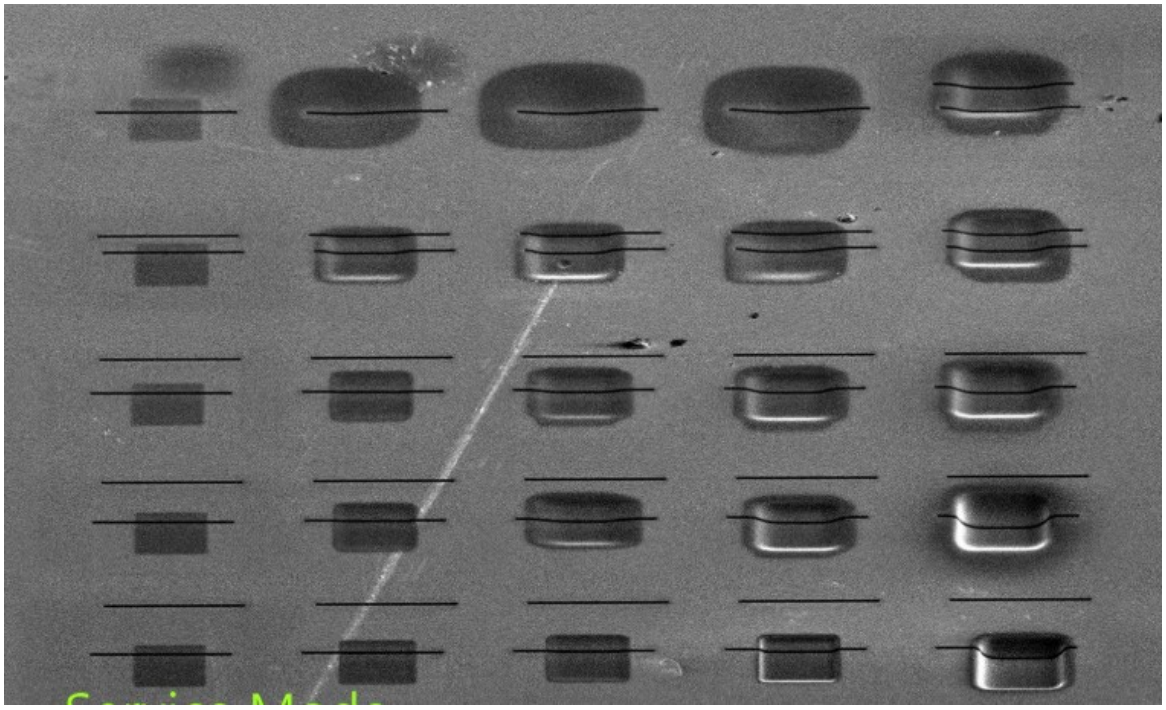


Figure 3. Silicon milled using argon ions. Rows show accelerating voltages of 5, 8, 10, 12 and 30 kV from top to bottom; beam current varies between milled areas (see Table 1).

effect of voltage and current on the volumetric sputtering yield of Silicon.

H_1: There is a significant difference between the effect of voltage and current on the volumetric sputtering yield of Silicon.

The ANOVA significance value was calculated using the multiple linear regression model:

$$Y = \hat{\beta}_0 + \hat{\beta}_1 X_1 + \hat{\beta}_2 X_2 + \epsilon$$

Using the reported units, the fitted multiple linear regression model is:

$$Y_s = 0.36627 - 0.00536I - 0.00247V \pm 0.04697 \quad (3)$$

where Y_s is measured in $\mu m^3/nC$, I is beam current in nA, and V is accelerating voltage in kV.

The null hypothesis was rejected, as the ANOVA returned a significance value of 0.02 ($\alpha = 0.05$) (Table 2), indicating a significant difference between the effect of voltage and current on the volumetric sputtering yield of silicon. Current was a significant factor affecting the volumetric sputtering yield (p = 0.008), while voltage alone

did not show statistical significance (p = 0.395) (Table 2).

Table 2. p-values for variables associated with volumetric sputtering yield and the ANOVA significance for voltage and current.

Y-variable	X-variable	p	ANOVA
Volumetric sputtering yield	Voltage	0.395	0.02 for voltage and current
	Current	0.008	
	Milled depth	0.183	
	Charge	0.008	–
Natural log of volumetric sputtering yield	Natural log of charge	0.003	–

Using the fitted linear relationship from the log-log plot demonstrated in Figure 4,

$$\ln(Y_s) = -0.2778 \ln(q) + 0.1044$$

the volumetric sputtering yield can be expressed as

$$Y_s = 1.1100\, q^{-0.2778}.$$

This relationship suggests a power-law dependence of volumetric sputtering yield on charge, which may be approximated as

$$Y_s \propto q^{-1/3} \quad \text{or} \quad Y_s \propto q^{-1/4}$$

corresponding to Equations (4) and (5), respectively.

$$Y_s \approx \frac{a}{q^{1/3}} \tag{4}$$

$$Y_s \approx \frac{a}{q^{1/4}} \tag{5}$$

Figure 4 demonstrates a linear relationship between the natural logarithm of volumetric sputtering yield and natural logarithm of charge, indicating that the data follows a power-law model. Additional sampling and analysis are required to determine whether Equation (4) or Equation (5) provides the more accurate description.

The R^2 value of Figure 4 is higher than the R^2 value of Figure 5 (42% compared to 34%), suggesting that the log-log representation provides a better fit to the data than the linear scale. The remaining unexplained variance indicates that additional parameters not investigated in this study also have an influence on the volumetric sputtering yield.

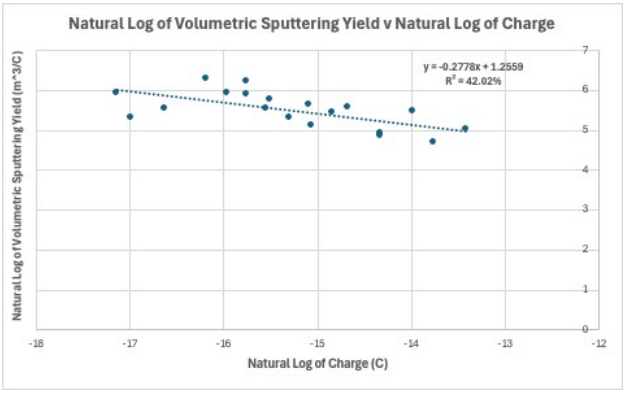


Figure 4. Natural logarithm of volumetric sputtering yield as a function of the natural logarithm of delivered charge.

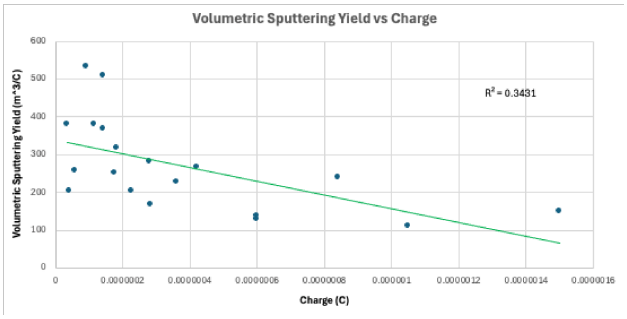


Figure 5. Volumetric sputtering yield as a function of delivered charge, with a fitted trendline.

DISCUSSION

Volumetric sputtering yield and milled depth relationship

Figure 2 shows that the higher the voltage, the more stable and efficient the sputtering and milling processes are, as shown by the measured volumetric sputtering yield and the greater milled depth at high voltages (12 kV and 30 kV).

Inconsistencies in sputtering are shown by the sharp decrease in the volumetric sputter yield value regarding a voltage of 5 kV. This inconsistency can be attributed to redeposition of the sputtered material, surface damage induced by the ion beam, and surface roughening. These factors heavily reduce the efficiency of the sputtering process as milling progresses, leading to low volumetric sputtering yield. The same phenomena have been observed in similar ion beam studies regarding milling of silicon. Prolonged milling introduces complexities and inconsistencies which ultimately decrease the volumetric sputtering yield (Jamaludin et al., 2013).

Further graphical analysis

The volumetric sputter yield generally decreased with increasing charge across all voltages (Figure 2(a)). The rapid drop at lower voltages (5 kV and 8 kV) suggests that the energy provided by the ion beam was insufficient in order to maintain efficient sputtering as charge accumulates. In contrast, the decrease in the volumetric sputter yield was more stable at high voltages as this provided more kinetic energy because the ions carry greater momentum. This allowed them to sustain material removal even as the charge increased, leading to a more stable volumetric sputter yield.

Figure 2(b) shows that high voltages and high charge values ed in a greater amount of material removal, suggesting that they provided enough energy to maintain a high milling rate as charge increased. This may be due to more energetic ions penetrating deeper into the target material, resulting in a more effective milling process.

The SEM PFIB is the industry standard for high precision milling and analysis, ensuring precise and relevant measurements (Kim et al., 2018) (Liu et al., 2020). To minimise potential sources of measurement error, the used SEM was routinely calibrated.

This experiment successfully isolated the effect of the independent parameters, voltage and current, on volumetric sputtering yield by employing argon as the ion species across all milling conditions. The silicon target material and image analysis methodology were kept consistent throughout the study, minimising variability.

The data collected closely aligned with theoretical expectations, with higher accelerating voltages producing more stable volumetric sputtering yields. As shown in Figure 2, the observed trends are consistent with the relationships described by Equation (1), confirming an inverse proportionality between volumetric sputtering yield and delivered charge. Rearranging Equation (1) allows the dependence between milled depth and charge to be expressed as Equation (4), indicating a direct proportionality between milled depth and charge. This proportionality is reflected in Figure 2(b), where the milled depth increased with increasing charge delivered by the ion beam.

$$Y_s = \frac{V_r}{q}$$

where the volume removed is given by $V_r = L \times w \times d_m$.

$$d_m = \frac{Y_s q}{Lw} \tag{6}$$

where d_m is the corrected milled depth, Y_s is the volumetric sputtering yield, q is the delivered charge, and L and w are the length and width of the milled area, respectively.

$$\therefore d_m \propto q$$

Both graphs align with their respective mathematical models, providing initial validation of the observed relationships between charge, volumetric sputtering yield, and milled depth. However, further validation would require a larger sample size in order to reduce statistical uncertainty and improve the statistical confidence of the results.

Variations in the volumetric sputtering yield, particularly at lower voltages, suggest potential sources of uncertainty. These variations may arise from surface roughening, redeposition of sputtered material, and ImageJ-based depth measurement uncertainty. Measurement uncertainty was reduced by using high precision instruments.

The experimental process lacked repetition due to time and resource constraints. The nature of this study required meticulous calibration and execution, as the experimental workflow involved multiple stages, including sample preparation, milling, and imaging. Each session required approximately 4-8 hours for data collection, including overnight processes for imaging and depth measurement with the focused ion beam. The availability of the Helios 5 Hydra DualBeam SEM PFIB was limited, as the instrument was in high demand. Further work would benefit from a large sample size and increased repetition. Despite these limitations, the image analysis methodology remained consistent across all measurements, and the observed trends in each graph aligned with their expected mathematical models.

Future work

Future work should include testing with more ion species, like investigating xenon, nitrogen and carbon, and having larger sample sizes incorporating a broader range of voltage and current values and repeated trials for each ion species. Further analysis of the mathematical models presented in Figures 4 and 5 would also help determine whether Equation (4) or Equation (5) more accurately describes the observed behaviour.

CONCLUSION

This study investigated the effects of varying milling parameters on the volumetric sputtering yield of silicon using a plasma-focused ion beam using an argon ion species. The results demonstrated a significant difference between the effects of voltage and current on the volumetric sputtering yield, with an ANOVA significance value of 0.02 ($p < 0.05$). Higher voltages (12 kV and 30 kV) resulted in more consistent sputtering behaviour, as evidenced by greater milled depths and consistent volumetric sputtering yields. The volumetric sputtering yield showed an inverse relationship with charge, decreasing as charge increases across all voltages. Current showed to be a significant factor, affecting the volumetric sputtering yield ($p = 0.008$), while voltage alone did not show statistical significance ($p = 0.395$). The natural log of charge also demonstrated a significant relationship with the natural log of volumetric sputtering yield ($p = 0.003$), although more work is needed to confirm this relationship. These findings contribute to the understanding of ion beam milling processes and have implications for optimising parameters in semiconductor manufacturing and other high-precision applications which include semiconductor manufacturing, quantum computing, and nanodevice fabrication.

ACKNOWLEDGEMENTS

I thank TMOS for making their laboratories and resources available for this study; Dr Hossein Alijani Alijanvand for his guidance, and for supplying the data from the presented experiments; Dr Lisa Cabral for providing essential coaching and guidance throughout the year; and Mr Daniel Golestan for his support and guidance throughout the entirety of my report as my school teacher.

SUPPLEMENTARY MATERIAL

The supplementary material accompanying this article contains the chemical risk assessment, detailed ImageJ analysis procedure, worked calculations for corrected milled depth and volumetric sputtering yield, Python code used to automate the PFIB milling process, and the full experimental dataset.

The supplementary PDF is available with the online article at https://doi.org/10.67642/g1fw2r66.

REFERENCES

Bassim, N., Scott, K., & Giannuzzi, L. A. (2014). Recent advances in focused ion beam technology and applications. *MRS Bulletin*, *39*(4), 317–325. https://doi.org/10.1557/mrs.2014.52

Ghosh, S. K. (1975). Photogrammetric calibration of a scanning electron microscope. *Photogrammetria*, *31*(3), 91–114. https://doi.org/10.1016/0031-8663(75)90008-3

Hashmi, M. S. J. (Ed.).(2016). *Comprehensive materials finishing*. Elsevier. https://doi.org/10.1016/c2014-1-03366-2

Höflich, K., Hobler, G., Allen, F. I., Wirtz, T., Rius, G., McElwee-White, L., Krasheninnikov, A. V., Schmidt, M., Utke, I., Klingner, N., Osenberg, M., Córdoba, R., Djurabekova, F., Manke, I., Moll, P., Manoccio, M., De Teresa, J. M., Bischoff, L., Michler, J., … Hlawacek, G. (2023). Roadmap for focused ion beam technologies. *Applied Physics Reviews*, *10*(4). https://doi.org/10.1063/5.0162597

House, K. L., Pan, L., O'Carroll, D. M., & Xu, S. (2022). Applications of scanning electron microscopy and focused ion beam milling in dental research. *European Journal of Oral Sciences*, *130*(2). https://doi.org/10.1111/eos.12853

Jamaludin, F. S., Mohd Sabri, M. F., & Said, S. M. (2013). Controlling parameters of focused ion beam (FIB) on high aspect ratio micro holes milling. *Microsystem Technologies*, *19*(12), 1873–1888. https://doi.org/10.1007/s00542-013-1912-y

Kim, C-S., Ahn, S.-H., & Jang, D.-Y. (2012). Review: Developments in micro/nanoscale fabrication by focused ion beams. *Vacuum*, *86*(8), 1014–1035. https://doi.org/10.1016/j.vacuum.2011.11.004

Kim, S., Fröch, J. E., Christian, J., Straw, M., Bishop, J., Totonjian, D., Watanabe, K., Taniguchi, T., Toth, M., & Aharonovich, I. (2018). Photonic crystal cavities from hexagonal boron nitride. *Nature Communications*, *9*(1). https://doi.org/10.1038/s41467-018-05117-4

Li, P., Chen, S., Dai, H., Yang, Z., Chen, Z., Wang, Y., Chen, Y., Peng, W., Shan, W., & Duan, H. (2021). Recent advances in focused ion beam nanofabrication for nanostructures and devices: Fundamentals and applications. *Nanoscale*, *13*(3), 1529–1565. https://doi.org/10.1039/d0nr07539f

Liu, J., Niu, R., Gu, J., Cabral, M., Song, M., & Liao, X. (2020). Effect of ion irradiation introduced by focused ion-beam milling on the mechanical behaviour of submicron-sized samples. *Scientific Reports*, *10*(1). https://doi.org/10.1038/s41598-020-66564-y

Pastewka, L., Salzer, R., Graff, A., Altmann, F., & Moseler, M. (2009). Surface amorphization, sputter rate, and intrinsic stresses of silicon during low energy Ga+ focused-ion beam milling. *Nuclear Instruments and Methods in Physics Research Section B: Beam Interactions with Materials and Atoms*, *267*(18), 3072–3075. https://doi.org/10.1016/j.nimb.2009.06.094

Siew, S. Y., Li, B., Gao, F., Zheng, H. Y., Zhang, W., Guo, P., Xie, S. W., Song, A., Dong, B., Luo, L. W., Li, C., Luo, X., & Lo, G.-Q. (2021). Review of silicon photonics technology and platform development. *Journal of Lightwave Technology*, *39*(13), 4374–4389. https://doi.org/10.1109/jlt.2021.3066203

Study Science and Mathematics at UTS

Turn curiosity into real-world impact.



Students in a UTS learning environment. Image: UTS Science

Hands-on learning
State-of-the-art labs and industry connection.

Real-world challenges
Tackle issues that matter.

A positive impact
Be part of a healthier, more sustainable future.

YASJ Young Australians Science Journal

Assessing recurrent neural network accuracy and interpretability in breast cancer classification

Michaela Loukas[1]

[1]Marist Catholic College Penshurst, Sydney, New South Wales, Australia

ABSTRACT

Ribonucleic acid sequencing-based gene expression profiling enables molecular-level cancer diagnosis. However, most machine learning approaches lack the interpretability required for clinical adoption. This investigation examined how accurately a recurrent neural network could classify gene expression data to distinguish malignant from healthy breast tissue, determine molecular subtypes, and reveal key gene expression patterns. It was hypothesised that a multi-task recurrent neural network would achieve high diagnostic accuracy while providing gene-level interpretability. A bidirectional long short-term memory model was trained on The Cancer Genome Atlas Breast Cancer dataset (1,109 malignant and 109 solid tissue normal samples) following extensive preprocessing, including reducing 20,530 genes to 5,000 features. The model achieved 96.5% accuracy for malignancy classification, with 100% sensitivity and 70.6% specificity, and 75.4% accuracy for molecular subtype classification. Explainability analysis identified transferrin, adenosine diphosphate ribosylation factor interacting protein 2, and moesin as key genes, highlighting roles of iron metabolism and cytoskeletal regulation. These findings demonstrate that recurrent neural networks can achieve clinically applicable accuracy for transcriptomic breast cancer diagnosis whilst providing interpretable, gene-level insights, thereby addressing critical barriers to artificial intelligence adoption in oncology.

Young Australians Science Journal
Volume 1, Issue 1, 2026, pp. 9–18
https://doi.org/10.67642/ye0rwq74

Keywords: breast cancer; RNA sequencing; recurrent neural networks; bidirectional long short-term memory; explainable artificial intelligence; SHAP

Student authors: Michaela Loukas, Year 12

Address correspondence to authors@yasj.org.au

Type: Research Article
Open access: Yes
Licence: This work is licensed under a Creative Commons Attribution-NonCommercial 4.0 International License (CC BY-NC 4.0).
DOI: 10.67642/ye0rwq74

YASJ Editors' Note: Reviewers commended the integration of transcriptomic data, deep learning, and explainable artificial intelligence, particularly the connection between model performance and biologically interpretable gene-level findings. They noted that this computational proof of concept uses a single, imbalanced cohort, and that external validation and comparison with simpler baseline models would strengthen the findings.

INTRODUCTION

Breast cancer is the most frequently diagnosed malignancy among women worldwide and remains a leading cause of cancer-related mortality, accounting for approximately 15% of female cancer deaths globally (Zhang et al., 2025). In Australia, annual diagnoses have increased from approximately 13,500 cases in 2000 to over 20,000 in 2024, with mortality also rising despite advances in imaging, pathology, and treatment (Australian Institute of Health and Welfare, 2025). "While the overall 5-year survival rate in stage 1 breast cancer is 99%, it drops to 27% when distant metastases are detected" (Burcu et al., 2023). This highlights the need for earlier, molecular-level diagnostic strategies which detect malignancy before overt morphological change.

Breast cancer is biologically heterogeneous and

comprises distinct molecular subtypes: luminal A, luminal B, human epidermal growth factor receptor 2-enriched (HER2-enriched), and basal-like. These principal subtypes are currently classified using immunohistochemistry (IHC) markers for oestrogen, progesterone, and HER2 receptors (Orrantia-Borunda et al., 2022). However, IHC oversimplifies tumour biology and fails to capture transcriptional heterogeneity. Gene expression profiling reveals earlier and more nuanced distinctions, such as elevated estrogen-receptor 1 (ESR1) and guanine-adenine-thymine-adenine binding protein 3 (GATA3) in luminal A tumours, increased marker of proliferation Ki-67 (MKI67) in luminal B tumours, erb-b2 receptor tyrosine kinase 2 (ERBB2) amplification in HER2-enriched disease, and tumour protein p53 (TP53) mutations in basal-like cancers (Orrantia-Borunda et al., 2022). These transcriptional signatures often precede phenotypic changes, positioning gene-level analysis as a powerful tool for early detection.

Ribonucleic acid sequencing (RNA-seq) enables high-resolution transcriptomic profiling and surpasses microarrays in sensitivity, range, and the ability to detect low-abundance and novel transcripts (Mantione et al., 2014). Advances in high-throughput sequencing system (HiSeq) technologies have substantially reduced costs (Levy & Boone, 2019). Despite its biological value, clinical adoption remains limited due to the computational challenges posed by high-dimensional datasets and the need for robust analytical frameworks to extract clinically meaningful insights. (Acedo-Terrades et al., 2025).

Deep learning (DL) approaches have shown promise in cancer classification, particularly in medical imaging (Kim et al., 2021). Convolutional neural networks (CNN) have achieved high diagnostic accuracy using imaging modalities (Yu et al., 2023). However, such methods often rely on high-radiation or late-stage morphological data, limiting their suitability for early detection (Yu et al., 2023). Recurrent neural networks (RNN), particularly those incorporating bidirectional long short-term memory units (Bi-LSTM), are well-suited to modelling complex dependencies within sequential data (Schuster & Paliwal, 1997) and have demonstrated strong predictive performance in oncology (Dasgupta et al., 2025). Nonetheless, most existing RNN applications exclude transcriptomic inputs (Kim et al., 2021).

Another barrier to clinical translation is the limited interpretability of DL models. In oncology, where decisions are high-stakes, opaque "black-box" predictions undermine trust and ethical deployment (Islam et al., 2024). Explainable artificial intelligence (AI) techniques such as SHapley Additive exPlanations (SHAP) enable gene-level attribution, allowing model predictions to be interpreted and contextualised within established biological frameworks (Lundberg & Lee, 2017). While some studies have applied DL to gene expression data, few integrate explainability, and even fewer employ large, well-annotated datasets such as The Cancer Genome Atlas (TCGA) (Alharbi & Vakanski, 2023).

Recent transcriptomic studies have also identified emerging breast cancer biomarkers, including transferrin (TF), adenosine diphosphate ribosylation factor interacting protein 2 (ARFIP2), and moesin (MSN), which are implicated in iron metabolism, cytoskeletal regulation, and treatment resistance but remain absent from standard clinical panels (Alhaddad et al., 2025; Shi et al., 2024). The detection and validation of such subtle, non-canonical signals highlight the need for models that combine predictive accuracy with biological interpretability.

This study therefore asks whether a RNN trained on RNA-seq gene expression data can accurately and interpretably classify breast cancer and its molecular subtypes. The aim of this research was to develop a Bi-LSTM RNN using RNA-seq data from TCGA dataset to distinguish malignant from healthy tissue and identify molecular subtypes while providing gene-level explanations. It was hypothesised that integrating biologically informed preprocessing, recurrent DL architecture, and explainable AI would yield clinically relevant diagnostic accuracy while revealing biologically meaningful gene expression drivers. Collectively, this work demonstrates the potential of interpretable DL to address key limitations in current breast cancer diagnostics and advance the clinical adoption of transcriptomic AI models.

MATERIALS AND METHODS

Dataset selection and computational infrastructure

Gene expression data were obtained from The Cancer Genome Atlas Breast Invasive Carcinoma (TCGA-BRCA) cohort, comprising 1,109 primary breast tumours and 109 solid tissue normal sam-

ples (total n = 1,218), sequenced using the Illumina HiSeq platform (The Cancer Genome Atlas Program, 2018). Sample identities were assigned using TCGA barcode conventions, where "-01" denoted primary tumours, "-06" revealed metastatic samples and "-11" indicated normal breast tissue. All analyses were conducted in Python 3.10 using TensorFlow for DL implementation. Model training and experimentation were performed in Google Colab to enable graphics processing unit acceleration and reproducibility.

Batch effect assessment and data cleansing

To assess latent technical variation, dimensionality reduction was performed using t-distributed stochastic neighbour embedding (t-SNE). Samples were annotated by technical covariates including sequencing centre, tissue source site, vial number, and collection indicators. No batch effects were detected, hence, batch correction was not applied. Principal component analysis (PCA) was additionally used as a confirmatory linear assessment of variance structure. Outlier detection was conducted using Mahalanobis distance to identify samples with multivariate expression profiles deviating from the cohort centroid. Statistical outliers were subsequently contextualised through cohort-level validation against canonical oncogenes, tumour suppressors, and housekeeping genes using fold-change analysis. Three filtering strategies were evaluated, and the final dataset was selected to maximise molecular subtype separation while preserving sufficient sample size for model training.

Gene filtering and feature selection

Low-information genes were removed using a dual threshold approach, excluding genes with variance < 0.1 and those within the lowest 10% of mean absolute expression. This retained 18,477 genes while preserving biologically relevant tumour suppressors and regulatory genes. Differential expression analysis was conducted using two-sample Student's t-tests to compare malignant versus normal tissue and between molecular subtypes. Genes with $p < 0.05$ and $|\log_2 \text{fold change}| > 0.585$ were considered significant, yielding 15,925 differentially expressed genes. To reduce redundancy, Pearson correlation filtering was applied with a threshold of $|r| > 0.85$. Highly correlated gene pairs were assessed using F-tests to confirm comparable variance. Genes were then ranked using an analysis-of-variance F-statistic to quantify discriminatory power across molecular subtypes. The top 5,000 genes were retained for model input, resulting in an effective sample-to-feature ratio suitable for DL.

Neural network architecture and training

Data were standardised and stratified into training (70%), validation (15%), and test (15%) sets. Input data were reshaped to a (samples, 1, features) format. A multi-task Bi-LSTM RNN was constructed, consisting of two Bi-LSTM layers (128 and 64 units), followed by dropout (0.30), a dense layer (32 units, rectified linear unit (ReLU) activation), and dual output layers for binary (sigmoid) and subtype (softmax) classification. L2 regularisation ($\lambda = 0.001$) was applied. The model was trained using the Adam optimiser (learning rate = 0.001) with early stopping (patience = 5 epochs). The final architecture comprised 905,495 trainable parameters.

Model evaluation and interpretability

Performance was evaluated using accuracy, sensitivity, specificity, precision, and F1 score, computed with sklearn.metrics. Confusion matrices were generated for both malignancy and subtype classification. Model interpretability was assessed using SHAP, with beeswarm plots used to identify gene-level contributions to predictions. SHAP-identified genes were cross-referenced with established and emerging breast cancer biomarkers to assess biological plausibility.

RESULTS

To ensure that downstream modelling was performed on biologically coherent and statistically reliable data, a systematic dataset curation and feature selection process was undertaken to improve sample-level quality while preserving discriminative molecular signal. Four sample filtering strategies were compared - unfiltered, conservative, moderate, and strict - each removing samples based on increasing confidence of biological implausibility or transcriptional dysregulation (Table 1).

Dataset quality was quantified using clustering separation score, compactness, and their ratio as an overall quality metric.

Progressive filtering resulted in monotonic im-

Table 1. Comparative analysis of dataset filtering strategies

Dataset	Samples	Separation Score	Compactness	Quality Ratio	Sample Retention
Original	956	78.80	331.21	0.24	100%
Conservative	955	78.89	332.85	0.24	99.9%
Moderate	952	80.30	289.27	0.28	99.6%
Strict	932	83.29	271.81	0.31	97.5%

provements in clustering quality, with the separation score increasing from 78.80 in the unfiltered dataset to 83.29 under strict filtering, and the quality ratio increasing from 0.24 to 0.31 (Table 1). However, increasing stringency was associated with reduced sample retention, decreasing from 100% in the unfiltered dataset to 97.5% under strict filtering. Conservative filtering yielded minimal improvement in clustering quality despite near-complete sample retention (99.9%), indicating that removal of only the most extreme outliers was insufficient to substantially improve dataset structure.

Visualisation using t-SNE demonstrated progressive refinement of molecular subtype clustering with increasing filtering stringency (Figure 1a).

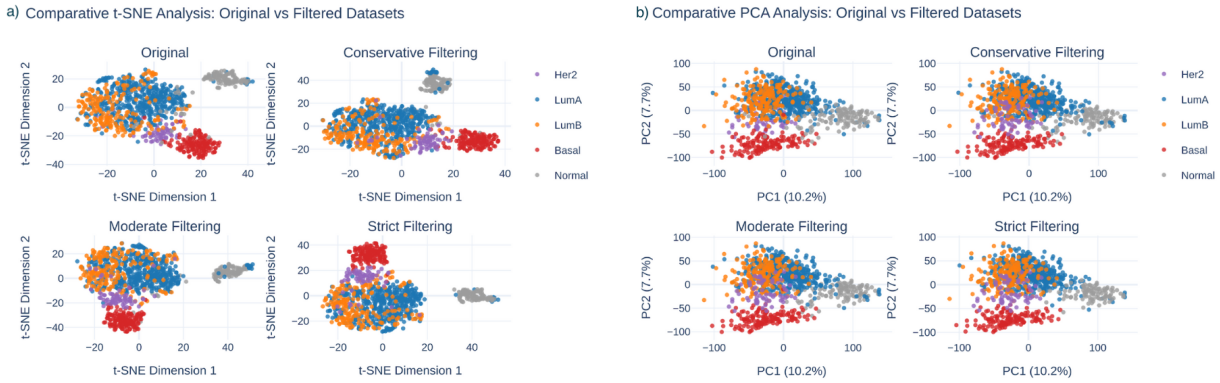


Figure 1. Effect of Progressive Filtering on TCGA-BRCA Sample Structure. (a) Comparative t-SNE plots of TCGA-BRCA sample clustering: original dataset vs. increasing filtering stringency (conservative, moderate, strict). More stringent filtering yields more defined clusters (colours denote subtype: grey = normal, blue = Luminal A, orange = Luminal B, purple = HER2-enriched, red = Basal-like). (b) Comparative PCA of Dataset Filtering Strategies. Each point represents a sample, projected onto the first two principal components (PC1 and PC2), which together explain 17.9% of total variance (PC1: 10.2%, PC2: 7.7%).

The unfiltered dataset exhibited diffuse and overlapping subtype clusters, whereas moderate filtering produced clearer separation between normal tissue, luminal, HER2-enriched, and basal-like samples while preserving expected areas of biological overlap. Although strict filtering produced the most compact clusters, boundaries appeared overly discrete, suggesting potential over-pruning of biologically valid intermediate samples. PCA was used as a complementary quality control measure and showed broadly consistent subtype organisation across filtering strategies, with the first two components explaining 17.9% of total variance (PC1: 10.2%, PC2: 7.7%; Figure 1b).

Based on the combined quantitative metrics and clustering visualisations, the moderate filtering strategy was selected for all downstream analyses as it achieved substantial improvement in dataset quality while retaining 99.6% of samples, thereby balancing data integrity with statistical power.

Following sample-level curation, feature selection reduced the dataset from 20,530 genes to 5,000 discriminative features (Table 2).

Table 2. Gene filtering pipeline results

Step	Method	Threshold / Criteria	Genes Retained
Initial Count	-	-	20 530
Low-Information Selective Filtering	Removing genes with mean absolute expression $\leq \pm$ 0.10	Var Threshold: 0.10	18 477
Differential Expression Analysis	T-test ($p < 0.05$)	$p < 0.05$	15 925
Quantile Normalisation	Standardised variance	$1.001 \rightarrow 0.088$	-
Signal-to-Noise (SNR) Filtering	SNR ratio	SNR > 1.0	492
Correlation filtering	Pearson correlation	$r > 0.85$	15 285
F-statistic ranking	Top discriminative features	Top 5 000	5 000

Differential expression analysis identified 15,925 significantly dysregulated genes between classes ($p < 0.05$, $\alpha = 0.05$), providing a statistically supported basis for dimensionality reduction. To assess biological validity of the final feature set, retention of established breast cancer biomarkers was evaluated (Table 3).

Table 3. Biomarker retention in final feature set

Biomarker Category	Total	Retained	Retention (%)	Key Examples Retained
PAM 50 Genes	10	3	30.0	ESR1, PGR, ERBB2
Tumour Suppressors	7	4	57.1	BRCA1, BRCA2, PTEN, CDKN2A
Oncogenes	6	3	50.0	MYC, CCND1, EGFR
Luminal Markers	5	5	100.0	ESR1, PGR, GATA3, FOXA1, TFF1
Basal Markers	6	2	33.3	EGFR, FOXC1
HER2-Enriched Pathway	5	3	60.0	ERBB2, PGAP3, LASP1
Overall	39	20	51.3	-

Binary classification of malignant versus normal breast tissue achieved an overall accuracy of 96.5% (Figure 2a).

All malignant samples were correctly classified (sensitivity = 100%), while 12 of 17 normal samples were correctly identified (specificity = 70.6%), resulting in five false positive predictions and no false negatives. Performance metrics reflected balanced classification despite class imbalance, with a weighted F1-score of 0.96 (Table 4).

Table 4. Malignancy classification performance metrics

	Precision	Recall	F1-Score
Healthy	1.00	0.71	0.83
Malignant	0.96	1.00	0.98
Accuracy	-	-	0.97
Macro Average	0.98	0.85	0.90
Weighted Average	0.97	0.97	0.96

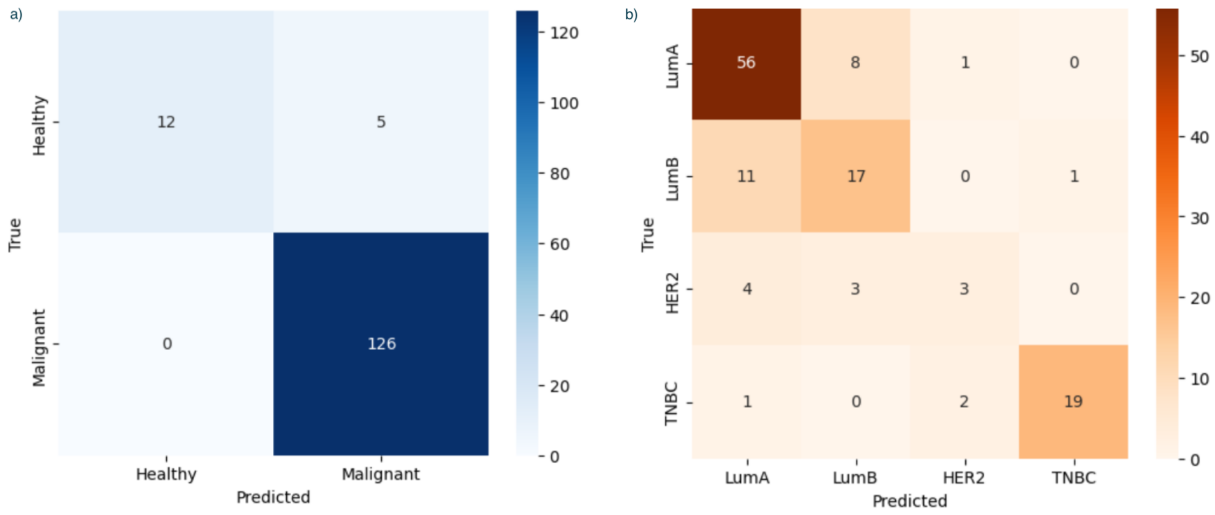


Figure 2. Confusion Matrices For Breast Cancer Classification. (a) Confusion Matrix for Malignancy Classification. The matrix demonstrates high sensitivity (1.00) for malignant tissue detection with minimal false positive predictions. (b) Confusion Matrix for Molecular Subtype Classification. Note: TNBC (Triple-Negative Breast Cancer) labels represent the Basal-like subtype.

Subtype classification achieved an overall accuracy of 75.4%, with performance varying across molecular subtypes (Figure 2b). Luminal A and basal-like tumours demonstrated the highest classification performance, with recall values of 86.2% and 86.4% respectively (Table 5).

Table 5. Molecular subtype classification performance metrics

	Precision	Recall	F1-Score
Luminal A	0.78	0.86	0.82
Luminal B	0.61	0.59	0.60
HER-2	0.50	0.30	0.38
Basal-Like	0.95	0.86	0.90

Luminal B exhibited intermediate performance (recall = 58.6%), while the HER2-enriched subtype showed the lowest recall (30.0%). Misclassification patterns were dominated by confusion between luminal A and luminal B subtypes, which together accounted for 61.3% of all classification errors (Figure 2b). Conversely, basal-like tumours showed comparatively low overlap with other subtypes.

Substantial gene overlap was observed across subtypes, particularly among luminal and HER2-enriched tumours, whereas basal-like predictions were driven by more distinct features (Figure 3).

Across all subtypes, TF emerged as a consistently influential feature, while ARFIP2 and Bardet-Biedl syndrome 12 (BBS12) appeared in multiple subtype signatures. In contrast, several genes demonstrated subtype exclusivity, including cadherin 19 (CDH19), hydroxysteroid 17-beta dehydrogenase 8 (HSD17B8), and kelch like family member 13 (KLHL13) for luminal A; serine peptidase inhibitor Kazal type 4 (SPINK4) and Solute Carrier Family 9 Member A3 regulator 1 (SLC9A3R1) for luminal B; neurofilament light chain (NEFL), ribosomal protein L26 like 1 (RPL26L1), and MSN for HER2-enriched tumours; and maternally expressed 3 (MEG3), delta/notch like epidermal growth factor repeat containing (DNER), and purinergic receptor P2X 6 (P2RX6) for basal-like tumours (Table 6).

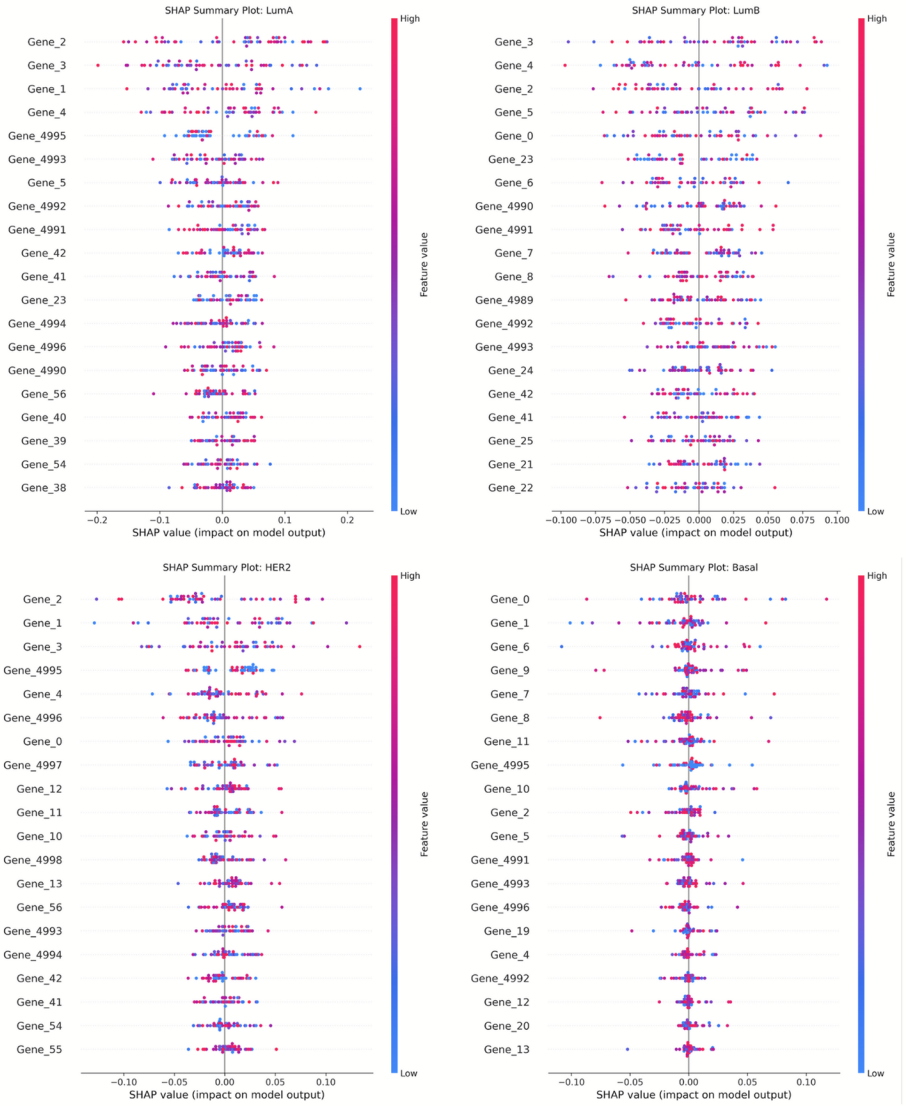


Figure 3. SHAP summary plots showing shared and subtype-specific gene contributions across breast cancer molecular subtypes. Luminal A (top left), Luminal B (top right), HER2-enriched (bottom left), and Basal-like (bottom right).

Table 6. Top 10 SHAP-identified genes by molecular subtype

Rank	Corresponding Genes			
	Luminal A	**Luminal B**	**HER2-Enriched**	**Basal-Like**
1	TF	ARFIP2	TF	ACAT2
2	ARFIP2	HYMAI	BBS12	BBS12
3	BBS12	TF	ARFIP2	SSPN
4	HYMAI	BTRC	LHCGR	MEG3
5	LHCGR	ACAT2	HYMAI	PSENEN
6	HSD17B8	SPINK4	NEFL	DNER
7	BTRC	SSPN	ACAT2	HNRPAB
8	KLHL13	SLC9A3R1	RPL26L1	LHCGR
9	PER2	PER2	MSN	P2RX6
10	CDH19	PSENEN	HNRNPAB	TF

DISCUSSION

This investigation evaluated whether a RNN trained on RNA-seq gene expression data could accurately distinguish malignant from healthy breast tissue, classify molecular subtypes, and identify key genes driving these predictions. Overall, the model achieved high diagnostic performance, demonstrating 96.5% accuracy and 100% sensitivity for malignancy detection (Figure 2a), alongside moderate specificity (70.6%). Subtype classification accuracy reached 75.4% (Figure 2b), with performance varying across molecular subtypes. Explainability analysis revealed biologically plausible gene signatures that aligned with both established and emerging breast cancer biomarkers (Figure 3). Collectively, these findings support the hypothesis that transcriptomic differences between healthy and malignant tissue can be leveraged by RNNs to enable accurate and interpretable breast cancer classification.

The absence of false negatives in malignancy classification is clinically significant, as it indicates that no malignant samples were incorrectly classified as healthy (Figure 2a). While specificity was lower, resulting in some false positives, this trade-off is acceptable in a screening or triage context where sensitivity is prioritised. Importantly, the model operates on molecular data and therefore has the potential to detect malignancy prior to observable anatomical changes, distinguishing it from imaging-based approaches such as CNN-driven breast imaging systems (Yu et al., 2023). These results suggest that RNA-seq-based models could complement existing diagnostic workflows as an early molecular screening tool rather than a definitive standalone test.

Subtype classification performance reflected known biological relationships between breast cancer subtypes. Luminal A and basal-like tumours were classified with the highest accuracy, while luminal B and HER2-enriched subtypes exhibited greater misclassification. Notably, 61.3% of subtype classification errors occurred between luminal A and luminal B tumours (Figure 2b). This pattern is consistent with the biological continuum between these oestrogen receptor-positive subtypes, which share hormone-regulated pathways and differ primarily in proliferation-associated gene expression (Orrantia-Borunda et al., 2022). Consequently, the observed confusion is likely attributable to genuine molecular overlap rather than model inadequacy.

HER2-enriched tumours showed the lowest classification performance (Figure 2b and Table 5), which may reflect both the small sample size for this subtype and its inherent transcriptional heterogeneity. The dispersion of misclassified HER2-enriched samples across multiple predicted classes suggests variable gene expression patterns that were not fully captured by the selected feature set. These findings align with previous research highlighting the molecular diversity of HER2-positive disease and the limitations of single-modality transcriptomic classification (Orrantia-Borunda et al., 2022).

SHAP analysis provided gene-level insight into model decision-making, revealing both shared and subtype-specific molecular drivers. Several genes, including TF, ARFIP2, and BBS12, appeared across multiple subtype signatures, suggesting involvement in common regulatory pathways underlying breast cancer progression (Table 6). The identification of TF as a consistently influential feature aligns with emerging evidence linking iron metabolism dysregulation to tumour growth and therapeutic resistance (Alhaddad et al., 2025). Similarly, ARFIP2 and MSN have been independently associated with trastuzumab resistance and poor prognosis, supporting the biological plausibility of the model's explanations (Shi et al., 2024). On the contrary, a subset of genes demonstrated subtype exclusivity, including CDH19 and HSD17B8 for luminal A, SPINK4 for luminal B, NEFL and MSN for HER2-enriched tumours, and MEG3 and P2RX6 for basal-like disease (Table 6). These findings extend established Prediction Analysis of Microarray 50 (PAM50) panels by highlighting additional genes that may contribute to refined subtype discrimination.

The preprocessing pipeline played a critical role in balancing data quality with biological preservation. Moderate filtering improved clustering structure while retaining 99.6% of samples, avoiding over-pruning of biologically valid intermediate cases (Table 1). This hybrid approach addressed limitations of purely computational feature selection noted in previous studies (Acedo-Terrades et al., 2025.

Several limitations may have influenced the findings. Class imbalance between malignant and healthy samples likely contributed to reduced specificity. Subtype imbalance, particularly for HER2-enriched tumours, constrained classification performance and limits generalisability. Ad-

ditionally, reliance on transcriptomic data alone excluded clinical variables such as tumour stage, treatment history, and imaging features that are routinely integrated into diagnostic decision-making. The exclusion of a non-breast cancer control dataset further limits assessment of cross-cancer specificity. Future work should prioritise larger, more balanced multi-cohort datasets and integrate multimodal inputs, including clinical and imaging data, to enhance robustness. Longitudinal gene expression analysis could also enable modelling of disease progression and treatment response.

CONCLUSION

This study demonstrated that recurrent neural networks can accurately and interpretably classify breast cancer using RNA-seq gene expression data. The proposed multi-task bidirectional long short-term memory achieved high diagnostic performance for malignancy detection with perfect sensitivity, alongside reliable molecular subtype classification, with performance patterns reflecting known biological relationships between subtypes. Importantly, the preprocessing and feature selection strategy improved dataset quality while preserving clinically relevant biomarkers, ensuring alignment with established molecular pathways. Explainability analysis further validated the model by identifying biologically meaningful genes consistent with current breast cancer literature. Together, these findings support the research hypothesis that explainable deep learning approaches can leverage transcriptomic data to deliver clinically relevant breast cancer classification while maintaining transparency essential for medical adoption.

ACKNOWLEDGEMENTS

I would like to thank my Science Extension teacher and project supervisor, Ms Thompson, for running the Science Extension course solely for me. Without her initiative, this research opportunity would not have been possible. Her generosity with time and guidance, from identifying gaps in the literature to the final edits, was invaluable. I thank Safaa Al Haj Hussein and Teah Goodhand for their mentorship throughout this project. Their monthly Zoom meetings provided essential feedback on the scientific process and helped ensure a rigorous data preprocessing pipeline. I am grateful for their careful review of my drafts and ongoing support. I also thank Ms Cartwright and Ms English for reviewing my first complete draft and providing constructive feedback that significantly strengthened the quality of my report.

REFERENCES

Acedo-Terrades, A., Perera-Bel, J., & Nonell, L. (2025). The importance of data transformation in RNA-seq preprocessing for bladder cancer subtyping. *BMC Research Notes*, *18*(1). https://doi.org/10.1186/s13104-025-07138-x

Alhaddad, L., Saifo, M., & Alsayed, R. (2025). Special status of iron transfer proteins in the serum of breast cancer patients. *Discover Oncology*, *16*(1). https://doi.org/10.1007/s12672-025-02799-3

Alharbi, F., & Vakanski, A. (2023). Machine learning methods for cancer classification using gene expression data: A review. *Bioengineering*, *10*(2), 173. https://doi.org/10.3390/bioengineering10020173

Australian Institute of Health and Welfare. (2025). *Cancer data in Australia*. https://www.aihw.gov.au/reports/cancer/cancer-data-in-australia/contents/overview

Burcu, B., Ertas, I., Sener, A., Demircioglu, Z. G., Cerekci, E., & Kaya, C. (2023). Retrospective analysis of parameters affecting metastatic breast cancer. *The Medical Bulletin of Sisli Etfal Hospital*, *57*(4), 479–484. https://doi.org/10.14744/SEMB.2023.94803

Dasgupta, S., Dutta, M., Halder, A., Khan, A., Saha, G., & Pal, R. K. (2025). Computational analysis of gene expression data using bidirectional long short-term memory for disease diagnosis. *Innovations in Systems and Software Engineering*, *21*, 93–107. https://doi.org/10.1007/s11334-022-00492-0

Islam, T., Sheakh, Md. A., Tahosin, Mst. S., Hena, Most. H., Akash, S., Bin Jardan, Y. A., FentahunWondmie, G., Nafidi, H.-A., & Bourhia, M. (2024). Predictive modeling for breast cancer classification in the context of Bangladeshi patients by use of machine learning approach with explainable AI. *Scientific Reports*, *14*(1). https://doi.org/10.1038/s41598-024-57740-5

Kim, J.-Y., Lee, Y. S., Yu, J., Park, Y., Lee, S. K., Lee, M., Lee, J. E., Kim, S. W., Nam, S. J., Park, Y. H., Ahn, J. S., Kang, M., & Im, Y.-H. (2021). Deep learning-based prediction model for breast cancer recurrence using adjuvant breast cancer cohort in tertiary cancer center registry. *Frontiers in Oncology*, *11*. https://doi.org/10.3389/fonc.2021.596364

Levy, S. E., & Boone, B. E. (2019). Next-generation sequencing strategies. *Cold Spring Harbor Perspectives in Medicine*, *9*(7), a025791. https://doi.org/10.1101/cshperspect.a025791

Lundberg, S. M., & Lee, S.-I. (2017). *A unified approach to interpreting model predictions*. *30*, 4765–4774. https://proceedings.neurips.cc/paper/2017/hash/8a20a8621978632d76c43dfd28b67767-Abstract.html

Mantione, K. J., Kream, R. M., Kuzelova, H., Ptacek, R., Raboch, J., Samuel, J. M., & Stefano, G. B. (2014). Comparing bioinformatic gene expression profiling methods: Microarray and RNA-seq. *Medical Science Monitor Basic Research*, *20*, 138–142. https://doi.org/10.12659/msmbr.892101

Orrantia-Borunda, E., Anchondo-Nuñez, P., Acuña-Aguilar, L. E., Gómez-Valles, F. O., & Ramírez-Valdespino, C. A. (2022). Subtypes of breast cancer. In *Breast cancer* (pp. 31–42). Exon Publications. https://doi.org/10.36255/exon-publications-breast-cancer-subtypes

Schuster, M., & Paliwal, K. K. (1997). Bidirectional recurrent neural networks. *IEEE Transactions on Signal Processing*, *45*(11), 2673–2681. https://doi.org/10.1109/78.650093

Shi, X., Sheng, Y., Fei, H., Wei, B., Zhang, Z., Xia, X., Mao, C., & Si, X. (2024). Combined transcriptome and proteome analysis reveals MSN and ARFIP2 as biomarkers for trastuzumab resistance of breast cancer. *Breast Cancer Research and Treatment*, *207*(1), 187–201. https://doi.org/10.1007/s10549-024-07355-1

The Cancer Genome Atlas Program. (2018). *The Cancer Genome Atlas Program*. National Cancer Institute. https://www.cancer.gov/ccg/research/genome-sequencing/tcga

Yu, X., Dong, M., Yang, D., Wang, L., Wang, H., & Ma, L. (2023). Deep learning for differentiating benign from malignant tumors on breast-specific gamma image. *Technology and Health Care*, *31*, 61–67. https://doi.org/10.3233/thc-236007

Zhang, Y., Ji, Y., Liu, S., Li, J., Wu, J., Jin, Q., Liu, X., Duan, H., Feng, Z., Liu, Y., Zhang, Y., Lyu, Z., Song, F., Song, F., Yang, L., Liu, H., & Huang, Y. (2025). Global burden of female breast cancer: New estimates in 2022, temporal trend and future projections up to 2050 based on the latest release from GLOBOCAN. *Journal of the National Cancer Center*, *5*(3), 287–296. https://doi.org/10.1016/j.jncc.2025.02.002

YASJ Young Australians Science Journal

Investigation of kinetic energy of .308 projectiles of different masses

Isaac Phillips[1]

[1]Killara High School, Sydney, NSW, Australia

ABSTRACT

Projectile kinetic energy is a useful metric in ballistics that allows for the understanding of the magnitude of chemical potential energy that is transferred to projectiles in firearms. The purpose of this report is to investigate the effect that .308 projectile mass has on the kinetic energy of projectiles at muzzle exit of a .308 target rifle. Velocity was measured with the use of a radar chronograph, which was used to calculate the kinetic energy of the projectiles at that point in time. It was found that although velocity decreased as mass increased, kinetic energy increased as mass increased. The kinetic energy increased from approximately 3275J at 155 grains to 3962J at 220 grains. This was explained by the greater opportunity for work to be done on projectiles of greater mass due to slower volume expansion behind the projectile. This acts as a demonstration of Newton's Second Law and variables that influence projectile behaviour in ballistics such as pressure evolution over time.

Young Australians Science Journal
Volume 1, Issue 1, 2026, pp. 19–25
https://doi.org/10.67642/ar34df81

Keywords: internal ballistics; projectile mass; muzzle velocity; kinetic energy; radar chronograph; classical mechanics

Student authors: Isaac Phillips, Year 12

Address correspondence to authors@yasj.org.au

Type: Research Article
Open access: Yes

Licence: This work is licensed under a Creative Commons Attribution-NonCommercial 4.0 International License (CC BY-NC 4.0).

DOI: 10.67642/ar34df81

YASJ Editors' Note: This study presents a clear investigation of how projectile mass relates to muzzle velocity and kinetic energy under controlled loading conditions. The use of chronograph measurements and statistical analysis gives the work a strong experimental structure. Readers should note that the findings are specific to one rifle and loading configuration, and that the 220-grain group contains four valid measurements rather than five. The proposed explanation involving pressure evolution within the barrel is plausible, but was inferred rather than measured directly.

LITERATURE REVIEW

The behaviour of projectiles when fired by a firearm is dictated by internal ballistic processes, in which chemical energy from propellent (smokeless powder) is converted into kinetic energy of the projectile. Understanding the factors that affect the muzzle velocity and energy is central to applications in ballistics. These processes occur within the barrel and involve the generation of dramatically expanding gases due to propellent combustion which results in the acceleration of the projectile. The evolution of pressure within the barrel is highly dynamic, increasing dramatically initially after ignition then decreasing as the volume behind the projectile expands, as explained by Ongaro et al. (2024).

Muzzle velocity, defined as the velocity of a projectile the instant it exits the barrel of a firearm, is a crucial parameter in determining projectile behaviour such as range, trajectory and impact characteristics. It is governed by a range of variables such as projectile, propellent and barrel characteristics. As such, it is a significant measurable indicator on the efficiency of the energy transfer occurring within the firearm, as noted by Rogers et al. (2024).

A particularly significant parameter affecting muzzle velocity is projectile mass. As described by Newton's Second Law, $F = ma$, an increase in mass results in a decrease in acceleration for a given force, and as such the resulting velocity of such a mass will be decreased. However, the motion of the projectile also affects the pressure

evolution within the barrel. A decrease in acceleration slows the extent to which the volume behind the projectile expands, allowing higher pressures to be sustained over a greater length of the barrel. The kinetic energy of a projectile is given by $KE = \frac{1}{2}mv^2$, displaying how kinetic energy depends linearly on mass but quadratically on velocity. This indicates competing behaviour, as velocity tends to decrease with increasing mass due to lower acceleration, lowering kinetic energy, but increasing mass increases kinetic energy through the mass component, thus the result will represent some balance of these effects, accounting for the work done on the projectile while inside the barrel. The work-energy theorem states that $W = \int F\,dx$, indicating that a higher pressure sustained over a longer length of the barrel can result in an increase in the kinetic energy at muzzle exit. This is noted in detail in Ongaro et al. (2024).

The use of a radar chronograph in experimental ballistics studies is a highly accurate and well supported as seen in Silva-Rivera et al. (2021). It functions by measuring the time taken for a projectile to pass between two sensors on the device, thus making them a reliable and efficient tool for the measurement of muzzle velocity.

Experimental studies have demonstrated a strong correlation between theoretical physical models and experimental measurements, supporting the validity of studies on highly impactful parameters such as kinetic energy of projectiles, as noted by Kagankiewicz and Magier (2024). Importantly, many studies are investigating the impact of firearm, projectile and propellant characteristics, especially in the realm of optimising energy transfer and the prediction of projectile trajectories, as seen in Xiao and Zhang (2026), reinforcing the relevance of research into energy transfer in firearms.

While many studies investigate the effects of propellant charge or barrel characteristics, few have specifically isolated the effect of projectile mass on the muzzle velocity of firearms and thus the transfer of kinetic energy to the projectile. Thus, this study seeks to investigate the relationship between projectile mass and the net transfer of kinetic energy, providing insight into factors such as pressure evolution, acceleration, mass, muzzle velocity and kinetic energy.

SCIENTIFIC RESEARCH QUESTION

Does the mass of a .308 calibre projectile affect its kinetic energy at muzzle exit of a .308 calibre Custom Barnard P Action rifle with a 30 inch Krieger barrel?

SCIENTIFIC HYPOTHESIS

The .308 projectiles of greater mass will have greater kinetic energy at muzzle exit of a .308 calibre Custom Barnard P Action rifle with a 30 inch Krieger barrel.

METHODOLOGY

25 total .308 cartridges were loaded with 40 grains of ADI AR2208 smokeless rifle powder (gunpowder) and 220 grain Berger Target, 200 grain Berger Hybrid, 185 grain Berger Juggernaut Target, 168 grain Berger Hybrid Target HPBT and 155 grain Sierra Match King HPBT projectiles (all of which were match-grade hollow point boat tail design (HPBT) for greatest consistency in internal ballistic performance), 5 cartridges for each projectile mass to reduce the effect of variance within each group (see Supplementary Methods S1). The actual mass of the projectiles was verified using an Ohaus Precision Standard electronic balance. At St Marys Indoor Shooting Centre, a .308 Custom Barnard P Action rifle with a 30 inch Krieger Barrel was set up on a shooting table using an adjustable rest to maintain stability and a consistent firing position. A Garmin Xero C1 Pro chronograph was positioned behind the end of the barrel, which records instantaneous velocity at the moment the projectile exits the muzzle using radar. In a seated shooting position, the shooter fired a 220 grain projectile cartridge and the chronograph velocity reading was recorded in feet per second while connected to an iPhone 8 Plus via Bluetooth on ShotView™ mobile application, which was used exclusively to record the velocities from the chronograph, which are inputted automatically from the chronograph to the app after each measurement. This was repeated for the remaining 4 220 grain projectile cartridges, waiting 1:30 minutes between each shot to reduce variance due to barrel temperature. This process was repeated for the 200, 185, 168 and 155 grain projectiles. The experiment was conducted under a documented risk assessment and in accordance with the applicable shooting-range procedures. The velocity of each projectile was documented in Microsoft Ex-

cel and utilised to calculate the kinetic energy of each projectile mass at muzzle exit using relevant equations.

RESULTS

The muzzle velocity of projectiles was measured with a degree of uncertainty ±0.05ft/s and were transferred from ShotView™ and documented in a table in Microsoft Excel with unit conversions to metric (ft/s to m/s) (see Supplementary Table S1). An error occurred in the chronograph for the 220gr projectile where one shot was not recorded.

This was then transferred to a table with only metric values for velocity (m/s) (Table 1).

Table 1. Relationship between muzzle velocity (m/s) and projectile mass (gr, kg)

Mass (gr)	Mass (kg)	Velocity (m/s)					
		Trial 1	Trial 2	Trial 3	Trial 4	Trial 5	Average
220	0.01425576	746.9124	750.3871	742.2794	742.4928		745.5179
200	0.01295978	773.4605	774.2225	767.6388	775.6855	768.6751	771.9365
185	0.01198780	767.1816	780.2880	779.7698	772.8509	780.1966	776.0574
168	0.01088622	787.5727	804.0014	792.0533	801.5021	799.0942	796.8447
155	0.01004383	815.3400	803.3004	807.6286	806.7446	804.7330	807.5493

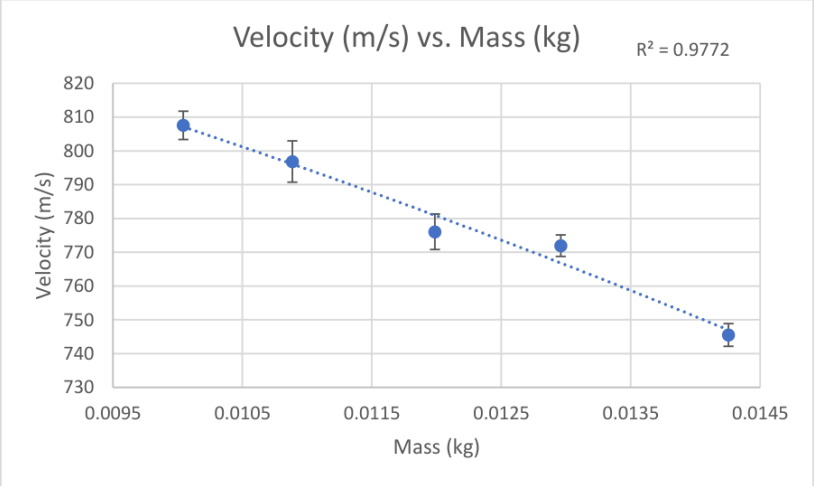


Figure 1. Relationship between muzzle velocity (m/s) and projectile mass (kg). Group sample sizes were $n = 4$ for 220 gr and $n = 5$ for all other projectile masses

ANOVA was used with an alpha value of 0.05 to determine whether there was a statistically significant difference between the means of the velocity of each group (see Supplementary Table S2).

The velocities collected from Table 1 were used to calculate kinetic energy by the formula $KE = \frac{1}{2}mv^2$, where m is the projectile mass in kg and v is the projectile velocity in m/s (Table 2).

Table 2. Relationship between projectile kinetic energy at muzzle exit (J) and projectile mass (gr, kg)

Mass (gr)	Mass (kg)	Kinetic energy (J)					
		Trial 1	Trial 2	Trial 3	Trial 4	Trial 5	Average
220	0.01425576	3976.488	4013.573	3927.311	3929.569		3961.735
200	0.01295978	3876.537	3884.179	3818.401	3898.873	3828.718	3861.342
185	0.01198780	3527.815	3649.382	3644.536	3580.147	3648.526	3610.081
168	0.01088622	3376.201	3518.525	3414.725	3496.683	3475.705	3456.368
155	0.01004383	3338.466	3240.600	3275.614	3268.448	3252.168	3275.059

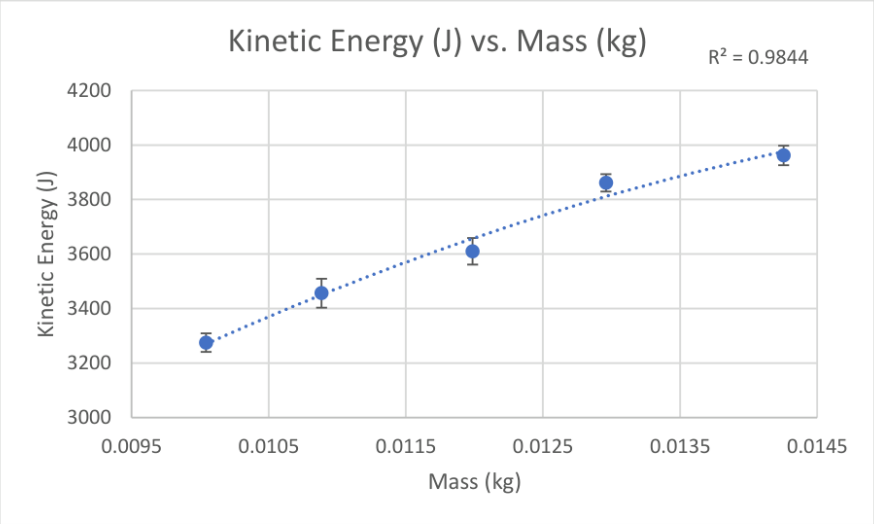


Figure 2. Relationship between kinetic energy of projectile at muzzle exit (J) and projectile mass (kg). Group sample sizes were $n = 4$ for 220 gr and $n = 5$ for all other projectile masses

ANOVA was used with an alpha value of 0.05 to determine whether there was a statistically significant difference between the means of the kinetic energy of each group (see Supplementary Table S3). Since kinetic energy is proportional to the square of velocity, propagated uncertainty can be evaluated as $\Delta KE = KE \cdot 2\frac{\Delta v}{v}$, where $\Delta v = \pm 0.015\ \mathrm{m\,s^{-1}}$ based on chronograph precision.

These values are naturally included in the standard deviation shown in the error bars and contribute a small portion of the total error.

For purposes of discussion, average acceleration of projectile from rest to recorded velocity and the time the projectile takes to travel the length of the barrel were calculated using the following equations:

$a = \frac{v^2-u^2}{2s}$, where a is average acceleration, v is final velocity, u is initial velocity and s is displacement (length of the barrel the projectile travels) (see Supplementary Tables S4 and S5).

$t = \frac{v-u}{a}$, where t is the time the projectile takes to travel the length of the barrel, v is final velocity, u is initial velocity and a is average acceleration (Table 3).

ANOVA statistical tests were performed on both data sets with an alpha value of 0.05 (see Supplementary Tables S5 and S6).

Table 3. Relationship between projectile time in barrel (s) and projectile mass (gr, kg)

Mass (gr)	Mass (kg)	Time in barrel (s)					
		Trial 1	Trial 2	Trial 3	Trial 4	Trial 5	Average
220	0.01425576	0.001870367	0.001861706	0.001882041	0.001881500		0.001873903
200	0.01295978	0.001806169	0.001804391	0.001819866	0.001800988	0.001817413	0.001809765
185	0.01198780	0.001820951	0.001790365	0.001791554	0.001807593	0.001790574	0.001800207
168	0.01088622	0.001773804	0.001737559	0.001763770	0.001742977	0.001748230	0.001753268
155	0.01004383	0.001713396	0.001739075	0.001729756	0.001731651	0.001735980	0.001729970

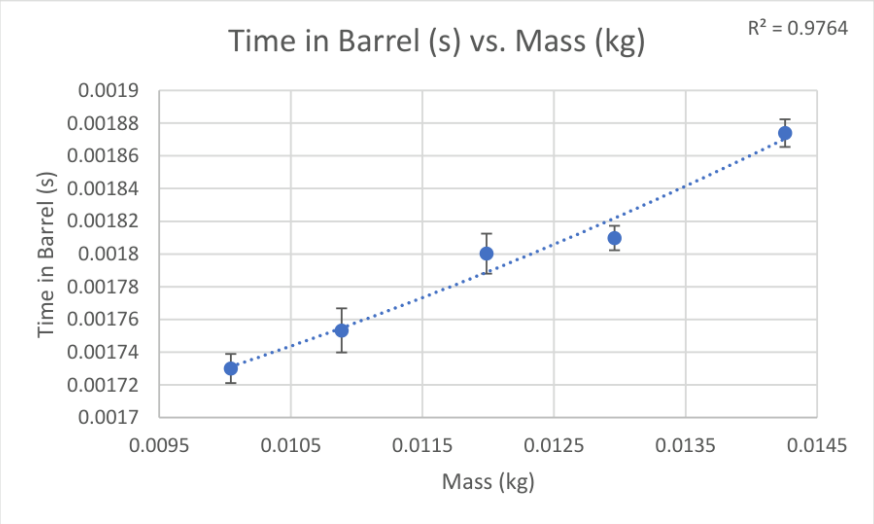


Figure 3. Relationship between projectile time in barrel (s) and projectile mass (kg). Group sample sizes were $n = 4$ for 220 gr and $n = 5$ for all other projectile masses

DISCUSSION

All data gathered was tested using ANOVA with an alpha value of 0.05. The F-critical for all data sets was 2.895107. No injuries occurred during the experiment.

The projectile muzzle velocity as seen in Table 1 and Figure 1 was observed to decrease as mass increases. This is plausible as it adheres to Newton's Second Law, as objects of larger mass experience less acceleration under application of a constant force. This remained true despite factors such as friction on the rifling and the projectile travels through the barrel, which would theoretically have a greater deceleration effect on lighter projectiles. The trend was not linear, as seen in Figure 1, a polynomial trendline with a slight negative concavity fit the data with the greatest R^2 value of 0.9772, indicating that the magnitude of the rate of velocity decrease increases with mass. ANOVA displayed an F-value of 96.74092 and a pvalue of 2.343792×10^{-12} (F-value $>$ F-critical, p-value < 0.05), indicating that there was a statistically significant difference between the means within this data set (the results are unlikely (less than 5% probability) to have been caused by random chance).

Using the velocities calculated from Table 1, the kinetic energy of the projectiles at the instant that the muzzle velocity was calculated (the moment the projectile left the muzzle) using the equation $KE = \frac{1}{2}mv^2$. Theoretically, velocity would have a greater effect on kinetic energy than mass would, due to kinetic energy being directly proportional to the square of velocity, while being directly proportional to mass. Experimentally, as seen in Table 2 and Figure 2, the kinetic energy of the projectile increased with mass, despite lighter projectiles possessing greater velocities. ANOVA displayed an F-value of 168.7801 and a p-value of 1.465494×10^{-14} (F-value $>$ F-critical, p-value < 0.05), indicating that there was a statistically significant difference between the means within this data set. This trend can be explained by the nature of the energy transfer between the potential energy in the gunpowder charge, that being the work done on the projectile being proportional to the force on the projectile integrated over the length of the barrel.

Although not directly related to the work done on the projectile, the time the projectile spends in the barrel affects the rate at which the volume expands behind the projectile, thus affecting the magnitude of pressure generated by the propellant combustion over time and thus being a relevant relationship to examine with respect to projectile mass. In order to calculate the time the projectile spends in the barrel, first the average acceleration of the projectile must be calculated. The barrel length was measured to be 30in, and the cartridge protrudes into the barrel 2.5in when chambered, so a total displacement of 27.5in was converted to metric (0.6985 m) and used in calculations. Using the equation $a = \frac{v^2-u^2}{2s}$, the average acceler-

ation of each data point was calculated (as shown in Supplementary Table S4) and analysed using ANOVA to display an F-value of 94.82958 and a p-value of 2.805423×10^{-12} (F-value > F-critical, pvalue < 0.05), reinforcing a statistically significant difference between the means within the data set.

The average acceleration of each data point was then used to calculate the total time the projectile spent travelling from rest to muzzle exit when fired. This was achieved using the equation $t = \frac{v-u}{a}$ (as seen in Table 3) and was also analysed using ANOVA to display an F-value of 100.4061 and a p-value of 1.675771×10^{-12} (F-value > F-critical, p-value < 0.05), reinforcing a statistically significant difference between the means within the data set. Table 3 and Figure 3 depict time spent in firearm barrel as increasing with mass. The trendline is polynomial with a slight positive concavity, indicating that the rate of increase in time increases with mass. This experimentally and mathematically confirms Newton's Second Law.

Since time spent in firearm barrel increases with projectile mass, and kinetic energy also increases with mass, it can be inferred that the greater kinetic energy in the heavier projectiles is explained by a greater opportunity for the combustion of the propellant to do work on the projectile. When a round is fired, the chemical potential energy stored in the gunpowder is released in a combustion reaction which results in the formation of rapidly expanding gases. The interaction between the rapidly expanding gases and the projectile transfers the potential energy released in the combustion reaction to kinetic energy in the projectile. In all practical applications, some energy is lost in the system in forms such as bearing surface friction, air resistance, heat and sound, therefore not all chemical potential energy is transferred to kinetic energy in the projectile. Thus, the difference in kinetic energy in heavier and lighter projectiles can be determined to be a result of the heavier projectiles travelling at slower velocities, therefore increasing the duration of time spent in the barrel, which results in a lower volume expansion rate behind the projectile, causing higher pressures to be sustained for a longer period of time and thus for a longer portion of the barrel's length. According to the work-energy theorem, $W = \int F\,dx$, a greater force due to pressure over a particular length will result in a greater work done on the projectile, thus explaining the increasing kinetic energy with increasing projectile mass.

It should be noted that this experiment contains limitations. The Ohaus Precision Standard electronic balance has a degree of uncertainty of ±0.01gr (0.000648g), which is almost negligible in this experiment. There was also found to be a deviation of up to 0.22gr (0.0143g) in the weighed projectiles when compared with their manufacturer stated masses. Variables such as neck tension, brass quality, brass wear, gunpowder moisture content, projectile uniformity, primer charge uniformity, recoil resistance, bullet centricity also have effects on the velocity of the projectile, which could explain the variance within groups. Further limitations of this research are extrapolation to other factors in ballistics such as ballistic coefficient and the behaviour of projectiles in long range flight, which have not been considered in this investigation.

CONCLUSION

The aim of this investigation was to determine how .308 projectile mass affected the kinetic energy of projectiles at muzzle exit of a .308 target rifle. The data was consistent with the expected relationship of increased kinetic energy with increased mass, supported by statistically significant results despite limitations such as measurement uncertainty and shot variance. Thus, the hypothesis was supported. These findings reinforce principles of classical physics and its application to ballistics in practice.

SUPPLEMENTARY MATERIAL

Supplementary material accompanying this article contains the raw data and unit conversions, derived acceleration calculations, ANOVA outputs, an additional derived-data figure and detailed supplementary methods.

The supplementary PDF is available with the online article at https://doi.org/10.67642/ar34df81.

REFERENCES

Kagankiewicz, F., & Magier, M. (2024). Experimental verification of the internal ballistics numerical simulations of classical weapons in Lagrangian coordinates. *Continuum Mechanics and Thermodynamics*, *36*(5), 1323–1337. https://doi.org/10.1007/s00161-023-01263-3

Ongaro, F., Robbe, C., Papy, A., Stirbu, B., & Chabotier, A. (2024). Modelling of internal ballistics of gun systems: A review. *Defence Technology*, *41*, 35–58. https://doi.org/10.1016/j.dt.2024.05.004

Rogers, J. A., Bass, N. T., Wiest, M. L., Wantz, Z., Wilkerson, J. W., & Lacy, T. E. Jr. (2024). The pursuit of hypervelocities: A review of two-stage light gas gun aeroballistic ranges. *International Journal of Impact Engineering*, *185*, 104861. https://doi.org/10.1016/j.ijimpeng.2023.104861

Silva-Rivera, U. S., Zúñiga-Avilés, L. A., Vilchis-González, A. H., Tamayo-Meza, P. A., & Wong-Angel, W. D. (2021). Internal ballistics of polygonal and grooved barrels: A comparative study. *Science Progress*, *104*(2). https://doi.org/10.1177/00368504211016954

Xiao, Y., & Zhang, X. (2026). A novel structure to continuously control muzzle velocity of a gun based on two-phase reactive flow and energy exchange characteristics. *International Communications in Heat and Mass Transfer*, *175*, 111070. https://doi.org/10.1016/j.icheatmasstransfer.2026.111070

YASJ Young Australians Science Journal

Box modelling the transfer of sulfur on Mars using Earth as a geochemical analogue

Cathy Zhang[1], Penelope King[2]

[1]James Ruse Agricultural High School, Sydney, New South Wales, Australia
[2]Australian National University, Canberra, Australian Capital Territory, Australia

ABSTRACT

Volcanism was once the primary source of sulfur transport on Mars, and its present-day surface preserves a geological record of these mineralogical processes. Sulfur plays a key part in the eruption process, forming sulfides, and less commonly sulfates in the magma chamber, and being expelled as sulfur dioxide-rich gas. However, there is a mismatch between the location of existing volcanic provinces and detections of high sulfur abundances measured through satellite instruments such as the Compact Reconnaissance Imaging Spectrometer for Mars (CRISM) and the Gamma Ray Spectrometer (GRS). Despite similarly hosting a basaltic surface, the sulfur content in Martian meteorites (408–2700 ppm) and by Martian dust measured by rovers (2 wt% S) exceeds Earth's basalts by almost an order of magnitude. This study attempts to account for the observed abundance of sulfur through applying comparative planetology using Earth's volcanoes, including both eruptive and quiescent degassing rates and solid leachate particles. The study successfully provided order-of-magnitude estimates of the mass of sulfur produced in volcanism over the Noachian-Hesperian periods of >3.7 to 3.1 Ga and it provided values similar to previous studies. However, it was not possible to confirm mass balance due to large uncertainties in the mass of sulfur in the sedimentary reservoir.

Young Australians Science Journal
Volume 1, Issue 1, 2026, pp. 26–36
https://doi.org/10.67642/97wtbw66

Keywords: Mars; sulfur cycle; volcanism; volcanic degassing; comparative planetology; box modelling; geochemistry

Student authors: Cathy Zhang, Year 11

Address correspondence to authors@yasj.org.au

Type: Research Article
Open access: Yes

Licence: This work is licensed under a Creative Commons Attribution-NonCommercial 4.0 International License (CC BY-NC 4.0).

DOI: 10.67642/97wtbw66

YASJ Editors' Note: This study applies comparative planetology and box modelling to investigate the Martian sulfur cycle at a planetary scale. The use of terrestrial volcanic data, including eruptive and quiescent degassing, provides a creative basis for estimating sulfur fluxes over geological time. Readers should note that the model relies on assumptions about eruption duration, volcanic surface area and sulfur reservoirs, while the unknown depth of the sedimentary reservoir prevents a complete mass balance. Within these limitations, the study provides a useful framework for further investigation.

INTRODUCTION

Understanding the sulfur budget on Mars is critical for reconstructing its volcanic history and early climate evolution. Unlike Earth, Mars has no current active volcanism or plate tectonics, hence hosting many rocks older than 3.6 Ga (Tanaka et al., 2014) that preserve a historical record for its mineralogical processes and planet formation (Ehlmann & Edwards, 2014). Mars' geologic history is divided into the Noachian (>3.7 Ga), Hesperian (3.7–3.1 Ga), and Amazonian (<3.1 Ga) periods (Figure 1), and has been continuously constructed through insights from orbital infrared spectroscopy and in situ chemical measurements from rovers and landers. Its volcanic rock pri-

marily formed during the planet's early formation as a magma ocean 4.48 Ga ago (Moser et al., 2019), and during the Noachian-Hesperian periods (Ehlmann & Edwards, 2014). Like the other terrestrial inner planets, Mars has a dominantly basaltic surface, however the Martian sulfur content exceeds Earth's basalts by almost an order of magnitude (Ojha et al., 2019). Atmospheric SO_2 derived from volcanic activity is highly likely to have influenced the early climate of Mars, providing a greenhouse effect that may have maintained warm, wet conditions in the early Noachian period necessary to account for the observed clay deposits. The widespread availability of sulfur on Mars could have provided an abundant source for energy and nutrients to fuel sulfur-metabolizing microbes. Sulfates also have a high potential to preserve biomarkers and palaeoenvironmental conditions since they can rapidly precipitate from a brine. Thus, understanding the source and transport processes for the abundance of sulfur on Mars can help characterise its past habitability, potential for life, and climate change that eventuated in its current dry, oxidising environment.

The excess sulfur on Mars suggests that volcanism was the most important geologic process in enriching the Martian bedrock (Szynkiewicz et al., 2022). This is because sulfur is involved in every part of an eruption process; it forms sulfides and sulfates in the magma chamber or becomes supersaturated into sulfur-bearing species that alter the crust in a fluid phase, becoming an SO_2-rich gas that is expelled at low pressure (Casas et al., 2026).

After being released into the atmosphere, S-bearing volcanic gases undergo oxidation-reduction reactions and solid disproportionation to become different sulfur species deposited in S-bearing solids. At shallow depths of the near-surface crust within volcanoes, sulfur may become supersaturated in the melt, forming bubbles of different S-species that either escape as gas or build up and release explosively at a volcanic plume (Casas et al., 2026). When eruptions occur, solid volcanic fragments can be transported and deposited, potentially including sulfur-bearing species. Whilst the ferric oxides that colour Mars' surface red indicate a currently dry, oxidising environment (Bibring et al., 2005), sediment analysis reveals clays older than the mid-Hesperian. These may indicate a previously wet environment (Ehlmann & Edwards, 2014) that allowed sulfuric acid to form and transport S-species. This may have formed some very early sulfates on Mars' surface, suggesting other sulfates formed in a continually drying environment.

Mars' lack of present volcanic activity prevents direct observation, hence geochemical information is derived from rover and satellite missions characterising samples of the sedimentary rock currently on the Martian surface.

As shown in Figure 2, surface materials containing typical SO_3 abundances have concentrations of ~4-7 wt% (1.6-2.8 wt% S) reaching 40 wt% (16 wt% S) for sulfate-rich veins. These sulfur-rich areas mapped by GRS do not appear to correspond with CRISM sulfate-bearing rocks, nor with the volcanic provinces, nor with any particular unit of volcanic rock, further raising questions regarding the transportation and depositional processes that result in high S concentrations and distributions. The only currently observed process for transportation of sedimentary sulfur is aeolian due to the dry Martian environment, however there is evidence of previous fluvial and potentially glacial processes promoting sulfur dissolution. However, these processes only serve to redistribute existing sulfur on the Martian surface, and do not affect how they are sourced, and thus do not explain their abundance. This suggests that key sulfur sources or transport mechanisms remain unidentified.

There have been several attempts to quantify the output and concentration of sulfur on Martian surfaces. Applying the law of uniformitarianism, scientists have used analogue volcanic systems from Earth to better understand Mars' mineralogy. For example, Ende and Szynkiewicz (2021) used chosen terrestrial O_2-depleted acidic hydrothermal vents as a geochemical analogue for the hydrothermal S-rich deposits in Gusev crater on Mars, in order to investigate potential oxidation mechanisms of volcanic S. Whereas Earth's climate and surface chemistry are mostly dependent on the water and carbon cycle, Mars likely hosted a sulfur cycle (Franz & King, 2026; Hynek et al., 2019; Ojha et al., 2019). Gaillard et al. (2013) have attempted to box model this sulfur cycle, concluding from experimental results, thermodynamic models, and the direct measurements of Martian soils that a variety of sulfur reservoirs and sulfur cycling processes are involved.

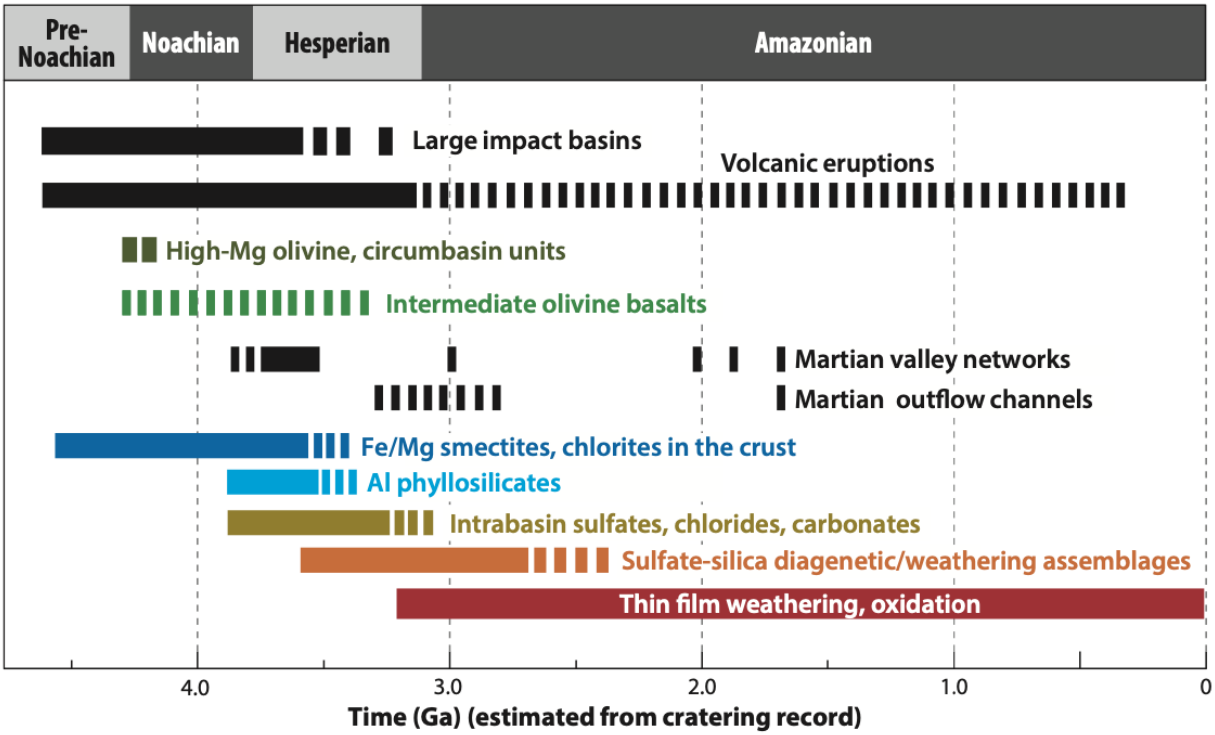


Figure 1. Mars' geologic time scale from Ehlmann and Edwards (2014)

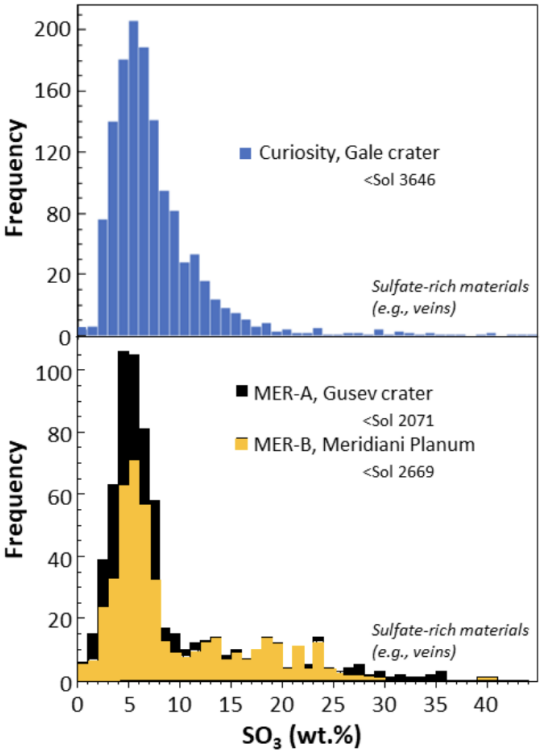


Figure 2. Histograms showing sulfur content as SO_3 wt% from the Alpha-particle X-ray Spectrometer (APXS) using bins of 1 wt%. The trend identifies primarily 5 wt% of SO_3 as the concentration of sulfur content currently observed in three landing sites on Mars, with higher concentrations >30 wt% observed in sulfate-rich veins (Franz and King, 2026)

Figure 3 represents their proposed early Martian sulfur cycle, before major reduction in magmatic rates some time greater than 3 Gyr ago, and outlines the major potential reservoirs and transport processes to be considered for the distribution of sulfur. However, these estimations lack quantitative values, especially fluxes that consider time. This existing model only serves as a visualisation of the many potential interactions of sulfur reservoirs.

Other studies, such as Hynek et al. (2019) and Ojha et al. (2019) have attempted to balance a box model for local, well-studied sites on Mars, specifically Meridiani Planum and the Medusae Fossae Formation (MFF) respectively. Hynek et al. (2019) used mass balancing, by providing relevant volumes and identifying the limitations of individually proposed scenarios of groundwater upwelling, volcanic airfall, atmospheric source and fluvial input. However, these models do not account for the likely possibility of these input scenarios occurring simultaneously and affecting one another. They identified the need for a better constraint of the primary basaltic sediment and sulfate sources in order to justify any further calculations. Ojha et al. (2019) concluded the mass of the S emitted from the MFF-forming event(s) was up to "8 orders of magnitude higher than the mass of S emitted from the largest Quaternary vol-

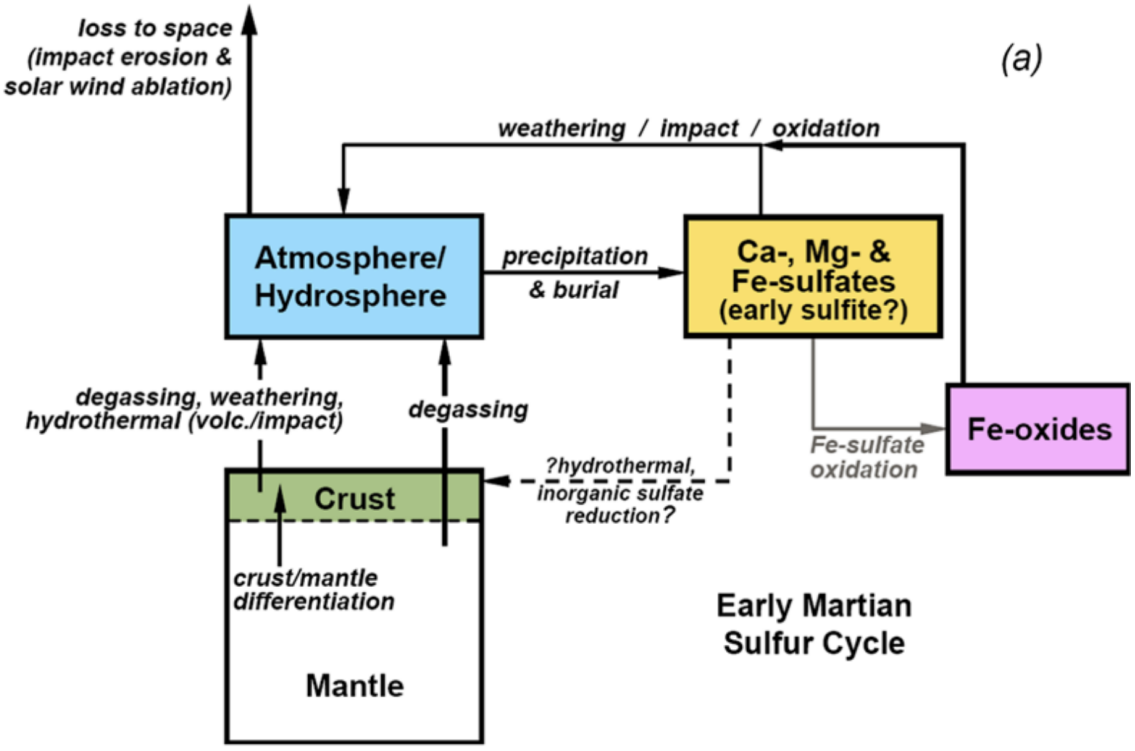


Figure 3. A simplified box model of the early Martian sulfur cycle, with no quantitative values, identifying the primary fluxes between reservoirs (from Gaillard et al., 2013)

canic eruption on Earth", further emphasizing the need to constrain the source of sulfur that would create the observed abundance. Neither of these studies included the effects of time, which significantly limits their reliability as the timescale over which the events they describe occurred would significantly affect the magnitude of final emitted sulfur mass.

All three studies described above have produced models which have remained largely incomplete as their proposed mechanisms for sulfate deposition and formation (e.g. groundwater upwelling and fluvial input) do not explain the abundance of sulfur in the bedrock. Eruptions in Kilauea, an analogue basaltic shield volcano in Hawaii, show that there are other sources of sulfur not considered by these authors. Sulfates can also form during quiescent degassing and also in the eruption plume, as seen at Kilauea (Franz & King, 2026) and these may be sampled in volcanic ash-leachates (the adsorption of volatiles onto ash) that have avoided contact with water, which would actively dissolve the sulfates into groundwater (Casas et al., 2026). Quiescent degassing is the release of gas during a volcano's life outside of sole-eruption events, and can take place over months to decades. From an estimate of ~2.8×10^{12} g of SO_2 per year from Earth's eruption data from 1978-2014, ~43% is contributed by quiescent degassing (Carn et al., 2016) demonstrating that it makes significant contributions to the total amount of sulfur transported into the atmosphere reservoir.

This study attempts to quantitatively constrain the sulfur cycle on Mars by applying comparative planetology using data from Earth's volcanoes, including both eruptive and quiescent degassing rates and incorporating the effects of eruption duration through flux rates. Box modelling was used to assess whether incorporating quiescent degassing alongside eruptive degassing can better account for the sulfur output by volcanic reservoirs on Mars during the Noachian-Hesperian periods. By doing so, I provide useful estimates that can be used in future research to help scientists further characterise the primary chemical cycle on Mars and its broader effect on Martian climate change. Additionally, this comparative planetology methodology could be developed and eventually applied to other rocky planets with basaltic magma systems to understand their planetary evolution.

METHODOLOGY

Earth's SO_2 gas output flux rate

The dataset was chosen from four review papers which collated multidecadal measurements of ter-

restrial volcanic eruptive and quiescent degassing (i.e. Carn et al., 2003; Carn et al., 2016; Carn et al., 2017; Shinohara, 2008). The volcanoes chosen had to satisfy the following list of parameters in order to best replicate Martian volcanic conditions:

- Primarily basaltic (Ehlmann & Edwards, 2014)
- Must originate from intraplate volcanism or intercontinental rift zones, as Mars has no plate tectonics
- Measurements avoid contact with water to ensure the sulfur has not been dissolved

The last condition removed mid-ocean ridge formations from consideration; despite contributing a large amount of basalt production on Earth, the presence of seawater would render measurements inaccurate for comparison with Mars. This decreased the sample size to 16 volcanoes, a list of which can be found in Supplementary Material (Appendix V).

These mass values were collated and converted to kilotonnes (kT). Their respective flux values (mass/time) were determined through dividing this mass with the respective period of eruption the sulfur was released over, sourced from the Smithsonian Natural History Global Volcanism Program. These volcanoes were further classified by magma type (including alkali-basalts and basalt-rhyolitic), tectonic environment and type of eruption (active or quiescent). In order to be able to apply these fluxes directly to Martian volcanic sources for which only the surface area is known, the approximate surface area for each terrestrial volcano was found through satellite imagery. To do this, a spherical map projection was used and simplified into 2D of a circle's area, with variable radius. The centre of the circle was placed in the centre of the volcanic vent, whilst the radius was adjusted to extend to where volcano elevation reaches zero.

Thus, each flux was calculated using the following formula:

$$\text{Flux}_{\text{output}} = \frac{V}{t \cdot SA}$$

where (V) = volume of extruded S, (t) = eruption period, SA = surface area of Earth volcano.

Volcanoes at rift zone boundaries and of slightly altered basaltic compositions were also included to identify any different trends in flux. Due to the large order of magnitude difference in range between active volcanic eruptions output flux and quiescent degassing rates, a logarithmic scale was applied to the data. Flux was then grouped through the Past4 program, creating a histogram frequency distribution graph. The bin size varied with integer intervals. When observing for a peak, there was no difference in the highest value between the histograms of 5, 6 and 7 bins for the same range, and hence the primary flux value was derived by observing the highest frequency value.

Volcanic reservoir sizes

To quantify the Martian volcanic reservoir, a total surface area was calculated to apply the terrestrial SO_2 flux to and this was applied to predict the mass of sulfur released during the Noachian-Hesperian periods. A mass representing the current size of the reservoir was also calculated using known sulfur concentrations from Martian meteorites representing the Martian source region for volcanic rocks.

The total surface area for volcanic Martian reservoirs was determined through using the United States Geological Survey (USGS) Geologic Map of Mars (Tanaka et al., 2014). The same map projection process applied for Earth's volcanoes in the Earth's SO_2 Gas Output Flux Rate section was employed for each volcanic unit, using a different shape maintained by approximating the projection of the map as two circles attached to the central rectangle (Figure 9). This shape was then resized to contain all individual Noachian to Hesperian volcanic units within it, matching the scale to calculate the surface area of the volcanics (Figure 10).

The sum of the surface area of these shapes was multiplied with the Earth SO_2 sulfur output flux to create an equivalent output flux for Martian volcanism.

In addition, the amount of sulfur in the mantle reservoir was estimated using the volatile content of undegassed Martian meteorites such as shergottites and nakhlites with S contents of <0.27 wt% and <0.2865 wt% respectively (Franz & King, 2026). The maximum values of the indicated range were taken as they represent the least degassed S contents of the meteorite that was measured. The assumption was made that the highest sulfur contents of the meteorites can be used as an estimate for mantle volatile content, as there would

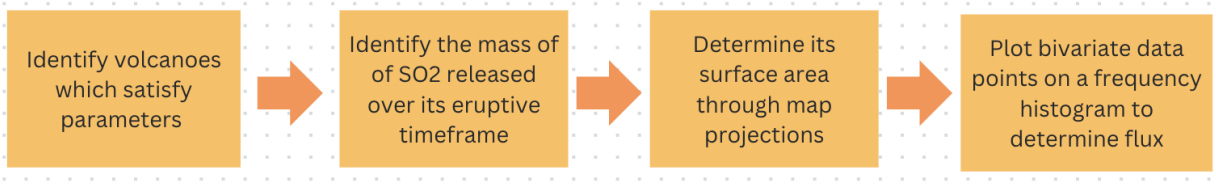


Figure 4. Overview of methodology to calculate the Earth SO_2 gas output flux

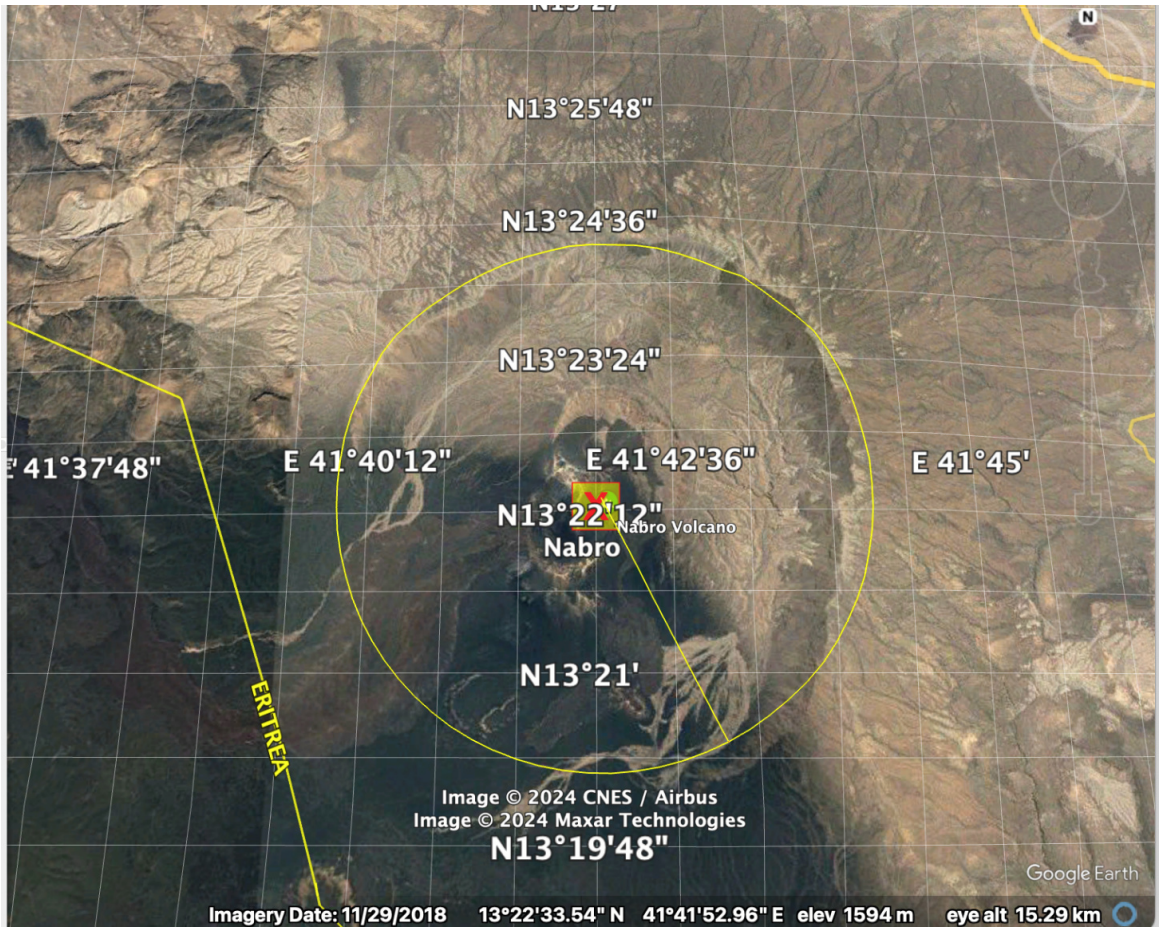


Figure 5. Google Earth circle measurement tool used to create surface area estimates. Radius extends to the edge of the volcano's elevation

be no other new sources of S in the meteorite. This assumes that the mantle has an approximate uniform distribution of sulfur near the crust. Although likely not precise, this method provides a range for source regions (i.e. the magma chamber) and surface rocks (Jakosky & Treiman, 2023). The size of the volcanic reservoir in kt of sulfur was also calculated through estimates of the total mass of extruded Martian volcanic materials

with an assumed constant density of 3.3 g cm^{-3} from Craddock & Greeley (2009). Only the values from the Noachian-Hesperian periods were considered, hence creating an estimate for the size of the reservoirs through the chosen time frame.

Sedimentary reservoir sizes

The sedimentary reservoir surface area was calculated through further map projections over a Mercator projection of the USGS Geological Map for Mars (Franz & King, 2026).

Using a similar approach to calculating the volcanic reservoir sizes, shapes of the CRISM sulfate-bearing rocks were outlined in rectangles and circles in Microsoft PowerPoint, with the surface area calculated. The changing scale of a Mercator projection was accommodated for through identifying the different scales at different latitudes throughout the test. However, the average depth and thus volume is indeterminable with the limited measurements on Mars, and the dramatic differences in elevation between the Northern lowlands and

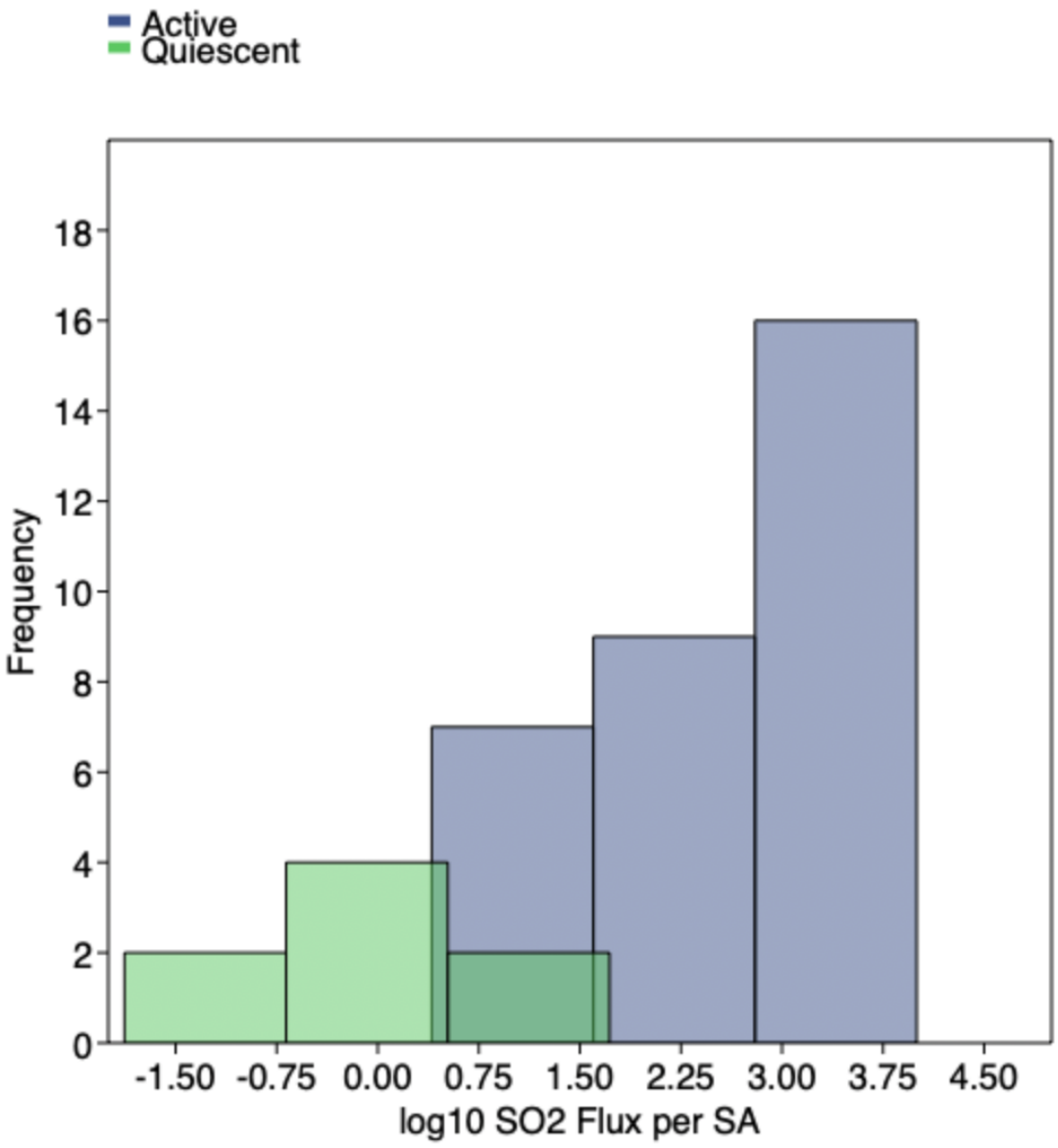


Figure 6. Frequency histogram showing a $\log_{10}$ scale in the x-axis of the SO_2 flux per surface area (SA) in kt yr^{-1} km^{-2}, ranging from -2 to 4 with 5 bins. The peak for Quiescent is from -0.75 to 0.5, whilst the peak for Active volcanism is from 3 to 4

Southern highlands. Hence, it was not possible to calculate a valid volume, density, or mass of its total sulfur. The model only used the surface area of the sedimentary reservoir to predict the total flux, as the mass of this reservoir could not be determined.

RESULTS AND DISCUSSION

Quantifying sulfur release from Noachian to Hesperian volcanism

By assuming an average duration of eruption of 2 Myr (Jiang et al., 2021), the model indicates that 5.8×10^{15} to 5.8×10^{16} kt of sulfur was released into the atmosphere from active degassing (flux of 5×10^{2}–5×10^{3} kt yr^{-1} km^{-2}) and quiescent degassing (flux of 0.5 kt yr^{-1} km^{-2}) from the Noachian-Hesperian periods. Once the sulfur has been released into the atmosphere, it can be deposited and redistributed in a multitude of different ways, however this would not affect the total amount of sulfur present on the surface of Mars. This is because the model assumes a closed system, and hence unlike Gaillard's qualitative model, assumes there are no additional inputs or outputs of sulfur on a planetary scale. Impact events and meteorites would not reintroduce significant amounts of any new material, rather only redistributing on the surface of Mars. This is a valid approach, as the orders of magnitude of

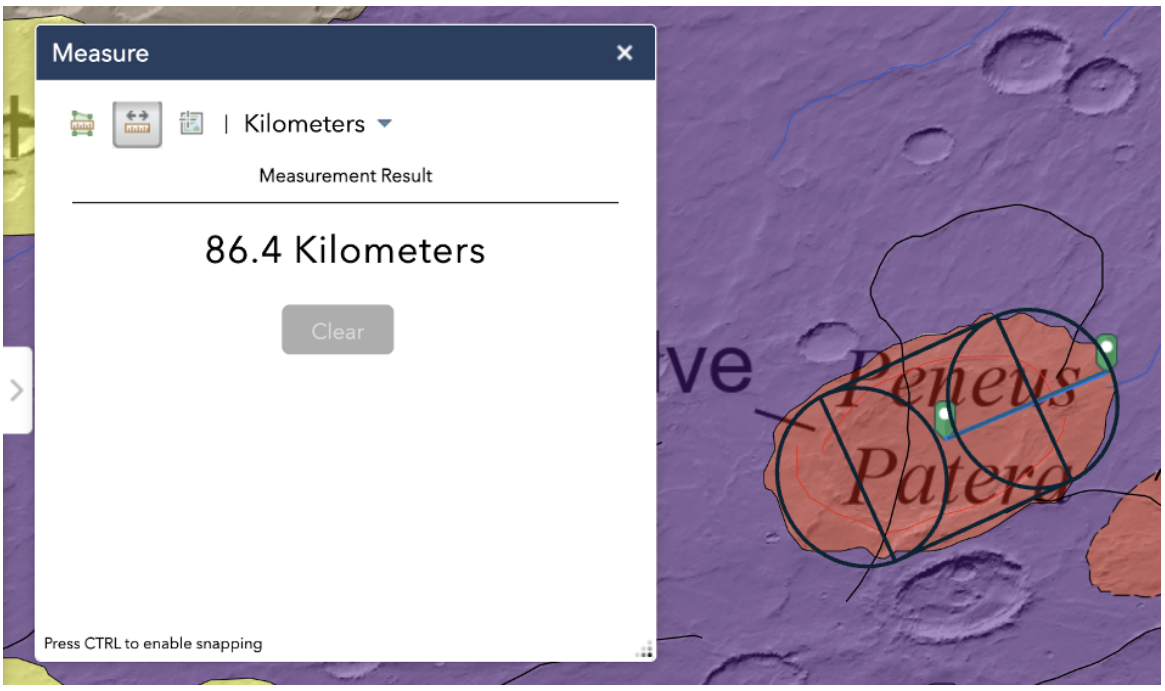


Figure 7. Demonstrating how an image of USGS Interactive Map Measurement tool can be annotated in PowerPoint to produce an area using the map projection shape for a Noachian volcanic unit

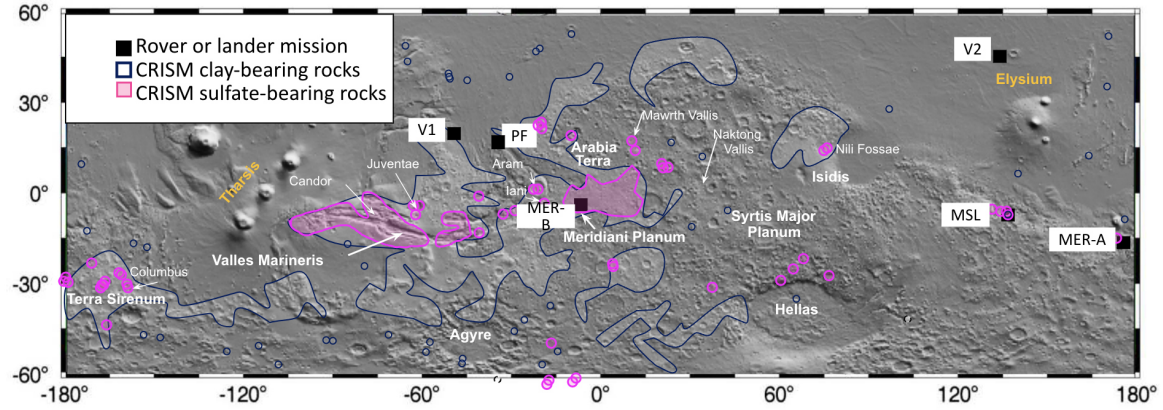


Figure 8. Sulfur and sulfate concentrations and locations on the surface of Mars, overlying a map of Noachian rocks. Sulfate-bearing rocks and phyllosilicate-bearing rocks are based on data from CRISM (Ehlmann and Edwards, 2014). Map from Franz and King 2026

sulfur in consideration as produced by the box model (10^15-10^16 kt) would not be drastically disturbed by the small sulfur content supplied by scattered meteorites. The study also does not consider the effects of hydrothermal transfer between the reservoirs, and only considers volatile output, as it primarily focuses on degassing. This is again a valid approach, as acid and water soluble sulfur species would only be mobilised if infiltrated by groundwater, and would not be sourced from the groundwater itself. The source of S would have to result from volcanic processes.

The assumed duration eruption period of 2 myr, which is the average between 1-5 myr as commonly cited in Jiang et al. (2021), is based on Earth's large igneous provinces; intraplate, mafic igneous volcanic systems. These are intentionally very similar to Martian volcanic conditions. It does not consider the possibility of 32 Myr in magnitude, the maximum cited volcano eruption length, which would shift results by an order of magnitude.

However, since the duration of Martian eruptions is unable to be determined, it is in the best interest to accommodate for a wide range of possibilities for the eruptive time frame.

The final perceived order of magnitude is in agreement with current literature such as Ojha et al. (2019), which found $>10^{14}$ kt (10^{17} kg) of S was delivered to the atmosphere. Similarly, the map

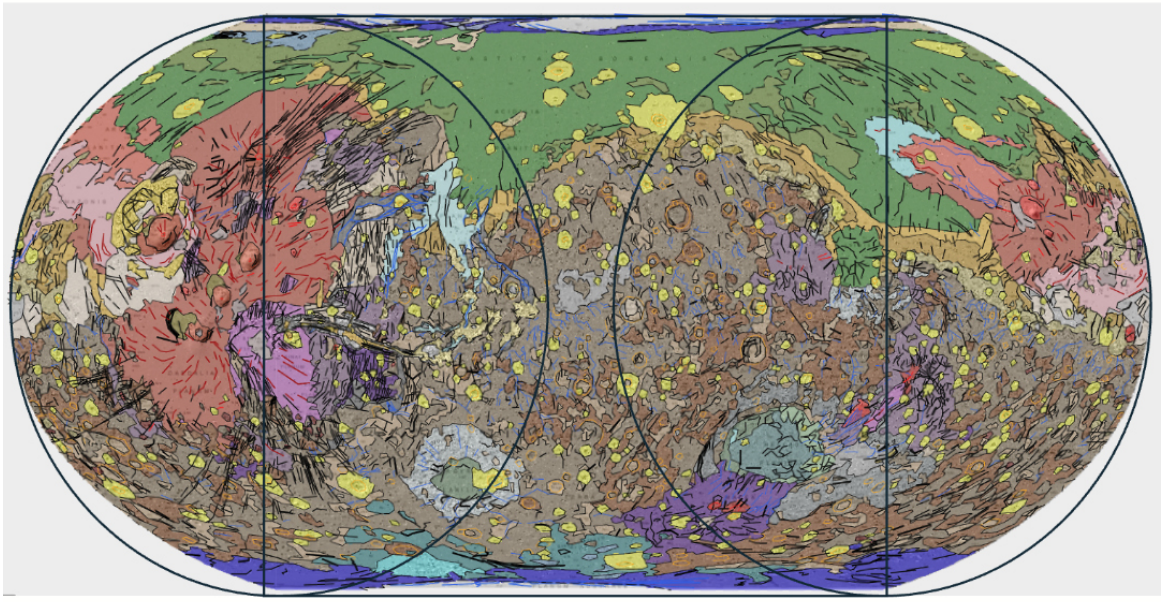


Figure 9. USGS Geologic Map of Mars, modified from Tanaka et al. (2014) with shapes overlain above through PowerPoint package. This model is limited as the irregularity of the shape of volcanic units compared indicates it may overestimate the size of the units

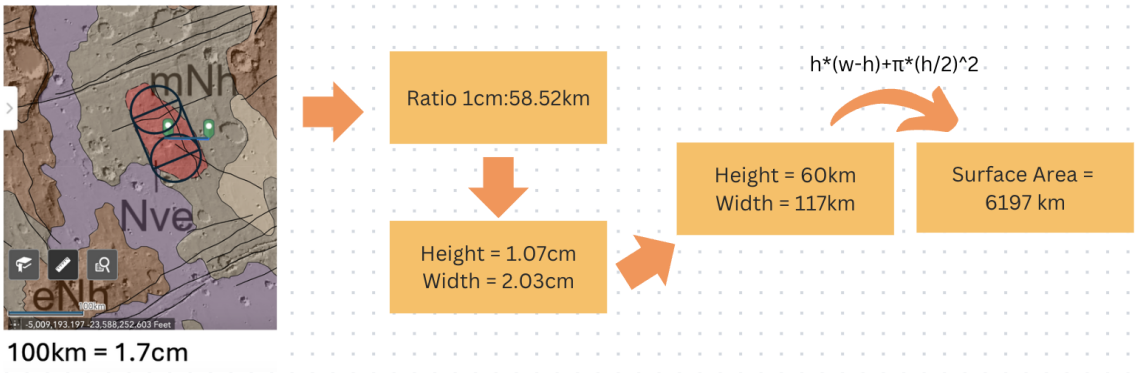


Figure 10. Calculations of one sample of Volcanic Surface Area. When repeated for all samples of Noachian-Hesperian surface area, the final value is 1.1×10^7 km^2. All calculated values can be found in Supplementary Material (Appendix II)

projection method in calculating volume of volcanic rock is consistent with Craddock & Greeley (2009), which estimated a total volume of 4.244×10^7 km^3 of S. The total surface area from map projections of 1.1×10^7 km^2 multiplied with average thickness of 5 km in the Middle Noachian era (Jakosky & Treiman, 2023), provides 5.5×10^7 km^3, which is in the same order of magnitude.

Key limitations

The first key limitation to address is the use of surface areas in order to relate the calculated Earth sulfur output flux to Martian volcanoes. Volcanoes, especially the shield volcanoes mainly observed on Mars, have a gradually decreasing thickness further away from the volcano. This variation in slope also determines the volume of volcanic rock present, and thus provides separate insight into the size of the volcano and its magma chamber.

However, due to the lack of precise depth measurements on Mars, it would be impractical to attempt to account for thickness differences in order to use volume of volcanic rock to relate the two planets. Hence, the assumption was made such that the surface area of a volcano is directly proportional to the rate of sulfur release. As surface area can be deduced using map projections for both Earth and Mars, this factor allowed the flux rates to be related to each other despite differences in topography.

Another key limitation in deriving the sedimentary reservoir size was the use of a Mercator projection geological map, which was necessary as it fea-

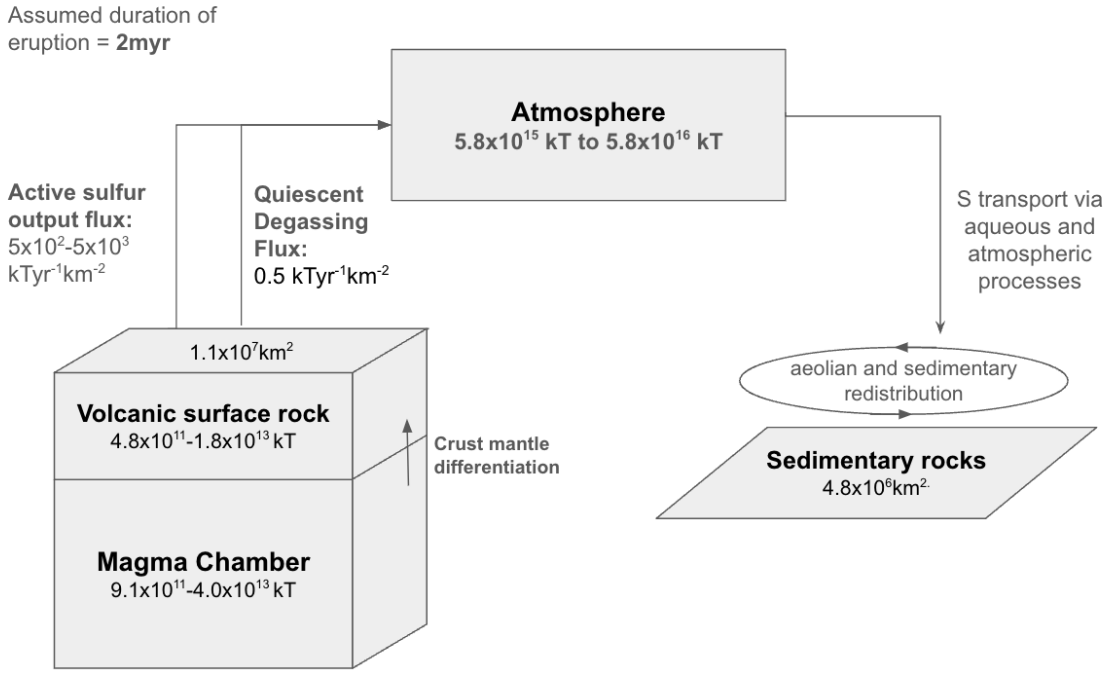


Figure 11. Finalised Box Model, including all relevant values. All values are in elemental S, with reservoir sizes given in kt (10^9 g) of S, as well as surface area of Mars. The total output flux rate (with the addition of quiescent degassing) when multiplied with the eruption period and volcanic surface area produces 5.8×10^{15}–5.8×10^{16} kt of sulfur released into the atmosphere over 2 Myr

tured labelled CRISM sulfur-rich areas. Despite the scale of the map changing with the latitude, each area spans only a small latitudinal range, resulting in minimal error. However, this process would have increased the uncertainty of this method of measurement taking, as there would be an increased number of scales for different latitudes.

Future directions

As this study is the first to attempt to consolidate the total Martian sulfur cycle by using comparative planetology as an estimate of the total sulfur released over time on Mars, more study is necessary to remove confounding variables and address the assumptions made. An immediate next step would be to include the eruption of early-Amazonian volcanoes (Ehlmann & Edwards, 2014; Tanaka et al., 2014) that may have released sulfur. Although difficult to acquire, using more direct data measurements from existing rovers on Mars to calculate a measurement for the average depth of sedimentary soil layers and height of volcanoes would constrain the size of the sedimentary reservoir and find a quantitative mass that could complete the box model. To do this, topographic data, gravitational anomalies, or potentially seismic studies could be used to determine crustal thickness. Such an approach would confirm that the box model is mass balanced if the amount of sulfur released into the atmosphere is comparable with the size of the sedimentary deposit reservoir; further verifying that the methods used in this study are appropriate.

CONCLUSION

This study successfully used Earth analogues and box modelling to provide fluxes for the cycling of sulfur on Mars, notably being the first attempt at applying this concept to the whole planet as a closed system. The principles of comparative planetology were used in selecting a criteria of Earth volcanoes to replicate Martian conditions. Previously overlooked quiescent degassing rates were also considered, increasing the rate of output of sulfur. The final box model approximated $5.8{\times}10^{15}$ to $5.8{\times}10^{16}$ kt of sulfur was released from the Noachian to Hesperian period from volcanism.

A remaining gap is the unknown depth of the sedimentary reservoir, which hinders a calculation of mass balance as current data cannot confirm whether the proposed output sulfur mass

truly matches the observed abundance on Mars. Nonetheless, future studies can consider these calculations and begin to consolidate a sedimentary reservoir size in order to further test the calculated flux rates.

ACKNOWLEDGEMENTS

I would like to thank my Science Extension teacher, Dr Carina Dennis, for her endless support and Dr Karina Sendt for her timely feedback. Their guidance has been invaluable and integral to the success of this report. I would also like to thank my friends who peer reviewed my report and made insightful suggestions.

SUPPLEMENTARY MATERIAL

Supplementary material accompanying this article contains the underlying volcanic sulfur flux data, Martian volcanic surface-area calculations, sulfur reservoir estimates, volcano selection criteria and supporting calculations (Appendices I–VI).

The supplementary PDF is available with the online article at https://doi.org/10.67642/97wtbw66.

REFERENCES

Bibring, J.-P., Langevin, Y., Gendrin, A., Gondet, B., Poulet, F., Berthé, M., Soufflot, A., Arvidson, R., Mangold, N., Mustard, J., & Drossart, P. (2005). Mars surface diversity as revealed by the OMEGA/Mars Express observations. *Science*, *307*(5715), 1576–1581. https://doi.org/10.1126/science.1108806

Carn, S. A., Clarisse, L., & Prata, A. J. (2016). Multi-decadal satellite measurements of global volcanic degassing. *Journal of Volcanology and Geothermal Research*, *311*, 99–134. https://doi.org/10.1016/j.jvolgeores.2016.01.002

Carn, S. A., Fioletov, V. E., McLinden, C. A., Li, C., & Krotkov, N. A. (2017). A decade of global volcanic SO_2 emissions measured from space. *Scientific Reports*, *7*(1), 44095. https://doi.org/10.1038/srep44095

Carn, S. A., Krueger, A. J., Bluth, G. J. S., Schaefer, S. J., Krotkov, N. A., Watson, I. M., & Datta, S. (2003). Volcanic eruption detection by the total ozone mapping spectrometer (TOMS) instruments: A 22-year record of sulphur dioxide and ash emissions. *Geological Society, London, Special Publications*, *213*(1), 177–202. https://doi.org/10.1144/gsl.sp.2003.213.01.11

Casas, A. S., King, P. L., & Delmelle, P. (2026). Sulfur in volcanism. In D. E. Harlov & G. S. Pokrovski (Eds.), *The role of sulfur in planetary processes: From cores to atmospheres* (pp. 767–857). Springer. https://doi.org/10.1007/978-3-032-07705-9_11

Craddock, R. A., & Greeley, R. (2009). Minimum estimates of the amount and timing of gases released into the Martian atmosphere from volcanic eruptions. *Icarus*, *204*(2), 512–526. https://doi.org/10.1016/j.icarus.2009.07.026

Ehlmann, B. L., & Edwards, C. S. (2014). Mineralogy of the Martian surface. *Annual Review of Earth and Planetary Sciences*, *42*(1), 291–315. https://doi.org/10.1146/annurev-earth-060313-055024

Ende, J., & Szynkiewicz, A. (2021). Mechanisms of sulfate formation in acidic hydrothermal sites of Iceland, Lassen, Valles Caldera, and Yellowstone: Implications for possible oxidation pathways in Martian volcanic settings. *Icarus*, *368*, 114608. https://doi.org/10.1016/j.icarus.2021.114608

Franz, H. B., & King, P. L. (2026). Processes involving sulfur on Mars. In D. E. Harlov & G. S. Pokrovski (Eds.), *The role of sulfur in planetary processes: From cores to atmospheres* (pp. 1315–1394). Springer. https://doi.org/10.1007/978-3-032-07705-9_17

Gaillard, F., Michalski, J., Berger, G., McLennan, S. M., & Scaillet, B. (2013). Geochemical reservoirs and timing of sulfur cycling on Mars. *Space Science Reviews*, *174*(1-4), 251–300. https://doi.org/10.1007/s11214-012-9947-4

Hynek, B. M., McCollom, T. M., & Szynkiewicz, A. (2019). Sulfur cycling and mass balance at Meridiani, Mars. *Geophysical Research Letters*, *46*(21), 11728–11737. https://doi.org/10.1029/2019gl085115

Jakosky, B. M., & Treiman, A. H. (2023). Mars volatile inventory and outgassing history. *Icarus*, *402*, 115627. https://doi.org/10.1016/j.icarus.2023.115627

Jiang, Q., Jourdan, F., Olierook, H. K. H., Merle, R. E., & Whittaker, J. M. (2021). Longest continuously erupting large igneous province driven by plume-ridge interaction. *Geology*, *49*(2), 206–210. https://doi.org/10.1130/g47850.1

Moser, D. E., Arcuri, G. A., Reinhard, D. A., White, L. F., Darling, J. R., Barker, I. R., Larson, D. J., Irving, A. J., McCubbin, F. M., Tait, K. T., Roszjar, J., Wittmann, A., & Davis, C. (2019). Decline of giant impacts on Mars by 4.48 billion years ago and an early opportunity for habitability. *Nature Geoscience*, *12*(7), 522–527. https://doi.org/10.1038/s41561-019-0380-0

Ojha, L., Karunatillake, S., & Iacovino, K. (2019). Atmospheric injection of sulfur from the Medusae Fossae forming events. *Planetary and Space Science*, *179*, 104734. https://doi.org/10.1016/j.pss.2019.104734

Shinohara, H. (2008). Excess degassing from volcanoes and its role on eruptive and intrusive activity. *Reviews of Geophysics*, *46*(4). https://doi.org/10.1029/2007rg000244

Szynkiewicz, A., Ende, J. J., & Moore, R. D. (2022). Pathways of sulfur oxidation in volcanic settings: How unanswered questions about sulfate origin on Mars can be addressed. In *53rd Lunar and Planetary Science Conference* (Abstract 2506). Lunar and Planetary Institute. https://www.hou.usra.edu/meetings/lpsc2022/pdf/2506.pdf

Tanaka, K. L., Skinner, J. A., Jr., Dohm, J. M., Irwin, R. P., III, Kolb, E. J., Fortezzo, C. M., Platz, T., Michael, G. G., & Hare, T. M. (2014). *Geologic map of Mars* (Scientific Investigations Map 3292). U.S. Geological Survey. https://doi.org/10.3133/sim3292

i3 ASTA i-Cubed Awards

inquiry, innovation, ingenuity

TAKE YOUR SCIENCE FURTHER

Your next question could take you somewhere extraordinary.



Eight pathways. One national stage.

Since 1951, Science and Engineering Fairs have given young Australians opportunities to investigate questions, test ideas and share discoveries. Today, around 12,000 students participate through state and territory programmes each year, submitting nearly 8,000 independent science and engineering projects.

Students progress through their state or territory science competition. Outstanding projects can then be nominated by their Science Teachers Association to represent their region nationally through the ASTA iCubed Awards. These eight pathways create opportunities for students right across Australia, including rural and regional communities, to have their work recognised.

ASTA is developing the iCubed awards into an in-person Australia Wide Science and Engineering Fair. The event will bring young researchers together to demonstrate their projects, exchange ideas with one another and receive feedback from STEM professionals. For students, presenting and discussing their own research with like-minded peers can be as valuable as the recognition itself.

Teachers, mentors, sponsors and volunteer judges help make these opportunities possible. Whether you're supporting a student project or sharing your expertise, get in touch to find out how you can be involved.

iCubed: The Australia Wide Science and Engineering Fair

VISIT THE VIRTUAL FAIR

Explore current or past projects at i3awards.org.au

SUPPORT STUDENTS

Donate tax free at asta.org.au/donate or get in touch to discuss sponsorship

JUDGE OR VOLUNTEER

Whether at state or national level, volunteers make fairs possible

FIND YOUR STATE OR TERRITORY FAIR

NSW — STANSW Young Scientist
www.youngscientist.au

VIC — Science Talent Search
www.stav.org.au/science-talent-search

QLD — Queensland Science Contest
www.staq.qld.edu.au/competitions/queensland-science-contest

SA — Oliphant Science Awards
www.oliphantscienceawards.com.au

WA — Science Talent Search
www.stawa.net/student-activities/science-talent-search

TAS — Tasmanian Science Talent Search
www.stat.org.au/tsts

ACT — SEAACT Science & Engineering Fair
www.seaact.act.edu.au/science-fair

NT — Territory Young Scientists Awards
www.territoryyoungscientistcompetitionstant.weebly.com

AUSTRALIAN SCIENCE TEACHERS ASSOCIATION

For further information contact the Australian Science Teachers Association
i.cubed.awards@asta.edu.au | **www.asta.edu.au**
Alfred St North Sydney, NSW 2060

YASJ Young Australians Science Journal

Invention of a new device to optimise air quality for vehicle occupants in Sydney's tunnels: the Car Canary

Ellie Cole[1]

[1]Presbyterian Ladies' College Sydney, Sydney, New South Wales, Australia

ABSTRACT

Traffic-related air pollutants (TRAP) present a risk to vehicle occupants (VO) when driving in tunnels. Recirculating vehicle cabin air (RVCA) is the current recommended strategy to protect motorists from TRAP exposure. TRAP and carbon dioxide (CO_2) concentrations were hypothesised to be higher in tunnels, with RVCA reducing TRAP but increasing exposure to CO_2. Air quality testing in tunnels confirmed the presence of TRAP and that CO_2 accumulates in a passenger vehicle when two VO use RVCA. The measured levels of CO_2 indicate poor ventilation and a build up of re-breathed air, which may increase the risk of transmission of airborne viruses when an infectious person is present, along with fatigue or drowsiness that may be relevant to driving behaviour. Three scenarios were tested using different combinations of RVCA and window use. Testing indicated a trade-off: particulate matter 2.5 µm or less in diameter ($PM_{2.5}$) exposure was highest with windows open and lowest with windows closed and RVCA enabled, while CO_2 exposure was highest when RVCA was enabled. Driving with windows closed and RVCA disabled reduced CO_2 exposure but slightly increased $PM_{2.5}$ exposure. To help manage this trade-off, a prototype device known as the Car Canary was developed to alert VO when $PM_{2.5}$ reaches a set point, indicating when to enable RVCA. These preliminary findings from the WestConnex M4–M8 tunnel system suggest that closing windows while using the device to guide RVCA use may help balance exposure to CO_2 and TRAP, although further research is needed. This proof-of-concept device, known as Car Canary was invented and successfully tested in this pilot study.

Young Australians Science Journal
Volume 1, Issue 1, 2026, pp. 38–48
https://doi.org/10.67642/0n025v96

Keywords: Traffic-related air pollutants; Road tunnels; Carbon dioxide; Recirculating vehicle cabin air; $PM_{2.5}$; Car Canary

Student authors: Ellie Cole, Year 12

Address correspondence to authors@yasj.org.au

Type: Research Article
Open access: Yes

Licence: This work is licensed under a Creative Commons Attribution-NonCommercial 4.0 International License (CC BY-NC 4.0).

DOI: 10.67642/0n025v96

YASJ Editors' Note: This study combines environmental measurement with engineering design to investigate air quality in Sydney road tunnels and develop the Car Canary prototype. The progression from sensor comparison to a functioning proof-of-concept device is a particular strength. Readers should note that testing used a single vehicle with two occupants and a relatively small number of replicates, while the low-cost CO_2 sensor showed poor agreement with the research-grade instrument. The findings are therefore preliminary, but provide a strong basis for further testing and development.

INTRODUCTION

Vehicle usage in Australia is increasing, with the largest number of registered vehicles being in New South Wales (NSW) (Australian Bureau of Statistics, 2016, 2022). Emissions from motor vehicles are termed "traffic-related air pollutants" (TRAP) which are associated with adverse health

effects including asthma and cardiovascular disease (Health Effects Institute, 2010). Vehicle occupants (VO) are exposed to the highest concentrations of TRAP within road tunnels (Knibbs et al., 2009; Martin et al., 2016; Morawska et al., 2008). Recirculating vehicle cabin air (RVCA) is one strategy recommended to minimise exposure of TRAP to VO (Transport for NSW, 2023), however RVCA increases the concentration of exhaled carbon dioxide (CO_2). This increases the risk of infection of airborne viruses such as COVID-19 if an infected VO is present (Peng & Jimenez, 2021) and can cause detrimental effects to cognitive function, leading to effects on decision making and poor driving ability (Jung et al., 2017; Satish et al., 2012). Therefore a balance is needed to provide optimal air quality conditions to VO (Kumar et al., 2021).

Although there is a need to mitigate health risks for VO, at present there are no systems or devices developed that balance the risks of exposure to TRAP, CO_2 and infection risk to VO in tunnels. This literature suggests that VO would benefit from the development of a simple yet sensitive device that could alert occupants when it is appropriate to disable RVCA (Kumar et al., 2021).

It was hypothesised that concentrations of both TRAP and CO_2 would be higher inside the tunnel than they would be in non-tunnel environments. Additionally, it was anticipated that VO would be most protected from TRAP when using RVCA and would be most protected from CO_2 when RVCA was turned off. It was also anticipated that $PM_{2.5}$ exposure would be highest when driving with windows open and lowest when driving with windows closed and RVCA enabled, while CO_2 exposure would be highest when RVCA was enabled. In addition, it was hypothesised that a home-made engineered device (HMED) would accurately measure in-vehicle air quality and alert VO at an appropriate time when RVCA should be used to maximise VO health and safety.

MATERIALS AND METHODS

Testing occurred in Sydney's longest section of road tunnel, being the WestConnex M4–M8 system, a 22.km expressway and involved five phases.

Phase 1: Obtaining and constructing monitoring devices

Components were sourced to build a HMED that contained relevant air quality parameters to measure TRAP and CO_2. The HMED was constructed from readily accessible Arduino-compatible components and included particulate matter, particularly fine particles $\leq 2.5\,\mu m$ in diameter ($PM_{2.5}$), nitrogen dioxide (NO_2), and CO_2 sensors. Wires and sensors were secured to the circuit board through soldering. The entire unit was built into a small plastic lunchbox container to keep it secure.

Research grade devices (RGDs) measuring the same parameters were also sourced. These included the Thermo Fisher Scientific Personal DataRAM pDR-1500 monitor, the Honeywell ToxiRAE Pro and the Aranet4 monitor. The aim of using RGDs was to determine the accuracy of the HMEDs and how they correlated to the measurements collected from RGDs.

The HMED and RGDs were placed inside a cardboard box which was placed in the researcher's lap in the passenger seat. Devices were secured to the box with a putty-like adhesive to prevent movement during testing.

Phase 2: In-field test

The HMED and RGDs were used to measure air quality while a vehicle was driven along various testing routes including tunnel and non-tunnel environments.

The researcher performed all measurement activities, while a second VO drove the vehicle which was a 2023 model Volkswagen T-Cross that was powered by regular unleaded petrol. To mimic the typical activities of commuters, testing was undertaken during peak hour.

Seven different routes were used (Table 1). The route taken was determined by the type of test being conducted. Route 1 or 2 involved tunnel testing while non-tunnel (control) testing occurred in Routes 3 to 7. The purpose of control testing was to determine whether air quality inside the tunnel differed from air quality outside the tunnel.

Each device was calibrated before use in accordance with manufacturers instructions. Prior to entering the tunnel, for all tests, the air-conditioning (AC) was turned on, RVCA was turned off and all windows were opened to venti-

Table 1. Testing routes

Route	Start and finish location	Type of route
1	Sydney Olympic Park Aquatic Centre (SOPAC) to Kingsgrove	Tunnel
2	Kingsgrove to SOPAC	Tunnel
3	SOPAC to Balmain	Non tunnel
4	Balmain to SOPAC	Non tunnel
5	Kingsgrove to Balmain	Non tunnel
6	Balmain to Kingsgrove	Non tunnel
7	SOPAC to Kingsgrove	Non tunnel

late the car. VO wore P2 respirators to protect themselves from TRAP during all tests. Upon entry to the tunnel, the time was recorded. An overview of how each tunnel test was carried out is shown in Table 2.

The mitigation strategies listed in Table 2 in the control tests were active upon commencement of the test. For the in tunnel tests, these strategies were active upon entry of the tunnel system. Between 3 to 7 replicates were completed per test.

The data obtained from each device were downloaded after each testing day and analysed in Microsoft Excel.

Phase 3: Preliminary analysis

To compare the control and experimental values received for both CO_2 and TRAP, a T-test for each treatment was performed to determine whether there was a difference between air quality inside and outside of tunnels. Regression analysis determined whether there was a true correlation between measurements collected from the RGD and HMED for each parameter and treatment.

Microsoft Excel was used to perform the analysis and to graph the results.

The parameter in the HMED that most closely correlated to the RGD was selected by comparing the Correlation Coefficient.

The CO_2 concentrations recorded while using RVCA were analysed to determine the average time it took for CO_2 to reach levels that presented a risk to VO.

The results of the statistical analysis were used to select the TRAP parameter that had the closest correlation between the HMED and RGD for use in an improved HMED.

Phase 4: Device construction

Statistical analyses calculated a line of best fit between the HMED parameters and the RGD. That line of fit provided a correction equation which became the code put into the software of an improved prototype device so that the measurements displayed would be corrected to be as close as possible to the measurements from a RGD.

An alarm value was also coded into the software so that the new prototype device would turn on a LED light at a specific set-point. The purpose of the light was to alert VO when to turn RVCA on or off. All coding was performed in Arduino.

The device was improved to be a compact unit that could be safely used in a vehicle. A yellow case was 3D printed and used to house all components. This improved HMED was given the name the "*Car Canary*".

The initial HMED was constructed as shown in Figure 1. All phases were completed between April and August 2024.

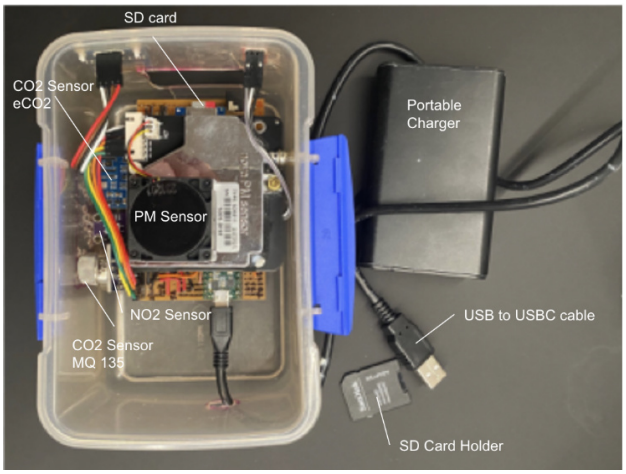


Figure 1. Home-made engineered device (HMED).

Table 2. Purpose of performing each test type

Test	Mitigation strategy	Measuring
A	Windows Open, AC on	TRAP in tunnel
B	Windows Closed, AC on, Fresh Air	TRAP in vehicle in tunnel
C	Windows Closed, AC on, RVCA	CO_2 in vehicle in tunnel
Control A	Control: Windows Open, AC on	TRAP in road
Control B	Control: Windows Closed, AC on, Fresh Air	TRAP in vehicle in road
Control C	Control: Windows Closed, AC on, RVCA	CO_2 in vehicle in road

Phase 5: Device testing

Both the *Car Canary* and the RGD were used to measure air quality in parallel both inside and outside of tunnels. A regression analysis was performed on the data from the *Car Canary* and the RGD to determine whether the results were highly correlated.

To validate and check accuracy, the *Car Canary* was exposed to concentrations above the alarm value to determine whether the LED light turned on at the specific set-point.

Ethics approval for this study was obtained from the school's Ethics Committee in March 2024.

RESULTS

A total of 35 tests of the HMED and RGD were completed in peak hour across various testing routes. Testing was done with the windows open (Test A); windows closed with RVCA disabled (Test B); and with windows closed with RVCA enabled (Test C). Between 3 and 7 replicates of each test were completed.

A review of the trends and the maximum concentrations recorded showed that concentrations of $PM_{2.5}$ rose steadily when driving through the tunnels with windows open or when RVCA was disabled with concentrations decreasing rapidly upon exiting the tunnel. Conversely, concentrations of $PM_{2.5}$ decreased when RVCA was enabled at the start of the trip and increased when RVCA was disabled. The highest concentrations of $PM_{2.5}$ were during Test A (windows open, AC on, in tunnel), and the lowest concentrations were during Test C (windows closed, AC on, RVCA, in tunnel).

Figure 2 displays the average of the maximum concentration of $PM_{2.5}$ for each set of tests recorded by the RGD.

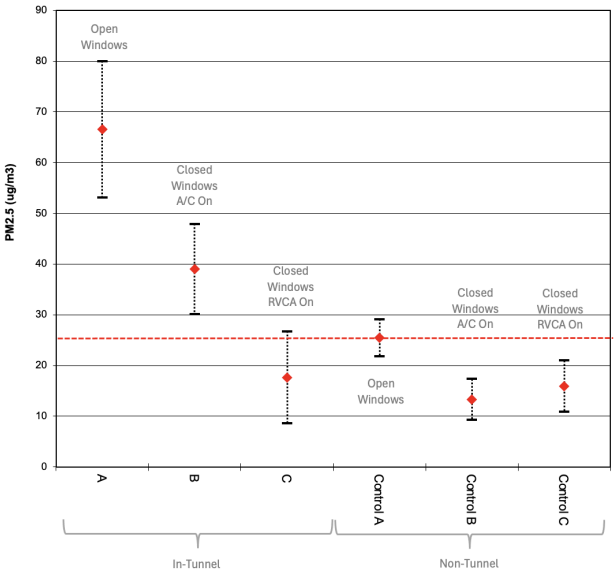


Figure 2. Average maximum concentrations of $PM_{2.5}$ recorded in each test (RGD). The error bars represent one standard deviation. The red line represents the 24-hour trigger limit of $25\,\mu g/m^3$ for $PM_{2.5}$. Values represent $n = 3$–7 replicates per test type.

The maximum concentration of $PM_{2.5}$ exceeded the 24-hour trigger level during Test A and B. During Test A and Test B, it took an average of 6 and 12-minutes respectively to exceed the 24-hour trigger level.

A review of the trends and maximum concentrations recorded in each test was performed for the HMED. Consistent with the RGD, concentrations of $PM_{2.5}$ rose steadily when driving through the tunnels with windows open or when RVCA was turned off with concentrations decreasing rapidly upon exiting the tunnel. Concentrations of $PM_{2.5}$ also decreased when RVCA was turned on and increased when RVCA was disabled. The highest concentrations of $PM_{2.5}$ were during Test A and the lowest concentrations were during Test C (Figure 3).

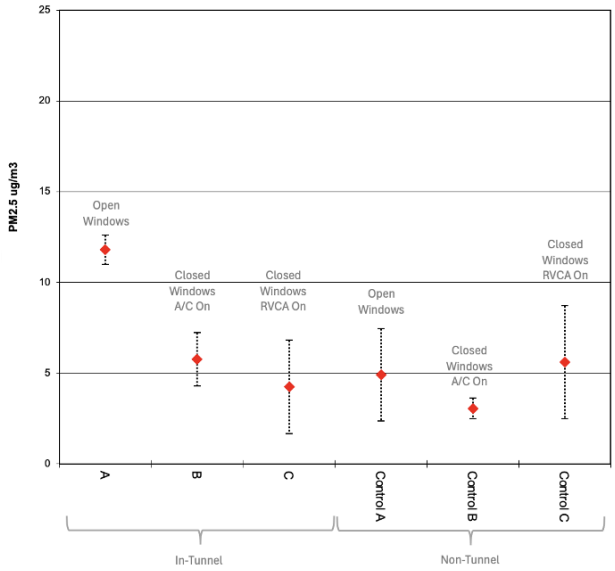


Figure 3. Average maximum concentrations of $PM_{2.5}$ recorded in each test (HMED). The error bars represent one standard deviation. Values represent $n = 3$–7 replicates per test type.

Similar to the RGD, the concentrations of $PM_{2.5}$ measured by the HMED were higher while driving in the tunnel with windows open than they were when RVCA was used. The highest concentrations of $PM_{2.5}$ were during Test A and the lowest concentrations were during Test C.

CO_2 measurements

CO_2 was successfully measured by the RGD and HMED. A review of the trends and the maximum concentrations recorded in each test was performed and showed that concentrations of CO_2 rose during all tests while driving through the tunnel or when RVCA was used. This includes with windows open (Test A), with air-conditioning on and no RVCA (Test B) and with air-conditioning on and recirculated air (Test C). Concentrations of CO_2 were the highest during Test C.

Figure 4 displays the average of the maximum concentrations of CO_2 recorded in each test by the RGD. The red lines represent the trigger limits of 800 ppm, 1000 ppm, and 3000 ppm for CO_2.

There were two CO_2 sensors in the HMED: an eCO_2 and MQ135 sensor. The MQ135 sensor recorded a value that correlates to CO_2 concentrations, however the recorded values had a minimal range (between 35 and 40) and did not change significantly between tests. These data were therefore excluded. The eCO_2 sensor was more sensitive and recorded measurements of CO_2 that ranged between expected ambient concentrations to over 2000 parts per million (ppm). The data from the eCO_2 sensor was included in this analysis.

A review of the trends and maximum concentrations recorded in each test was performed from the HMED. Consistent with the RGD, concentrations of CO_2 rose when driving in the tunnel or when RVCA was enabled. However, concentrations of CO_2 recorded by the HMED were higher in Test A and B compared to Test C.

Figure 5 displays the average of the maximum concentrations of CO_2 recorded in each test by the HMED. The red lines represent the trigger limits of 800 ppm, 1000 ppm, and 3000 ppm for CO_2.

In comparison to the RGD, the HMED did not show significantly different maximum concentrations of CO_2 while driving in the tunnel than when not in the tunnel, nor did it show the highest concentrations when RVCA was used.

Table 3 provides a summary of air quality tests conducted in the tunnel along with the average time it took in minutes to exceed the safety thresholds.

Statistical analysis

An F-test confirmed the control and experimental values of both $PM_{2.5}$ and CO_2 had an equal variance and supported the use of a two-sample t-test assuming equal variances.

The analysis demonstrated that there was a significant difference between Test A and Control A ($PM_{2.5}$ $p = 0.004$, CO_2 $p = 0.000003$) and Test B and Control B ($PM_{2.5}$ $p = 0.0001$, CO_2 $p = 3.3 \times 10^{-5}$). There was no significant difference between Test C and Control C ($PM_{2.5}$ $p = 0.8$, CO_2 $p = 0.3$).

An ANOVA was conducted for both parameters to determine if there was a significant difference between Test A, B and C. The analysis provided evidence to reject the null hypothesis of this statistical test ($PM_{2.5}$ $p = 0.000005$ and $F[30.2] > F_{\text{Critical}}[3.7]$; CO_2 $p = 0.00000002$ and $F[70.3] > F_{\text{Critical}}[3.7]$), indicating that there was a significant difference between the three tests in both parameters.

To determine where this difference was, a Tukey test was conducted on the average $PM_{2.5}$ between tests. The analysis showed there was a significant difference between each test type ($p < 0.01$). For CO_2, the analysis showed there was a significant

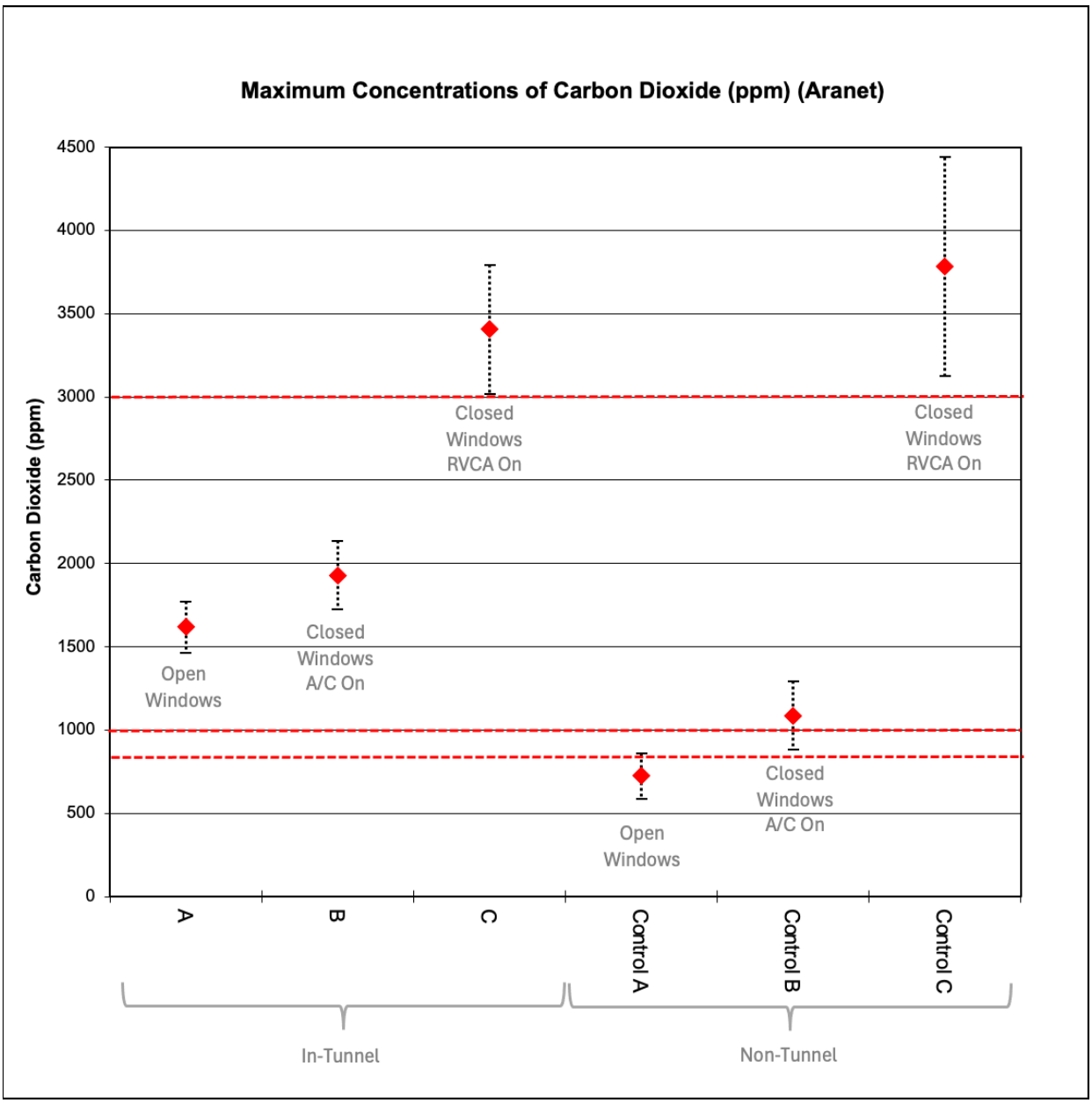


Figure 4. Maximum concentrations of CO_2 recorded in each test by the RGD. The error bars represent one standard deviation. Values represent $n = 3$–7 replicates per test type.

Table 3. Average time to reach threshold values for $PM_{2.5}$ and CO_2 under different mitigation scenarios (NR = not reached)

Parameter	Threshold	Windows Open (min)	Windows Closed RVCA disabled (min)	Windows Closed RVCA enabled (min)
$PM_{2.5}$	25 µg/m^3	6	12	NR
$PM_{2.5}$	50 µg/m^3	14	NR	NR
CO_2	800 ppm	7	2	3
CO_2	1 000 ppm	9	3	4
CO_2	3 000 ppm	NR	NR	16

difference between Test A and C ($p < 0.01$) as well as between Test B and C ($p < 0.01$) but not between Test A and B.

Therefore, there was a significant difference be-

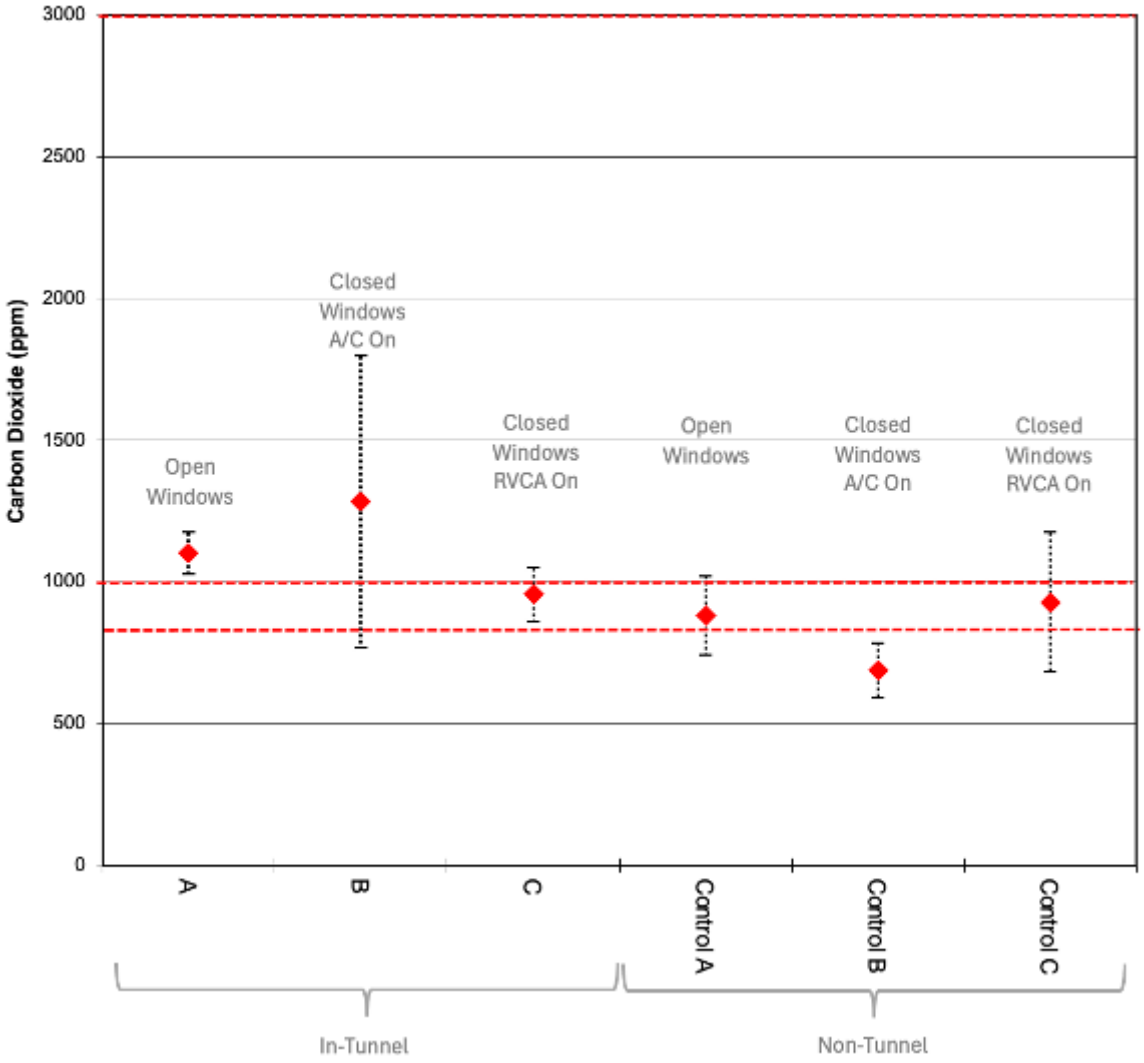


Figure 5. Maximum concentrations of CO_2 recorded in each test (HMED). The error bars represent one standard deviation. Values represent $n = 3$–7 replicates per test type.

tween $PM_{2.5}$ and CO_2 concentrations when driving through tunnels in comparison to a non-tunnel environment when windows were open (Test A) or closed (Test B) without RVCA. However there was not a significant difference between $PM_{2.5}$ or CO_2 concentrations inside the vehicle whether driving through a tunnel or non-tunnel environment when RVCA was used.

$PM_{2.5}$ remained below the threshold values in both tests. Further, the concentrations of $PM_{2.5}$ inside the vehicle were significantly different during each mitigation strategy. Concentrations of CO_2 when using RVCA were significantly different in comparison to when RVCA was disabled.

A regression analysis was performed on the $PM_{2.5}$ data collected from the RGD and the HMED from all Test A results (with outliers omitted). The RGD consistently recorded higher concentrations of $PM_{2.5}$ in comparison to the HMED, but the Pearson Correlation Coefficient was strong (Multiple $R = 0.89$) and the proportion of points that fit the regression line were also high ($R^2 = 0.80$). Figure 6 displays the results of the line of best fit. A regression analysis was performed on the CO_2 data collected from the RGD and the HMED from all Test C results. The RGD consistently recorded higher concentrations of CO_2 in comparison to the HMED. The Pearson Correlation Coefficient was low (Multiple $R = 0.31$) and the proportion of points that fit the regression line were also low ($R^2 = 0.10$). Figure 7 displays the results of the line fit plot.

The TRAP sensor in the HMED that most closely correlated to the scientific grade monitor was $PM_{2.5}$. Therefore it was this parameter selected for use in the improved HMED, known as the *Car Canary*.

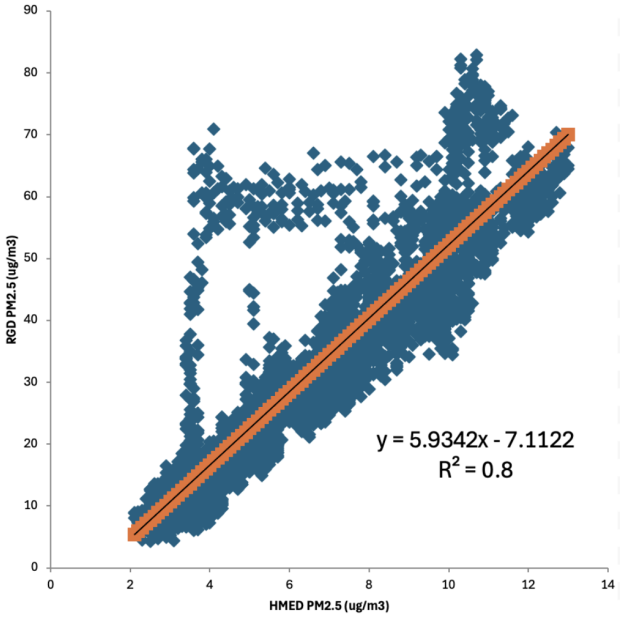


Figure 6. Line Fit Plot of $PM_{2.5}$ data for RGD and HMED measurements.

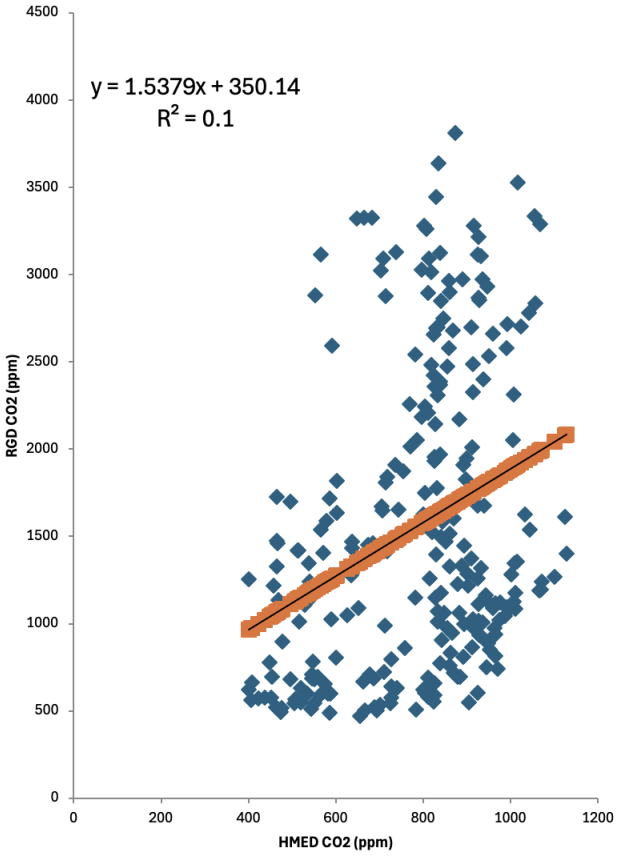


Figure 7. Line Fit Plot of CO_2 data for RGD and HMED measurements.

Car Canary prototype implementation

The Car Canary was upgraded and enhanced using the same low-cost $PM_{2.5}$ sensor as used in the initial testing. Other features included can be seen in Figure 8. The Car Canary was powered by an external USB charger which was connected via USB cable.

The formula below was programmed into the code in Arduino so that the measurements recorded by the $PM_{2.5}$ sensor in the *Car Canary* more closely aligned with the concentrations measured by the RGD:

$$\text{OUTPUT} = 5.9342x - 7.1122 + 8 \qquad (1)$$

where OUTPUT = numbers displayed and recorded by the *Car Canary*, and x = concentration measured by the $PM_{2.5}$ sensor in the *Car Canary*.

The formula was obtained from the line of best fit of $PM_{2.5}$ data and adding a value for the standard error. The standard error represents the value that the average calculated values were to the regression line of the data, which was 8 µg/m^3.

Other items included in the code in Arduino were to include a trigger limit of 50 µg/m^3. At that value, the Car Canary was programmed to turn on an LED light when $PM_{2.5}$ concentrations reached or exceeded 50 µg/m^3. To minimise the light turning on and off when $PM_{2.5}$ concentrations are near that limit, the measurements were programmed to run as a 10-second average. The value of 50 µg/m^3 was selected as a conservative measure to keep average exposures to VO below 25 µg/m^3. This is further explained in the discussion. A copy of the code can be provided upon request.

DISCUSSION

This investigation explored whether a HMED could monitor air quality and alert VO to enable or disable RVCA to minimize health risks. Testing focused on NO_2, $PM_{2.5}$, and CO_2 in tunnels. NO_2 was undetectable and excluded from analysis. $PM_{2.5}$ and CO_2 showed significant differences in air quality inside and outside tunnels with RVCA on or off.

It was found that:

- $PM_{2.5}$ concentrations were highest with win-

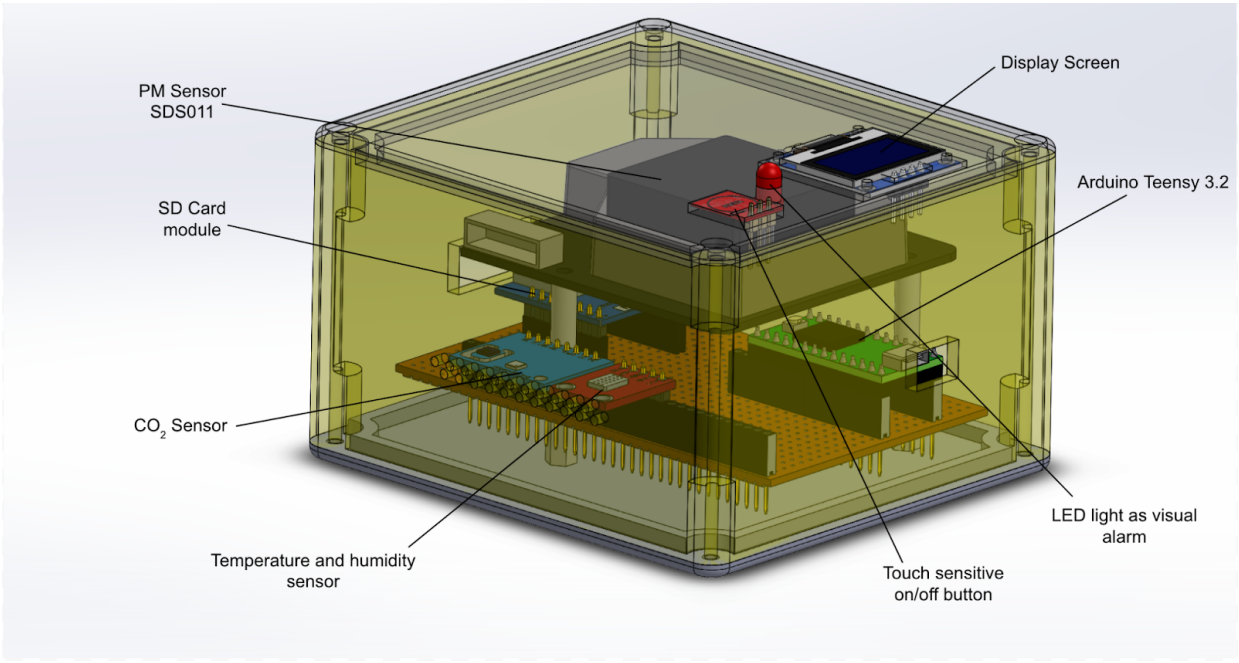


Figure 8. Car Canary layout and enclosure design.

dows open and lowest with windows closed and RVCA enabled, supporting the hypothesis that closing windows and enabling RVCA protects VO from TRAP exposure.

- CO_2 concentrations were highest with RVCA enabled and lowest with windows open. CO_2 levels exceeded trigger thresholds with RVCA enabled.
- A significant difference in CO_2 levels between Test A and Control A ($p < 0.05$) and Test B and Control B ($p < 0.05$) indicated additional CO_2 sources, likely vehicle exhaust. No significant difference was found between Test C and Control C ($p > 0.05$), confirming VO as the primary CO_2 source in those tests.

High CO_2 exposure is associated with risks of fatigue, and is a proxy for poor ventilation and re-breathed air. An increased infection risk arises from accumulation and recirculation of virus-laden aerosols when an infectious person is present. Reducing CO_2 exposure may therefore be beneficial. TRAP is also associated with adverse health effects including asthma and cardiovascular disease (Health Effects Institute, 2010). Disabling RVCA while keeping windows closed and AC on fresh air reduced CO_2 exposure but slightly increased $PM_{2.5}$ exposure.

In regards to device effectiveness, the $PM_{2.5}$ sensor in the HMED closely matched scientific-grade monitors, while the CO_2 sensor showed poor accuracy at high concentrations. The Car Canary prototype effectively alerted VO when $PM_{2.5}$ exceeded 50 µg/m^3, prompting RVCA activation to limit exposure.

The quality of the data was considered when interpreting these results. For $PM_{2.5}$, the home-made device correlated strongly with the research-grade monitor (Multiple $R = 0.89$; $R^2 = 0.80$), suggesting the $PM_{2.5}$ measurements were reasonably accurate, although the device consistently read lower than the research-grade monitor, which was corrected using a line of best fit. In contrast, the CO_2 sensor correlated poorly with the research-grade monitor (Multiple $R = 0.31$; $R^2 = 0.10$), so the CO_2 concentrations from the home-made device should be treated with caution and were not used in the final device. Precision and reliability were also limited by the small number of replicates (between three and seven per test) and by the use of a single vehicle with two occupants, which restricts how far the findings can be generalised. These results are broadly consistent with previous studies reporting elevated TRAP for vehicle occupants in road tunnels (Knibbs et al., 2009; Martin et al., 2016; Morawska et al., 2008) and with reports that recirculating cabin air can reduce particle exposure while affecting CO_2 concentrations (Jung et al., 2017; Kumar et al., 2021).

The limitations of this research include: limited TRAP parameters being measured due to time and material constraints and specific controls used that may not apply to all cars (e.g., vehicles with

more or less than 2 passengers). This study used the WestConnex M4–M8 tunnel system. The application of these results to other tunnel systems were not assessed.

Enhancements to the device could include monitoring multiple TRAP parameters and automating RVCA control for optimal air quality management. The study could be strengthened by including more replicates across varied vehicle types and routes, and by testing higher occupancy levels, which would directly increase CO_2 accumulation.

This study highlights the need for improved sensor accuracy and expanded TRAP monitoring to refine strategies for minimizing VO exposure to air pollutants and CO_2 in tunnels, however the findings provide valuable preliminary information and proof of concept.

CONCLUSION

Exposure to TRAP in tunnels poses a health risk to VO. This study reports TRAP and CO_2 concentrations being higher inside the WestConnex M4–M8 tunnel system, highlighting the need for targeted interventions. Air quality varied by treatment, with RVCA offering the most protection from TRAP but leading to CO_2 buildup. CO_2 levels exceeded 800 ppm in 3 minutes, 1000 ppm in 4 minutes, and 3000 ppm in 16 minutes. CO_2 at these levels has been associated with risks to cognitive function, fatigue, and infection transmission. While RVCA is the recommended mitigation strategy, this preliminary study suggests that prolonged use may increase exposure to CO_2.

To further reduce TRAP exposure, the study introduced Car Canary, a prototype device that alerts VO when TRAP reaches a critical level, signaling when to enable RVCA. This research provides valuable preliminary evidence and proof of concept, filling a gap by developing a device to balance TRAP and CO_2 exposure risks, with the aim of enhancing driver health and safety.

ACKNOWLEDGEMENTS

I have the following acknowledgements to make:

- My Science mentor, Dr Stephanus Van Heerden who supported me with the construction and coding of the HMED and the *Car Canary* in Arduino.
- My grandfather Chris McDonald, who taught me how to solder and lent me his soldering iron to construct the home-made devices in this study.
- My mother Kate Cole who guided me to resources to support the development of this project as well as the use of specific terminology and ways to structure a scientific report.
- Nikita Hains for providing guidance on the structure of the proposed methodology.
- Active Environmental Solutions for providing the RGD to measure NO_2 at no charge.
- PLC Sydney for providing $250 from the school's science extension fund to help fund this project.
- My Science Extension teacher, Dr Maria-Luisa Gutierrez who provided feedback and guidance on the content of this report.

REFERENCES

Australian Bureau of Statistics. (2016). *Motor vehicle census, Australia, 31 Jan 2016*. https://www.abs.gov.au/ausstats/abs@.nsf/Lookup/9309.0main+features131%20Jan%202016

Australian Bureau of Statistics. (2022). *Transport: Census, 2021*. https://www.abs.gov.au/statistics/industry/tourism-and-transport/transport-census/latest-release

Health Effects Institute. (2010). *Traffic-related air pollution: A critical review of the literature on emissions, exposure, and health effects* (Special Report 17). https://www.healtheffects.org/node/375

Jung, H. S., Grady, M. L., Victoroff, T., & Miller, A. L. (2017). Simultaneously reducing CO_2 and particulate exposures via fractional recirculation of vehicle cabin air. *Atmospheric Environment*, *160*, 77–88. https://doi.org/10.1016/j.atmosenv.2017.04.014

Knibbs, L. D., de Dear, R. J., Morawska, L., & Mengersen, K. L. (2009). On-road ultrafine particle concentration in the M5 East road tunnel, Sydney, Australia. *Atmospheric Environment*, *43*(22–23), 3510–3519. https://doi.org/10.1016/j.atmosenv.2009.04.029

Kumar, P., Omidvarborna, H., Tiwari, A., & Morawska, L. (2021). The nexus between in-car aerosol concentrations, ventilation and the risk of respiratory infection. *Environment International*, *157*, 106814. https://doi.org/10.1016/j.envint.2021.106814

Martin, A. N., Boulter, P. G., Roddis, D., McDonough, L., Patterson, M., Rodriguez del Barco, M., Mattes, A., & Knibbs, L. D. (2016). In-vehicle nitrogen dioxide concentrations in road tunnels. *Atmospheric Environment*, *144*, 234–248. https://doi.org/10.1016/j.atmosenv.2016.08.083

Morawska, L., Ristovski, Z., Jayaratne, E. R., Keogh, D. U., & Ling, X. (2008). Ambient nano and ultrafine particles from motor vehicle emissions: Characteristics, ambient processing and implications on human exposure. *Atmospheric Environment*, *42*(35), 8113–8138. https://doi.org/10.1016/j.atmosenv.2008.07.050

Peng, Z., & Jimenez, J. L. (2021). Exhaled CO_2 as a COVID-19 infection risk proxy for different indoor environments and activities. *Environmental Science & Technology Letters*, *8*(5), 392–397. https://doi.org/10.1021/acs.estlett.1c00183

Satish, U., Mendell, M. J., Shekhar, K., Hotchi, T., Sullivan, D., Streufert, S., & Fisk, W. J. (2012). Is CO_2 an indoor pollutant? Direct effects of low-to-moderate CO_2 concentrations on human decision-making performance. *Environmental Health Perspectives*, *120*(12), 1671–1677. https://doi.org/10.1289/ehp.1104789

Transport for NSW. (2023). *Using Sydney's tunnels*. https://www.transport.nsw.gov.au/operations/nsw-roads-network/using-sydneys-tunnels

YASJ Young Australians Science Journal

How concentration, temperature, and pH affect soapberry's cleaning power compared to commercially available detergents

Alexandra Prokhorov[1]
[1]PLC Sydney, Sydney, NSW, Australia

ABSTRACT

The widespread use of synthetic cleaning products significantly contributes to environmental pollution, creating the need for natural alternatives. In this study, the capillary tube method was used to investigate the effect of concentration, temperature and pH on the effectiveness of soapberry as a plant-based detergent and compare its effectiveness to commercially available detergent and bio-detergent. Effectiveness was measured as a decrease in surface tension, which in turn affects the formation of micelles that enclose lipids and dissolve grease and oils. The results of this study showed that greater effectiveness was achieved at higher concentration (5%), temperature (60°C) and pH (12) of soapberry surfactant and found soapberry to be more effective than water (control), similarly as effective as commercial bio-detergent, and less effective than commercial detergent. These findings support the use of soapberry in both domestic and industrial settings as an alternative to commercial cleaning products, reducing the chemical and plastic pollution associated with conventional detergents.

Young Australians Science Journal
Volume 1, Issue 1, 2026, pp. 49–55
https://doi.org/10.67642/psaek593

Keywords: soapberry; surface tension; surfactant; saponin; critical micelle concentration; natural detergent; environmental sustainability

Student authors: Alexandra Prokhorov, Year 10

Address correspondence to authors@yasj.org.au

Type: Research Article
Open access: Yes
Licence: This work is licensed under a Creative Commons Attribution-NonCommercial 4.0 International License (CC BY-NC 4.0).
DOI: 10.67642/psaek593

YASJ Editors' Note: This study systematically investigates soapberry as a potential alternative to commercial cleaning products by examining the effects of concentration, temperature and pH on surface tension. Comparison with conventional detergent, bio-detergent and water provides a clear experimental framework. Readers should note that surface tension was used as a proxy for cleaning effectiveness rather than measuring soil or oil removal directly, and that the capillary-tube method introduces measurement assumptions and uncertainty. Further direct cleaning-performance testing would strengthen the practical conclusions of the investigation.

INTRODUCTION

Hygiene is one of the most significant aspects of human life. Maintaining good hygiene is crucial in order for humans to survive (Curtis, 2007). As a result, humans themselves have developed, engineered and produced an immense range of hygiene and cleaning products for their homes and environments. The widespread use of these products has contributed to the development of a substantial commercial industry, with the global household cleaners market generating approximately USD 39.79 billion in revenue in 2024 and projected to grow at a compound annual growth rate of 3.17% between 2024 and 2029 (Statista, 2024).

However, over time, with the discovery of more chemicals and resources, as well as increased knowledge of their properties and applications, these everyday cleaning products have become increasingly complex mixtures containing harsh and potentially toxic chemicals. Such chemicals can pose risks not only to humans, but also to the environment and the flora and fauna it encompasses, primarily through entering aquatic environments as greywater (Yuan et al., 2014). Persistent contaminants in particular can remain in environmental systems for extended periods due to their resistance to degradation, leading to their accumu-

lation within organisms when uptake occurs faster than elimination — a process known as bioaccumulation. Once absorbed, these chemicals may undergo biotransformation, whereby metabolic processes alter their chemical structure, further affecting their toxicity, persistence and elimination. Moreover, contaminants can be transferred between organisms through feeding and accumulate at higher trophic levels through biomagnification, increasing exposure among organisms higher in the food chain, including humans (Mackay et al., 2018).

For example, triclosan (TCS), an antimicrobial compound commonly used in products such as hand soaps and cosmetics, has been detected in human body fluids across all age groups, with evidence indicating that prolonged exposure may adversely affect multiple biological systems, including hormone homeostasis and liver function (Yueh & Tukey, 2016). Similarly, lead is a cumulative toxicant that can affect multiple body systems, including the neurological, haematological, gastrointestinal, cardiovascular and renal systems; long-term exposure is particularly harmful to children, in whom even relatively low exposure can cause serious and, in some cases, irreversible neurological effects (World Health Organization, 2025).

Additionally, commercial bio-detergents — while specifically designed to replace some harmful components found in conventional detergents using enzymes such as cellulase and lipases (Ito et al., 2005) — are still manufactured cleaning products that require industrial processing and plastic packaging. As a result, both detergents and bio-detergents contribute to the release of toxic chemicals that end up in the ocean, in marine ecosystems, and even in seafood (Couture, 2019), with the chemicals in their plastic packaging, such as flame retardants, also being highly persistent in the environment, impacting coral in particular (Aminot et al., 2020).

However, some resources in nature can be used to perform the same function as artificial cleaning products without causing as much harm. An example of such a resource is the soapberry tree, *Sapindus* — from 'sapo', Latin for 'soap' — which is found in warm temperate and tropical regions such as China and India (Liu et al., 2021). The fruits of this tree, also known as soapnuts, contain organic compounds called saponins, which act as natural surfactants. The key ingredient in detergents and soaps, surfactants are chemical compounds that decrease surface tension and form micelles, molecular structures that enclose lipids and dissolve grease and oils (Kregiel et al., 2017), allowing for effective cleaning. Not only is this property of soapberries not limited to domestic applications — soapberry-derived saponins have also been used to facilitate the removal of heavy metals from contaminated soil (Maity et al., 2013) — but their many beneficial properties make them an environmentally friendly alternative across a range of applications.

Soapberries are natural, free of artificial chemicals, hypoallergenic, greywater safe, zero waste, biodegradable, antibacterial and antifungal (Rai et al., 2021). By not needing to be contained in plastic packaging and being themselves fully biodegradable, as well as lacking artificial chemicals, soapberries completely eliminate any plastic and chemical pollution that could occur from their widespread use. In addition, soapberries are commercially viable due to their low cost and accessibility; they are readily available for purchase online with a 1 kg bag costing approximately 10c per wash, compared with around 50c per wash for commercial bio-detergent (Only 1 Earth, 2022).

However, despite soapberries' numerous beneficial qualities, their use by the public and in the industry is very limited. This is likely due to the greater trust, chemical strength, and cleaning efficiency that conventional cleaning products possess. Therefore, more research into the properties of soapberries and how they function, how to enhance their properties, and their effectiveness in comparison to conventional cleaning products can increase their cleaning capability and make their use as an alternative more widespread, benefiting the environment.

Thus, this study was designed to determine the optimum conditions for the use of soapberries as a cleaning agent and assess their effectiveness as an alternative to commercially available cleaning products. Specifically, it investigated the effect of surfactant concentration, temperature and pH on soapberry effectiveness, measured through surface tension, and compared the effectiveness of soapberry with water (control), commercial detergent and commercial bio-detergent. Lower surface tension facilitates the formation of micelles, which enclose lipids and dissolve grease and oils, thereby contributing to cleaning effectiveness. The critical micelle concentration (CMC) is the concentration

point at which micelles are formed and after which surface tension remains relatively constant; therefore, determining the CMC of soapberry provides an indication of the concentration required for effective surfactant activity.

The variables surfactant concentration, temperature and pH were selected based on their potential effects on surfactant performance. As indicated by the CMC, a certain concentration of surfactant is required to form micelles and hence function effectively; the CMC of the *Sapindus* saponin extracted from pods has been determined to be 0.75%, and 0.45% when extracted from the pericarp (Balakrishnan et al., 2006; Rai et al., 2021). Temperature was selected because changes in molecular thermal activity can alter cohesive forces and intermolecular interactions within a solution, and temperature has been shown to impact the efficiency of soapberry-derived saponin (Maity et al., 2013). Additionally, commercial laundry detergents have been shown to contain ingredients to control and maintain pH, commonly including alkaline builders that help produce and maintain an alkaline environment, which can contribute to cleaning effectiveness.

Hence, it was hypothesised that increases in soapberry surfactant concentration (until a CMC level of 0.75%), temperature and pH would lead to a decrease in surface tension and hence an increase in effectiveness; and that soapberry would perform more effectively than water, similarly as effectively as commercial bio-detergent, and less effectively than commercial detergent.

MATERIALS AND METHODS

Method for calculating surface tension

Surface tension was determined using the capillary tube method. Capillary tubes of 1 mm inner diameter and the Duratech TD-2081 Digital vernier calliper were used to measure the change in water level and the following formula was used to calculate surface tension:

$$T = \frac{\rho \times \pi \times g \times r^2 \times h}{\cos(\theta) \times 2 \times \pi \times r}$$

where T is the surface tension (N/m); ρ is the density (kg/m^3); π is the constant 3.14; g is the force of gravity (9.8 m/s^2); r is the capillary tube radius (0.0005 m); h is the height travelled (m); and $\cos(\theta) = 1$ (where θ is the contact angle between the liquid and the glass of the capillary tube, assumed to equal 0°).

Experiment 1: Effect of concentration on surface tension

Organic soapnut powder (*Sapindus mukorossi*) from Root2Leaf Organic, laundry detergent powder from Cussons Radiant, laundry bio-detergent powder from Earth Choice, and an AMIR Digital Mini Scale and Intllab magnetic stirrer were used. Solutions of 0%, 0.5%, 1%, 2%, 3%, 4% and 5% (w/v) concentration of each of the agents were prepared by weighing 0 g, 0.5 g, 1 g, 2 g, 3 g, 4 g and 5 g of powder, adding to 100 ml of deionised water and stirring for 1 min at bar 4. Surface tension was calculated using the method provided. The Critical Micelle Concentration (CMC) point for each agent was identified graphically using the data collected.

Experiment 2: Effect of temperature on surface tension

The IVYX Scientific Thermostatically controlled water bath and Pasco Temperature Probe were used to achieve solution temperatures of 20°C, 25°C, 30°C, 40°C, 50°C and 60°C for water (control), and 1% concentration solutions of soapberry, detergent and bio-detergent (prepared using the method in Experiment 1). Surface tension was calculated using the method provided.

Experiment 3: Effect of pH on surface tension

Solutions of pH 4, 7 and 12 of each of the agents at 1% concentration were prepared by addition of hydrochloric acid (0.01 M) or sodium hydroxide (1 M) to deionised water [soapberry — 20:0:80, 0:0:100, 0:10:90; detergent and bio-detergent — 60:0:40, 10:0:90, 0:0:100]. The pH values were measured using the Techvida Digital pH Meter. Surface tension was calculated using the method provided.

Data analysis

To ensure precision, all the experiments were performed in replicate and results were presented as averages of the replication values. A One-Way ANOVA statistical analysis was performed using the Data Analysis Tool in Excel, which compared the surface tension of the different types of surfactants at critical micelle concentration level and water (control) in order to see if they were signif-

icantly different ($\alpha = 0.05$). A series of t-tests were further performed using the Data Analysis Tool in Excel, which compared surface tension at the critical micelle concentration for different types of surfactants in order to see if they were significantly different.

RESULTS

The results of Experiment 1 showed that surface tension decreased as the concentration of all three surfactants (soapberry, detergent and commercial bio-detergent) increased until the critical micelle concentration levels of 0.65% (Figure 1), 0.70% (Figure 2) and 1.06% (Figure 3) were reached, respectively.

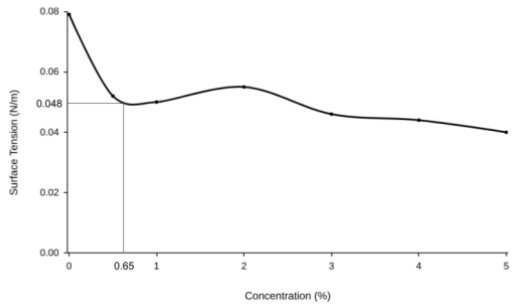


Figure 1. Average surface tension (N/m) of soapberry at increasing concentrations. Surface tension decreased until the critical micelle concentration (CMC) of 0.65% was reached, after which it remained relatively constant.

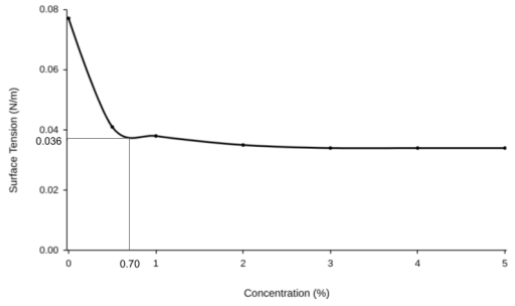


Figure 2. Average surface tension (N/m) of detergent at increasing concentrations. Surface tension decreased until the critical micelle concentration (CMC) of 0.70% was reached, after which it remained relatively constant.

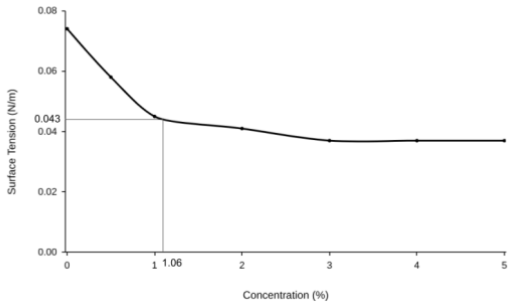


Figure 3. Average surface tension (N/m) of bio-detergent at increasing concentrations. Surface tension decreased until the critical micelle concentration (CMC) of 1.06% was reached, after which it remained relatively constant.

Comparing soapberries, detergent, and commercial bio-detergent based on their critical micelle concentration and water (control) showed that water had the highest surface tension of 0.077 N/m as expected, detergent had the lowest surface tension of 0.036 N/m, soapberry and commercial bio-detergent had similar surface tension of 0.048 N/m and 0.043 N/m, respectively, and the surface tension of soapberry and commercial bio-detergent was higher than detergent and lower than water (Figure 4). The data analysis showed that the surface tension of surfactants and water was significantly different (F-value = 7.918, p = 0.001, α = 0.05, One-Way ANOVA) and the surface tension of soapberry was significantly different from the surface tension of detergent (p = 0.022, α = 0.05, t-test) and water (control) (p = 0.035), but not significantly different from commercial bio-detergent (p = 0.429). The results of Experiment 2 showed that as the temperature increased the surface tension of all three types of surfactants and water (control) decreased; higher surface tensions were achieved at the lowest temperature of 20°C and lower surface tension was observed at 50°C–60°C (Figure 5). The results of Experiment 3 showed that as the pH level increased, the surface tension decreased for all three surfactants; higher surface tensions (0.062 N/m, 0.053 N/m, 0.0471 N/m) were observed in the acidic environment pH 4, and lower surface tensions were noted at the neutral pH 7 and basic pH 12 levels (Figure 6).

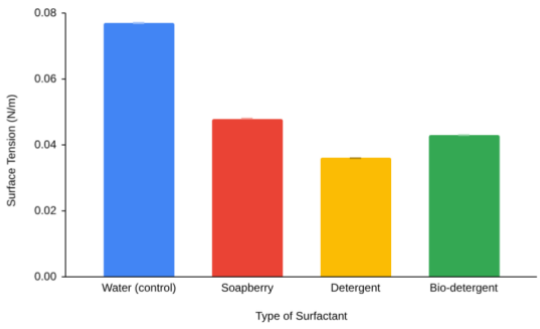


Figure 4. Average surface tension (N/m) of water (control), soapberry, detergent and bio-detergent at their respective critical micelle concentrations. Water had the highest surface tension (0.077 N/m), while detergent had the lowest (0.036 N/m); soapberry and bio-detergent had surface tensions of 0.048 N/m and 0.043 N/m, respectively.

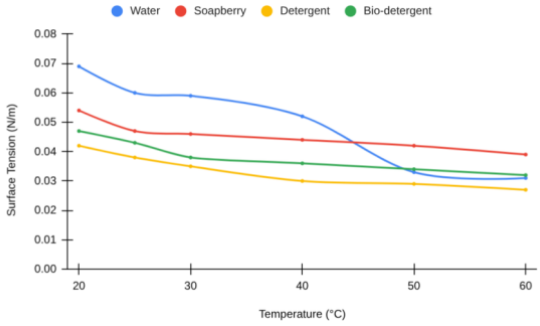


Figure 5. Average surface tension (N/m) of water (control), soapberry, detergent and bio-detergent at increasing temperatures. Surface tension decreased as temperature increased across all four substances.

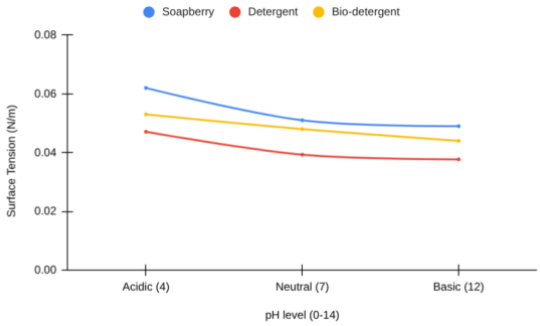


Figure 6. Average surface tension (N/m) of soapberry, detergent and bio-detergent under acidic (pH 4), neutral (pH 7) and basic (pH 12) conditions. Surface tension decreased as pH increased across all three surfactants.

DISCUSSION

The widespread use of commercial cleaning products contributes to increasing levels of environmental pollution and plastic waste, creating a need for effective and environmentally sustainable alternatives. The findings of this study support the potential of soapberry as such an alternative, suggesting that although soapberry may not provide equivalent surfactant performance to conventional detergent, it has potential as a lower-impact alternative to commercial bio-detergents.

The results supported the established inverse relationship between surfactant concentration and surface tension until the critical micelle concentration (CMC) is reached (Yuan et al., 2014). The surface tension of all three surfactants (soapberry, detergent and commercial bio-detergent) decreased as concentration increased until their respective CMC levels were reached, with the CMC of soapberry (0.65%) being close to the hypothesised and previously reported value of 0.75% (Balakrishnan et al., 2006; Kregiel et al., 2017; Rai et al., 2021). This indicated that all three substances had functioned as surfactants under the conditions tested.

The lower surface tension of detergent compared with soapberry and commercial bio-detergent was consistent with previous research showing that conventional detergents can produce greater reductions in surface tension due to their additional chemical components (Fuchs, 2015), while the similar (not significantly different) surface tension of soapberry and commercial bio-detergent was consistent with research indicating that commercial bio-detergents contain plant-based ingredients similar to those present in soapberry (Azuokwu et al., 2021). This suggests that soapberry may provide similar surfactant performance to commercial bio-detergent while avoiding the need for industrial processing and plastic packaging.

To further enhance this performance, conditions such as temperature and pH are important to consider. The observed trend of decreasing surface tension as temperature and pH increased supported the hypothesis and was consistent with previous research (Rai et al., 2021). This trend was observed across all three surfactants, as well as water (control) for temperature, suggesting that the effects of temperature and pH on surface tension are not unique to soapberry but may reflect more general effects on surfactant performance. This supports the potential for optimisation of temper-

ature and pH conditions to further improve the cleaning effectiveness of soapberry and incentivise its use.

The findings have implications for the use of soapberries as an alternative cleaning product in domestic settings. Although soapberry had lower surfactant performance than commercial detergent, its similar performance to commercial bio-detergent suggests that it may provide a lower-impact alternative to manufactured bio-detergents. This is particularly relevant given that soapberries do not require industrial processing or plastic packaging, potentially reducing the environmental impacts associated with manufactured cleaning products. The optimisation of concentration, temperature and pH conditions may further enhance the appeal and practical application of soapberry and support investigation into its use in other settings, including industrial applications such as soil and oil remediation.

The reliability of the findings was supported by the close agreement between the calculated density of water (921 kg/m^3) and its accepted value (1000 kg/m^3), as well as between the measured surface tension of water at 25°C (0.060 N/m) and its accepted value (0.071 N/m). Measurement readings were performed at eye level to minimise parallax error, and the small standard deviation and range across the data indicated consistency between repeated trials. All variables, apart from the independent variable in each experiment, were controlled, supporting the reproducibility of the results. These factors support the validity of the capillary tube method as a measure of surface tension. The presence of foam in the soapberry solution initially introduced measurement error; however, this was minimised by determining the stirring intensity that produced the least foam and maintaining the same stirring intensity and duration throughout the experiments. In addition, assuming that the contact angle θ was always equal to 0°, giving $\cos(\theta) = 1$, was a potential source of error. This could be addressed in future measurements by using a tensiometer to directly measure the contact angle and improve the accuracy of surface tension measurements.

Further research could investigate the antibacterial and antifungal properties of soapberries using agar plates and the disk diffusion method, which would allow the soapberry extract to diffuse through the agar medium. The cleaning effectiveness of soapberries could also be assessed directly using oil or soil remediation experiments under varying concentration, temperature and pH conditions. Such investigations would provide further evidence of the practical cleaning applications of soapberries beyond surface tension measurements.

CONCLUSION

This study showed that higher concentration (5%), temperature (60°C) and pH (12) of soapberry surfactant resulted in lower surface tension, indicating greater cleaning effectiveness, and that soapberry was more effective than water, less effective than commercial detergent and similarly as effective as commercial bio-detergent. These findings support the use of soapberries in both domestic and industrial applications and demonstrate their potential as an environmentally friendly cleaning alternative.

AUTHORSHIP STATEMENT

Alexandra Prokhorov: Conceptualization, Methodology, Software, Validation, Formal analysis, Investigation, Resources, Data Curation, Writing — Original Draft, Writing — Review & Editing, Visualization, Project administration, Funding acquisition.

ACKNOWLEDGEMENTS

I would like to acknowledge PLC Sydney for providing me with the opportunity to carry out this scientific investigation, and my science mentors for constant encouragement, support, and invaluable feedback.

REFERENCES

Aminot, Y., Lanctôt, C., Bednarz, V., Robson, W. J., Taylor, A., Ferrier-Pagès, C., Metian, M., & Tolosa, I. (2020). Leaching of flame-retardants from polystyrene debris: Bioaccumulation and potential effects on coral. *Marine Pollution Bulletin*, *151*, 110862. https://doi.org/10.1016/j.marpolbul.2019.110862

Azuokwu, A. A., Yerima, Y., & Azike, R. U. (2021). Production and performance evaluation of biodetergents as an alternative to conventional drilling detergent. *SPE Nigeria Annual International Conference and Exhibition*. https://doi.org/10.2118/207167-MS

Balakrishnan, S., Varughese, S., & Deshpande, A. P. (2006). Micellar characterisation of saponin from Sapindus Mukorossi. *Tenside Surfactants Detergents*, *43*(5). https://doi.org/10.3139/113.100315

Couture, S. (2019). *Are corals and seafood affected by common chemicals?* International Atomic Energy Agency. https://www.iaea.org/newscenter/news/are-corals-and-seafood-affected-by-common-chemicals

Curtis, V. A. (2007). A natural history of hygiene. *Canadian Journal of Infectious Diseases and Medical Microbiology*, *18*(1), 11–14.

Fuchs, J. (2015). *How do you measure surface tension?* CTG Technical Blog. https://techblog.ctgclean.com/2015/12/measure-surface-tension

Ito, S., Kobayashi, T., Hatada, Y., & Horikoshi, K. (2005). Enzymes in modern detergents. In *Microbial enzymes and biotransformations* (pp. 151–161). https://doi.org/10.1385/1-59259-846-3:151

Kregiel, D., Berlowska, J., Witonska, I., Antolak, H., Proestos, C., Babic, M., Babic, L., & Zhang, B. (2017). Saponin-based, biological-active surfactants from plants. In *Application and characterization of surfactants*. InTech. https://doi.org/10.5772/68062

Liu, J., Wang, L., Sun, C., Xi, B., Li, D., Chen, Z., He, Q., Weng, X., & Jia, L. (2021). Global distribution of soapberries (*sapindus* L.) habitats under current and future climate scenarios. *Scientific Reports*, *11*, 19740. https://doi.org/10.1038/s41598-021-98389-8

Mackay, D., Celsie, A. K. D., Powell, D. E., & Parnis, M. J. (2018). Bioconcentration, bioaccumulation, biomagnification and trophic magnification: A modelling perspective. *Environmental Science: Processes & Impacts*, *20*, 72–85. https://doi.org/10.1039/C7EM00485K

Maity, J. P., Huang, Y.-M., Hsu, C.-M., Wu, C.-I., Chen, C.-C., Li, C.-Y., Jean, J.-S., Chang, Y.-F., & Chen, C.-Y. (2013). Removal of Cu, Pb and Zn by foam fractionation and a soil washing process from contaminated industrial soils using soapberry-derived saponin: A comparative effectiveness assessment. *Chemosphere*, *92*(10). https://doi.org/10.1016/j.chemosphere.2013.04.060

Only 1 Earth. (2022). *Soapberries*. Only 1 Earth. https://www.onlyoneearthaus.com.au/products/soapberries

Rai, S., Acharya-Siwakoti, E., Kafle, A., Devkota, H. P., & Bhattarai, A. (2021). Plant-derived saponins: A review of their surfactant properties and applications. *Sci*, *3*(4), 44. https://doi.org/10.3390/sci3040044

Statista. (2024). *Household cleaners: Market data & analysis*. Statista. https://www.statista.com/study/48841/household-cleaners-market-data-and-analysis/

World Health Organization. (2025). *Exposure to lead: A major public health concern. Preventing disease through healthy environments*. World Health Organization. https://www.who.int/publications/i/item/9789240112384

Yuan, C. L., Xu, Z. Z., Fan, M. X., Liu, H. Y., Xie, Y. H., & Zhu, T. (2014). Study on characteristics and harm of surfactants. *Journal of Chemical and Pharmaceutical Research*, *6*(7), 2233–2237. https://www.jocpr.com/articles/study-on-characteristics-and-harm-of-surfactants.pdf

Yueh, M.-F., & Tukey, R. H. (2016). Triclosan: A widespread environmental toxicant with many biological effects. *Annual Review of Pharmacology and Toxicology*, *56*(1), 251–272. https://doi.org/10.1146/annurev-pharmtox-010715-103417

ISSUE ACKNOWLEDGEMENTS

The Young Australians Science Journal thanks the students, educators, researchers and organisations who made this inaugural issue possible.

Student authors

We particularly acknowledge the student authors whose curiosity, persistence and willingness to share their research made this first issue possible. We thank them for engaging thoughtfully with the editorial and peer-review process and for contributing their work to the wider scientific community.

Reviewers

We thank the researchers, educators and subject-matter experts who generously contributed their time and expertise to the peer-review process. Their constructive feedback helped strengthen the articles published in this issue.

Teachers and research mentors

We acknowledge the teachers, supervisors, mentors, laboratories and research organisations that supported the student authors in developing and completing their investigations.

Partners and supporters

The Young Australians Science Journal gratefully acknowledges the University of Technology Sydney and the Science Teachers Association of New South Wales for their support in developing the journal and creating opportunities for young Australians to participate in authentic scientific research and communication.

Production

We thank the YASJ Editorial Team and those who contributed to the editing, design, typesetting, administration and technical production of this issue.

EDITORIAL BOARD

The Young Australians Science Journal Editorial Team consists of:

Dr Lisa Cabral	University of Technology Sydney
James Cleaver	IBM Australia; University of New South Wales
Dr Ann Göth	Meriden School
Dr Maria Luisa Gutierrez	Presbyterian Ladies' College Sydney
Dr Matt Johansen	University of Technology Sydney
Dr Lauren McKnight	University of New South Wales; Science Teachers Association of NSW

YASJ Young Australians Science Journal

Submit to YASJ
yasj.org.au

CALL FOR PAPERS

Peer reviewed | Student-centred | Diamond open access | No author fees

The Young Australians Science Journal (YASJ) welcomes submissions of original scientific research undertaken by Australian high school students.

Established by the founding editors and supported by the Science Teachers Association of NSW, YASJ provides a supportive pathway into scholarly publishing. Submissions undergo peer review, with constructive feedback and editorial guidance to help students develop their papers for publication.

We invite students to share their findings from any area of science with a wider audience. Whether your research paper was completed as part of a school subject, science competition or independent project, YASJ offers an opportunity to take your work beyond assessment and contribute to the scientific record. Accepted articles are published as open access, with a permanent Digital Object Identifier (DOI) and full citation details, allowing research to be discovered, cited and built upon by others.

The journal primarily aims to publish the work of senior high school students, but we also welcome submissions from younger students whose work is of an equivalent sophistication. Students and teachers are encouraged to explore the submission guidelines available on the YASJ website, and consider submitting research for an upcoming issue.

WHAT WE PUBLISH

YASJ covers all areas of science, with a focus on experimental studies, observational studies, and new analyses of existing or public data sets. Confirmation studies and negative results are welcome.

WHO CAN SUBMIT?

The first author must have been enrolled in an Australian high school when the research was carried out.
Supervisors, teachers, or mentors should be listed as authors where they meet authorship criteria.

NO NEED TO REFORMAT

Papers can be submitted for review in the format they were written in, for example for a school assessment task or competition entry.
If accepted, editors will guide authors through formatting for publication.

PUBLICATION PATHWAY

Prepare and Submit — STUDENTS AND CO-AUTHORS
→ Editorial review — YASJ TEAM
→ Peer review by experts — RESEARCHERS AND PEERS
→ Editors filter feedback — YASJ TEAM
→ Revise and format — STUDENTS AND CO-AUTHORS
→ Publish — YASJ TEAM

Visit www.yasj.org.au for more information. Contact editor@yasj.org.au with any questions

ISSN 3083-0427 (Print)

Young Australians Science Journal

Volume 1, Issue 1

27 November 2026

YASJ

https://yasj.org.au